An Accelerator Measurement of Atomic X-ray Yields in Exotic Atoms and Implications for an Antideuteron-Based Dark Matter Search

Tsuguo Aramaki

Submitted in partial fulfillment of the
requirements for the degree
of Doctor of Philosophy
in the Graduate School of Arts and Sciences

COLUMBIA UNIVERSITY

2012

ABSTRACT

An Accelerator Measurement of Atomic X-ray Yields in Exotic Atoms and Implications for an Antideuteron-Based Dark Matter Search

Tsuguo Aramaki

The General AntiParticle Spectrometer (GAPS) is a novel approach for indirect dark matter searches that exploits cosmic antideuterons. The low energy antideuteron provides a clean dark matter signature, since the antideuteron production by cosmic ray interactions is suppressed at low energy, while the WIMP-WIMP annihilation can produce low energy antideuterons. GAPS utilizes a distinctive detection method using atomic X-rays and charged particles from the exotic atom as well as the timing, stopping range and dE/dX energy deposit of the incoming particle, which provides excellent antideuteron identification.

Prior to the future balloon experiment, an accelerator test was conducted in 2004 and 2005 at KEK, Japan to measure the atomic X-rays of antiprotonic exotic atoms produced by different targets. In 2005, solid targets were tested to avoid the bulky fixture of the gas target and also to have flexibility of the detector geometry in the flight experiment. Recently, we have developed a simple cascade model and the parameters were fitted with the experimental results. The cascade model was extended to the antideuteronic exotic atom for the GAPS flight experiment.

GEANT4 simulation was conducted to obtain optimized cuts on the timing, stopping range, dE/dX energy deposit, atomic X-rays, and annihilation products, in order to eliminate the background. Based on the simulation results, we have estimated the GAPS sensitivity with the antideuteron flux. GAPS has a strong potential to detect a dark matter signature.

Table of Contents

List of Figures

List of Tables

Acknowledgments

I would first like to offer my deepest gratitude to my supervisor, Professor Charles J Hailey, who has supported me throughout my graduate career and doctoral thesis with his expertise, guidance and patience. He has set the best example as a researcher, and taught me pure research and broadened my perspectives. I greatly appreciate his encouragement and sincerity, which has helped enrich my graduate experience and research. He has been my inspiration and will always be my mentor. I would also like to thank other members of our group, Professor Rene Ong and Professor Steve Boggs, for all their knowledge and assistance. I especially want to thank Kaya Mori and Jason Koglin for their guidance and advice throughout my graduate program. They have motivated and encouraged me beyond physics, and I have been blessed to be part of a stimulating academic environment. Also, I would like to thank Kerstin Perez for the useful discussions, her philosophical advice and editing assistances. I must also acknowledge the engineers, Gordon Tajiri, Dennis Stefanik, and, Marcela Stern for all their engineering and technical assistance.

Special thanks go out to my colleagues, and fellow students, HongJun An, Melania Nynka, Stephen Chan, Philip von Doetinchem, Isaac Mognet, Paul Kaplan, and Connor Hailey, for exchanging knowledge and skills and their companionship. It has been a pleasure to work with everyone involved in this research project. Lastly, I would like to thank my family for all their support, especially to my wife, Asami, for encouraging me to pursue this degree. I also would like to thank my daughter, Ema, who was born while I was writing my dissertation, for bringing immense joy and happiness to our family.

Chapter 1

Dark Matter and Beyond Standard Model Physics

1.1 Existence of Dark Matter

The Wilkinson Microwave Anisotropy Probe (WMAP) results confirmed that 73% of our universe is composed of dark energy, and 22% is dark matter ($\sim 5\%$ for baryonic matter, see Figure 1.1 [Jarosik *et al.*, 2011]). The nature and origin of these phenomena, however, are

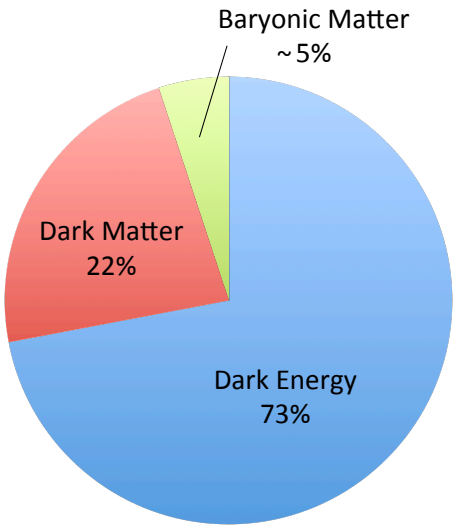

Figure 1.1: Composition of our universe [Jarosik *et al.*, 2011]

still unknown, and thus are the great cosmological problems of the 21st century. Unlike dark energy, dark matter is well-motivated by many theoretical models, and several experiments are currently being conducted to determine the origin of this matter (see Chapter 2).

1.1.1 Rotational curves

The existence of dark matter was postulated by Fritz Zwicky in 1933. He found that the rotational speed of galaxies was too large to be supported by the luminous matter. The rotational velocity can be estimated from Newton's law of gravitation as below.

$$\frac{mv^2}{r} = G\frac{M(r)m}{r^2}$$

Here, m and v are the mass and the rotational speed of the object (e.g. star) in the galaxy, r is its distance from the center of the galaxy, and $M(r)$ is the mass enclosed inside the galaxy's orbit at the distance r. Since most of the luminous mass of typical spiral galaxies exists in the central region, the rotational speed would be expected to decrease as $r^{1/2}$. In the 1970s, the rotational curves, the rotational speeds of objects in the galaxy with respect to their distance from the center of the galaxy, was measured by Vera Rubin et al.[Rubin and Ford, 1970], and they were not proportional to $r^{1/2}$, but almost flat. This implied the existence of non-luminous "missing mass" in the galaxy, which is now referred to as dark matter.

1.1.2 Weak gravitational lensing

Additional evidence of the existence of dark matter comes from gravitational lensing measurements. The light from a very distant, bright source is deflected by the curvature of space-time near the object. From the distortion of the light, the mass of the object can be estimated. The recent observation of the Bullet Cluster, two colliding clusters of galaxies, shows that the mass distribution obtained from the gravitational lensing analysis is different from the distribution of the baryonic matter observed by X-ray telescope [Clowe *et al.*, 2004]. The mass distribution obtained from the gravitational lensing is similar to the one observed before the collision, while the baryonic matter concentrates near the impact point. This implies that there is some mass around the object that does not interact

by electromagnetic forces. Note that the Bullet Cluster may not be explained by MOND (modified newtonian dynamics), which is one of the popular theories that can explain the galaxy rotation problem without introducing dark matter.

1.2 Dark Matter Candidates

A candidate source of dark matter should satisfy the following conditions, as described in this section. Since dark matter has never been directly observed, interactions with the Standard Model particles by the strong nuclear force and the electromagnetic force should be prohibited. On the other hand, since it can generate gravitational force, as seen in the rotational curves and gravitational lensing, it should have non-zero mass. Moreover, it should be stable on a cosmological time scale.

The dark matter candidates are categorized into baryonic and non-baryonic dark matter. The baryonic dark matter candidates are often called massive compact halo objects (MACHOs), which emit little or no radiation, such as black holes, neutron stars, and brown dwarfs. However, since Big Bang Nucleosynthesis constrains the amount of baryonic matter in the universe, the baryonic dark matter model has been excluded as a viable dark matter candidate.

Non-baryonic dark matter can be further categorized into hot dark matter and cold dark matter. Hot dark matter is considered to be light relativistic particles such as neutrinos. However, due to their large free streaming, the small density fluctuations seen in the cosmic microwave background (CMB), the relic radiation from the Big Bang, would be smoothed out and not able to clump together to create the galaxies and galaxy clusters we see now. Therefore, hot dark matter has also been excluded from the list of possible dark matter candidates [Peacock, 1999; L. Bergstrom, 2006]. Note that although baryonic dark matter and hot dark matter have been excluded as the sole sources of dark matter, they could still constitute some small fraction of this missing mass.

Cold dark matter, on the other hand, has a small free streaming length, since it is non-relativistic, which allows the small density fluctuations in the early universe to form the large scale structure of the modern universe. Therefore, cold dark matter is the preferred

model for dark matter. WIMPs (weakly interacting massive particles) and axions are the theoretically best motivated candidates for cold dark matter. I will introduce these particles in the following sections based on the references [Peacock, 1999; Feng, 2010; Porter *et al.*, 2011; Servant and Tait, 2003; Cheng *et al.*, 2002; Asztalos *et al.*, 2006].

1.2.1 WIMPs

WIMPs are typically considered to be thermal relics of the early universe. The Boltzmann equation and the thermal equilibrium density of the dark matter can be expressed as below.

$$\begin{aligned} \frac{dn_\chi}{dt} &= -3Hn_\chi - \langle\sigma v\rangle\,(n_\chi^2 - (n_\chi^{eq})^2) \\ n_\chi^{eq} &\sim g\left(\frac{mT}{2\pi}\right)^{3/2} e^{-T/m} \end{aligned}$$

Here, H is the Hubble parameter, n_χ is the number density of dark matter, t is time, σ is the thermally averaged annihilation cross section, v is the relative velocity ($\sim 10^{-3}$c), n_χ^{eq} is the thermal equilibrium density, g is the degrees of freedom of the dark matter particle, T is the temperature, and m is the mass of the dark matter. By solving the above equations, we obtain the fractional abundance as follows.

$$\Omega_\chi \sim \frac{0.1}{h^2}\left(\frac{3\times 10^{-26} cm^3 s^{-1}}{\langle\sigma v\rangle}\right)$$

With current dark matter density, $\Omega_\chi \sim 0.23$, and Hubble constant, $h \sim 0.7$, the interaction cross section, σ, will be of the order of the weak interaction scale. This is consistent with observations indicating that dark matter does not interact with the Standard Model particles by the strong force or electromagnetic force, i.e. only the weak force and gravitational force are allowed. This coincidence is called the "WIMP miracle".

Since none of the Standard Model particles are qualified to be dark matter, a new physics model has to be invoked for the dark matter particle. The two most popular dark matter candidates from beyond Standard Model physics, neutralinos in the supersymmetry (SUSY) theory and Kaluza-Klein particles in the extra dimension theory, will be discussed below.

1.2.1.1 SUSY Theory and Neutralino

The SUSY theory postulates that all the particles in the Standard Model have partners (superpartners) that have the same quantum numbers and gauge interactions as the Standard Model partners, but differ in spin by 1/2. Therefore, the superpartners of the fermions in the Standard Model are bosons, and the superpartners of bosons in the Standard Model are fermions. The SUSY theory is motivated by the need to solve the hierarchy problem of the Higgs scalar mass, since the divergent radiative corrections to the Higgs scalar mass from the Standard Model particles will be cancelled out by the contribution from the corresponding superpartners. Furthermore, in a SUSY theory in which new interactions begin in the TeV region, gauge couplings of the three gauge groups unify at $m_{GUT} \sim 10^{16}$ GeV, yielding a grand unified theory of electromagnetic, weak, strong forces. Since SUSY theory requires a huge number of degrees of freedom, the Minimal Supersymmetric extension of Standard Model (MSSM) is often used to simplify the model. The conservation of R-parity is often introduced in SUSY models, where R is defined as:

$$R \equiv (-1)^{3B+L+2s}$$

Here, B is the baryon number, L is the lepton number, and S is the particle spin. This indicates that R for the Standard Model particles is always 1, while R for the parameter-constrained SUSY particles is -1, and the SUSY particles can only decay into odd numbers of SUSY particles (plus any number of Standard Model particles). Therefore, the lightest supersymmetric partner (LSP) in the SUSY model becomes a stable particle. It can only be destroyed via self annihilation, which allows the LSP to be a candidate for dark matter. Among the SUSY particles, the neutral particles (charge = 0) are the gravitino, neutralino (a mass eigenstates of the bino, wino and two higgsinos), sgluon, and three generations of sneutrinos, but since the interaction cross section of the dark matter is of the order of the weak scale, only neutralino and sgluon can be candidates for dark matter.

1.2.1.2 Universal Extra Dimension Theory and Kaluza-Klein particle

Kaluza-Klein theory is a model that originally attempted to unify electromagnetism with gravity in higher dimensions. Kaluza and Klein published their original theory in 1921,

and more recently it was realized that this theory can explain the hierarchy problem by introducing the Plank constant in extra dimensions.

In Kaluza-Klein theory, the normal 3+1 dimensions are called a "brane" in the 3+1+k dimensional "bulk" space-time. The extra dimensions are assumed to be "compactified", as proposed by Oskar Klein in 1926, and they are considered to be on a circle with $R \sim 10^{-18}$ m. Since gravitons are allowed to propagate in the bulk, the momentum in the compactified dimensions should be quantized as $p \sim n/R$, where n is called Kaluza-Klein states, and the corresponding mass eigenstates are $m \sim n/R$. Since the extra dimensions are compactified, this model can be considered as the universal extra dimensions (UED) model, where all of the Standard Model fields may propagate in one or more compact extra dimensions. In other models, only gravitons can propagate in the bulk, while the Standard Model fields are confined in the brane. Since the Kaluza-Klein parity, $(-1)^n$, is considered to be conserved [Cheng *et al.*, 2002], the lightest Kaluza-Klein particle (LKP) is stable and can be a candidate for dark matter. The Kaluza-Klein photon, $B^{(1)}$, is considered to be the lightest Kaluza-Klein particle, since it receives negative radiative corrections. Dark matter experiments will be able to explore the relevant parameter space of the LKP. A Kaluza-Klein right-handed neutrino (LZP) can also be a candidate of dark matter under Z_3 symmetry, a baryon number and color charge symmetry in the Randall-Sundrum Model [Randall and Sundrum, 1999; Barrau *et al.*, 2005; Hooper and Servant, 2005].

1.2.2 Other Candidates: Axion

There are many other dark matter candidates, such as CHAMPS, Cryptons, D-matter, Q-balls, SWIMPS, Wimpzillas etc., but the axion is one of the most popular dark matter candidates. The axion is a hypothetical particle that was introduced by Peccei-Quinn to resolve the strong CP problem in quantum chromodynamics. The Lagrangian in QCD (quantum chromodynamics) can have a CP-violating term:

$$L = \cdots + \frac{\theta g^2}{32\pi^2} G_{\mu\nu} \tilde{G^{\mu\nu}} \cdots .$$

Here, $G_{\mu\nu}$ is the gluon field strength tensor, g is the QCD coupling constant and θ is an experimentally derived parameter. However, the CP violating term has never been

observed in measurements of the neutron electric dipole moment, and thus θ is constrained to be $\theta \leq 10^{-10}$ [Peccei and Quinn, 1977b]. Peccei and Quinn introduced the spontaneously broken global Peccei-Quinn symmetry, $\mathrm{U}(1)_{PQ}$, to resolve this "strong CP problem". They modified the Lagrangian as follows [Peccei and Quinn, 1977a]:

$$L = \cdots + \left(\theta - \frac{a}{f_a}\right) \frac{g^2}{32\pi^2} G_{\mu\nu} \tilde{G^{\mu\nu}} \cdots ,$$

where a is the axion field, and f_a is the axion decay constant. The axion field takes a minimum value at $a = \theta f_a$, where the axion appears as a pseudo Nambu-Goldstone boson with the mass:

$$m_a \sim 6\ \mu\mathrm{eV} \left(\frac{10^{12}\mathrm{GeV}}{f_a}\right).$$

Since axions can be produced with several different mechanisms, they are strong candidates for dark matter. The equation below gives the Lagrangian for the coupling of the axion to two photons. From this can be derived the second equation below, the lifetime of the thermal axion. In the equation below, if the age of the universe is used as a lower limit for the axion decay time and g_γ is a model dependent parameter, then the mass of the axion is constrained to be $m < 20$ eV. Such a low value of thermal axion mass is excluded because it would not be consistent with arguments related to galaxy structure formation, as mentioned above. Therefore, thermal axions cannot be the sole source of dark matter.

$$\begin{aligned} L_{a\gamma\gamma} &= -g_\gamma \frac{\alpha}{\pi} \frac{a}{f_a} \vec{E} \cdot \vec{B} \\ \tau_{a\to\gamma\gamma} &= \frac{64\pi}{g_{a\gamma\gamma}} \sim \frac{8.8 \times 10^{23}\ \mathrm{s}}{g_\gamma^2} \left(\frac{\mathrm{eV}}{m_a}\right)^5 \end{aligned}$$

α : the fine-structure constant

g_γ : a model dependent parameter

$\tau_{a\to\gamma\gamma}$: decay constant

There are several non-thermal production mechanisms for axions, and the relic density is estimated as [Feng, 2010]:

$$\Omega_a \sim 0.4\theta_i^2 \left(\frac{f_a}{10^{12}\text{GeV}}\right)^{1.18}.$$

Here, θ_i is the initial vacuum misalignment angle. Therefore, if $f_a \sim 10^{12}$ GeV and $\theta_i \sim 1$, the axion can be dark matter. Axions may be observed experimentally, since axions can convert into photons under a strong magnetic field [Asztalos *et al.*, 2006].

Chapter 2

Dark Matter Searches

There are dozens of experiments designed to search for particles associated with various manifestations of WIMP dark matter. Based on the detection approach, experiments can be categorized into three types: particle collider, direct search, and indirect search. The direct and indirect searches will measure the relic WIMPs, while the particle collider will try to create WIMPs. The detection methods and the background models for each search are not completely different, but also complementary, helping to illuminate the nature of dark matter.

2.1 Particle Collider

Particle accelerator experiments have been conducted since the 1930s. The LHC (Large Hadron Collider) is the largest and highest energy particle accelerator (p-p collisions), designed to search for new particles, including the Higgs boson (probably discovered) and SUSY particles. Each proton can be accelerated up to 7 TeV and collided with another in the main ring.

Seven experiments are currently conducted at the LHC, with the ATLAS and CMS experiments leading the measurement of SUSY particles. Both experiments have a similar detector composition, consisting of four major components. In the core of the detector, the tracker, surrounded by a magnet, measures the momentum. Each is covered by two calorimeters, an electromagnetic calorimeter and a hadronic calorimeter. The elec-

tromagnetic calorimeter measures the energy of electrons and photons, while the hadronic calorimeter measures the energy of hadrons. The calorimeters are surrounded by a muon spectrometer that measures the momentum of outgoing muons.

Unfortunately, WIMPs seldom interact with matter inside the detector, and they cannot be directly detected. Therefore, the missing energy and momentum need to be estimated using energy and momentum conservation. The proton-proton collision produces a pair of squarks and gluinos that decay into other SUSY particles, ultimately decaying into the stable LSP. The missing energy and momentum are estimated by vectorially summing the total energy and momentum in the detector [Polesello and Tovey, 2004].

2.2 Direct search

Experiments for direct dark matter searches have been conducted since the 1980s [Gaitskell, 2004]. Direct searches measure the recoiled energy of a target atom in the detector induced by the interaction with the WIMP. The recoil energy can be estimated as below.

$$E_R = \frac{\mu^2 v_\chi^2}{m_N}(1 - \cos\theta)$$

Here, E_R is the recoil energy, v_χ is the velocity of WIMPs, m_N is the mass for the target, θ is the scattering angle in the center of mass frame, and μ is defined below.

$$\mu \equiv \frac{m_\chi m_N}{m_\chi + m_N}$$

Since $m_\chi \sim 100$ GeV and $v_\chi \sim 0.001c$, E_r will be a few tens of keV. The recoil energy will be measured through heat, ionization and scintillation in the detector. Since the WIMP event is very rare and there are many types of backgrounds in that energy range, such as neutrons, gamma rays, and cosmic rays, the detector is often installed underground with passive and active shieldings.

The Xenon100 experiment uses a dual phase (gas and liquid) Xenon target surrounded by PMTs. The signals in the liquid (S1) and gas (S2) target and the drift timing inside the liquid target provide fiducial volume cuts to suppress the background. Additionally, the signal in the liquid target allows one to distinguish WIMP events from gamma-ray events, since gamma rays interact with electrons rather than the nuclei. The log10(S2/S1)

for electron recoil (gamma rays) is around 2.5, while 1.8 for nuclear recoil. The Xenon100 experiment has the current best upper limit of the WIMP-nucleon interaction cross section as seen in Figure 2.1 [Aprile *et al.*, 2011; Aprile *et al.*, 2012].

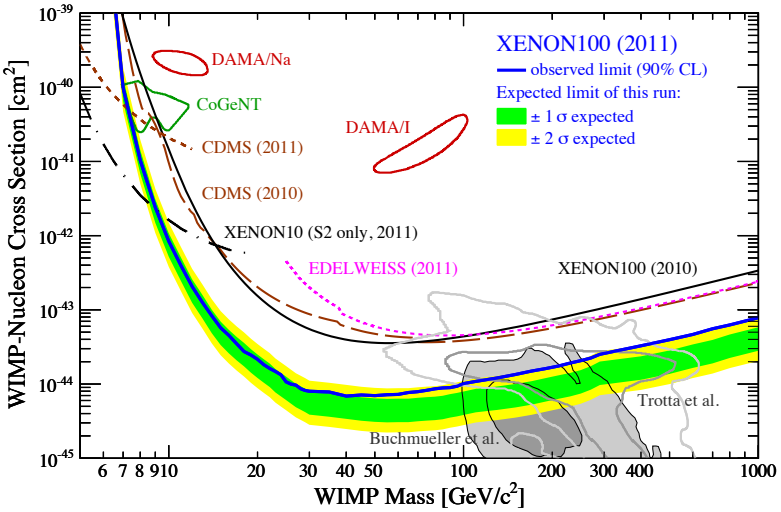

Figure 2.1: Spin-independent elastic WIMP-nucleon cross section as a function of WIMP mass m_χ, compared with other experiments. The solid blue line is the new XENON100 limit at 90% C.L. [Aprile *et al.*, 2011].

The cryogenic dark matter search (CDMS) measures the ionization and phonons from nuclear recoils in Ge and Si detectors at milli-Kelvin temperatures. It distinguishes nuclear recoil events from electron recoil events by the ratio of the ionization signal to the phonon signal. They also set the upper limit of the WIMP-nucleon interaction cross section (see Figure 2.1).

The DAMA project, which measures scintillation light with NaI detectors, announced a dark matter detection with their 7-year measurements, claiming to observe a model-independent annual modulation effect by the dark matter halo [Belli *et al.*, 2002]. This result indicates that the dark matter has relatively low mass, $\sim$ 10 GeV or $\sim$ 50 GeV (see figure 2.1). The CoGeNT experiment, which measures the ionization charge from nuclear recoils in the Ge detector, also claimed that they found events that could be a signature of dark matter with the mass $\sim$ 10 GeV [Aalseth *et al.*, 2011]. Note that low mass dark matter

may enhance the flux of the particles produced by the WIMP-WIMP annihilation, since the annihilation rate increases (see Section 2.3). However, DAMA and CoGeNT results conflict with other experiments, as seen in Figure 2.1.

2.3 Indirect search

The WIMP-WIMP annihilation rate is highly suppressed after the "freeze out" in the early universe. However, they can still annihilate with each other. The annihilation products can be W and Z bosons, gluons, quarks, leptons, and photons. Here, W and Z bosons, gluons, and quarks can generate jets and produce hadrons (including antiprotons and antideuterons), leptons and gamma rays. Since these particles are detectable Standard Model particles, the dark matter can be indirectly measured through these particles. Note that since these particles can also be produced by astrophysical sources and cosmic ray interactions, detailed background studies are essential to distinguish the dark matter signature from other astrophysical backgrounds.

IceCube searches for WIMP-induced neutrinos from the Sun. The WIMPs are gravitationally trapped in the Sun when the Sun sweeps through the dark matter halo. This increases the WIMP-WIMP annihilation rate, and neutrinos will be emitted from the Sun. The IceCube detector is capable of observing neutrinos with energies above 100 GeV [Hultqvist, 2011].

PAMELA (a payload for antimatter matter exploration and light-nuclei astrophysics), PPB-BETS (polar patrol balloon, balloon-borne electron telescope with scintillating fibers), ATIC (advanced thin ionization calorimeter), and Fermi LAT (large area telescope) have recently claimed to observe an excess of positron flux around 10 GeV - 200 GeV [Chang *et al.*, 2008; Abdo *et al.*, 2009; Adriani *et al.*, 2009]. However, it is still ambiguous whether the data show a dark matter signature, since there are many astrophysical sources, such as pulsars, that can explain the excess in the energy range.

Furthermore, a dark matter signature around 130 GeV in gamma-ray Fermi-LAT data from Galactic center observations [Weniger, 2012] has been announced. However, this claim is controversial due to the expected large astrophysical background from the Galactic center.

The line may be a real dark matter signature, but needs to be proven and further supported by other experiments as well. In the next section, I will introduce an indirect dark matter search using antibaryons, especially low energy antideuterons, which can provide a clear signature of the dark matter annihilation.

2.3.1 Antibaryon Search

2.3.1.1 Antiproton Search

Cosmic ray antiprotons have been detected for over 20 years including the recent measurement by PAMELA, BESS (balloon-borne experiment), and AMS (Alpha Magnetic Spectrometer) [Bonechi *et al.*, 2010]. Antiproton can be also produced by the WIMP-WIMP annihilation, however, the flux is similar or less than the one produced by the cosmic ray interaction in the interstellar medium. This provides the upper limit of the antiproton production by the WIMP-WIMP annihilation and constrained some of the WIMP parameter.

2.3.1.2 Antideuteron Search

Antideuteron production in WIMP-WIMP annihilations was proposed by Donato et al., in 2000 [Donato *et al.*, 2000; Donato *et al.*, 2008]. The antideuteron flux due to WIMP-WIMP annihilation (primary flux) can be estimated based on the dark matter density profile of galaxy, the WIMP-WIMP annihilation channel, the hadronization and coalescence model, and the propagation model. Here, the density profile determines the annihilation rate. The preferred annihilation channels are $\chi\chi \rightarrow W^+W^-$, $\chi\chi \rightarrow ZZ$, $\chi\chi \rightarrow b\bar{b}$, where χ is WIMP dark matter, since they can produce jets, and quarks and gluons in the jet can form hadrons by the strong force. If an antiproton and an antineutron produced in the hadronization process travel together within a certain relative momentum range, called coalescence momentum, they will form an antideuteron. The produced antideuterons will be propagated and reach the top of atmosphere (TOA). The primary antideuteron flux due to the WIMP-WIMP annihilation (solid purple line: LSP with $m_\chi \sim 100$ GeV, dashed green line: LKP with $m_\chi \sim 500$ GeV, dashed blue line: LZP with $m_\chi \sim 40$ GeV) is shown in Figure 2.2 [Baer and Profumo, 2005]. The relatively flat peak is located at E $\sim$ 0.2 GeV/n. The antideuteron flux due to the cosmic ray interactions with the interstellar medium

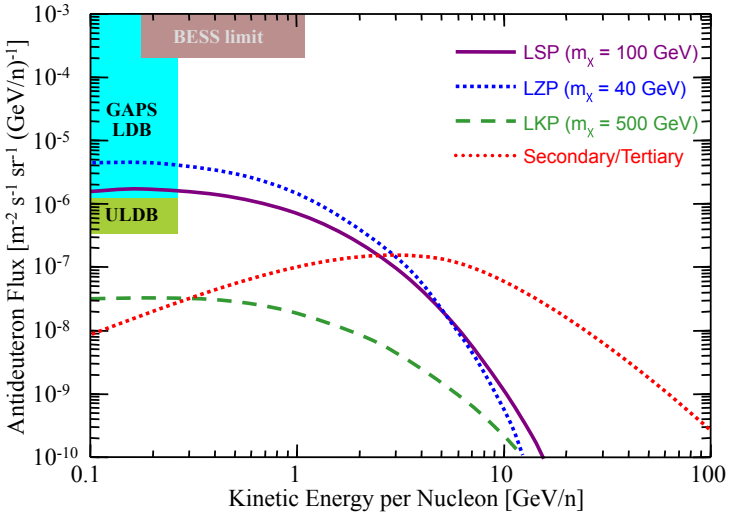

Figure 2.2: Antideuteron flux at the top of the atmosphere, compared with the BESS upper limit[Fuke *et al.*, 2005], and GAPS sensitivity The purple solid line (LSP), green dashed line (LKP), and green dashed line (LKP) representrepresent the primary antideuteron fluxes due to the dark matter annihilations [Baer and Profumo, 2005]. The red solid line represents the secondary/tertiary flux due to the cosmic ray interactions [Duperray *et al.*, 2005; Salati *et al.*, 2010].

(secondary/tertiary flux, red dashed line) is also shown in Figure 2.2 [Duperray *et al.*, 2005; Salati *et al.*, 2010]. Here, antiprotons (antineutrons) can be produced only as a pair, $p\bar{p}$ or $n\bar{n}$, due to baryon number conservation.

$$p + N \rightarrow p + N + (p + \bar{p}) + (n + \bar{n}) \cdots$$

Here, N is a nucleus in the interstellar medium. This requires the original cosmic ray proton to be energetic in order to produce an antiproton and an antineutron, and as a consequence the center of mass frame will be boosted. Therefore, the peak of the secondary flux is shifted to higher energy compared with the primary flux. In addition, since the flux of the cosmic ray proton follows the power law, $F_p \sim E^{-2.7}$, the interaction rate is drastically decreased and thus the antideuteron flux is also decreased.

The GAPS sensitivity (see Chapter 7) and the current upper limit for the antideuteron flux obtained by BESS experiment [Fuke *et al.*, 2005] are also shown in Figure 2.2. The

primary antiproton flux is two orders of magnitude larger than the secondary antideuteron flux, and we can clearly distinguish them. The GAPS balloon project (see Chapter 3) thus has a strong opportunity to detect the antideuterons as the dark matter signature.

Chapter 3

GAPS Balloon Project

3.1 Overview

The general antiparticle spectrometer (GAPS) was first proposed by Hailey and Mori in 2002 [Mori *et al.*, 2002], and was originally named the Gaseous AntiParticle Spectrometer. The original GAPS was designed to use a gaseous target, but with further studies, including the KEK (high energy accelerator research organization) beam test described in this thesis, we concluded that a solid target was more efficient and effective for the flight experiment. Since GAPS is a balloon-borne experiment (flight altitude $\sim$ 35 km), there are constraints on the size and mass of the payload. The solid target can greatly simplify the setup of the GAPS flight module by removing the bulky gas handling system and allowing more complex designs, such as a multi-layer detector geometry. The higher density of the solid target can easily slow down and stop more incoming antiparticles, which provides a larger detectable energy range. A GAPS prototype flight (pGAPS) was launched successfully from the JAXA/ISAS balloon facility in Hokkaido, Japan in summer 2012 [Doetinchem, 2012], and a proposed GAPS science flight is to fly from Antarctica in the winter of 2016-2017.

3.2 Detection Concept

The GAPS detection method involves capturing antiparticles into a target material with the subsequent formation of an excited exotic atom. A time-of-flight (TOF) system measures

the velocity (energy) and direction of an incoming antiparticle. It slows down by the dE/dX energy loss and stops in the target material, forming an excited exotic atom. The exotic atom de-excites in a complex process involving Auger ionization and electron refilling at high quantum number states, followed by the emission of X-rays at the lower quantum states (see Chapter 4). With known atomic number of the target, the Bohr formula for the X-ray energy uniquely determines the mass of the captured antiparticle [Mori *et al.*, 2002]. Ultimately, the antiparticle is captured by the nucleus in the atom, where it is annihilated with the emission of pions and protons. The number of pions and protons produced by the nuclear annihilation is approximately proportional to number of antinucleons, which provides an additional discriminant to identify the incoming antiparticle. The entire process takes place in less than a nanosecond. This process is illustrated in Figure 3.1. The Lithium-drifted silicon (Si(Li)) detector will be used both as a target to form the exotic atom and as a detector to detect atomic X-rays and the annihilation products. The concept of the detection technique has been verified through the accelerator testing at KEK in 2004 and

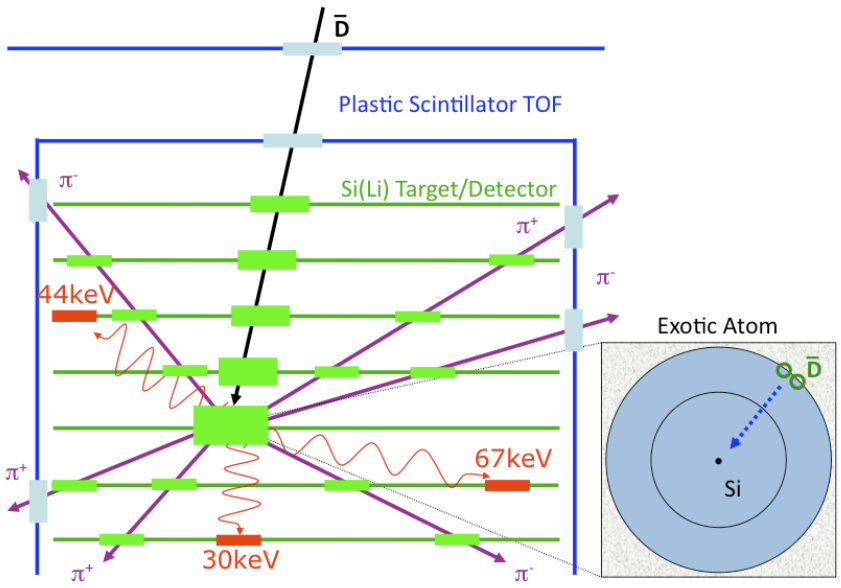

Figure 3.1: Schematic for GAPS detection method. An antiparticle slows down and stops in the Si(Li) target forming an exotic atom. The atomic X-rays will be emitted as it de-excites followed by the pion (and proton) emission in the nuclear annihilation.

2005, as described in Chapter 5 and 6.

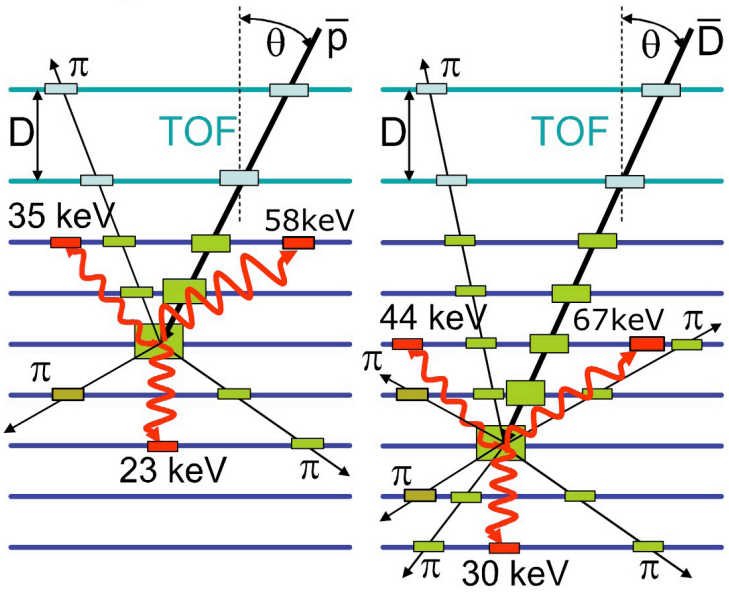

Figure 3.2: Antideuteron-antiproton identification technique: (1) depth sensing, (2) unique atomic X-rays, (3) pion multiplicity.

Antiprotons are a major background in this experiment, since they can also form exotic atoms and produce atomic X-rays and charged particles. However, the atomic X-rays and the number of pions and protons emitted from the exotic atom uniquely identify the mass of the original antiparticle, as do the depth sensing (stopping range of the incoming particle) and the dE/dX energy loss in each Si(Li) detector, once the velocity of the incoming antiparticle is determined by the TOF system. The three highest antideuteronic X-rays with a Si target are 67 keV, 44 keV and 30 keV, while antiprotonic X-rays are 107 keV, 58 keV, and 35 keV. The number of charged particles produced by the nuclear annihilation for the antideuteronic exotic atom is approximately twice as many as the one for the antiprotonic exotic atom. Additionally, antideuterons with the same TOF have a longer stopping range and can go deeper into the detector system than antiprotons. Thus, antideuterons with the same TOF will have a larger velocity and deposit less energy at each layer than antiprotons, since the dE/dX energy loss is inversely proportional to the velocity squared at low energy (see Figure 3.2). As a result, these detection methods provide a $> 10^6$ antiproton rejection

factor (see Chapter 7).

3.3 Instrumental Design

The GAPS balloon flight will have several unique features. It will be the first balloon flight with a very large, pixellated Si(Li) detector surrounded by a very large TOF system without a pressure vessel (see Figure 3.3). There will be 13 layers of detectors surrounded by TOF plastic scintillators, with each layer composed of 4 inch diameter, 2.5 mm thick Si(Li) detectors. Each Si(Li) detector will be segmented into 8 strips, and adjacent tracking layers will have their strips positioned orthogonally, providing modest three-dimensional tracking.

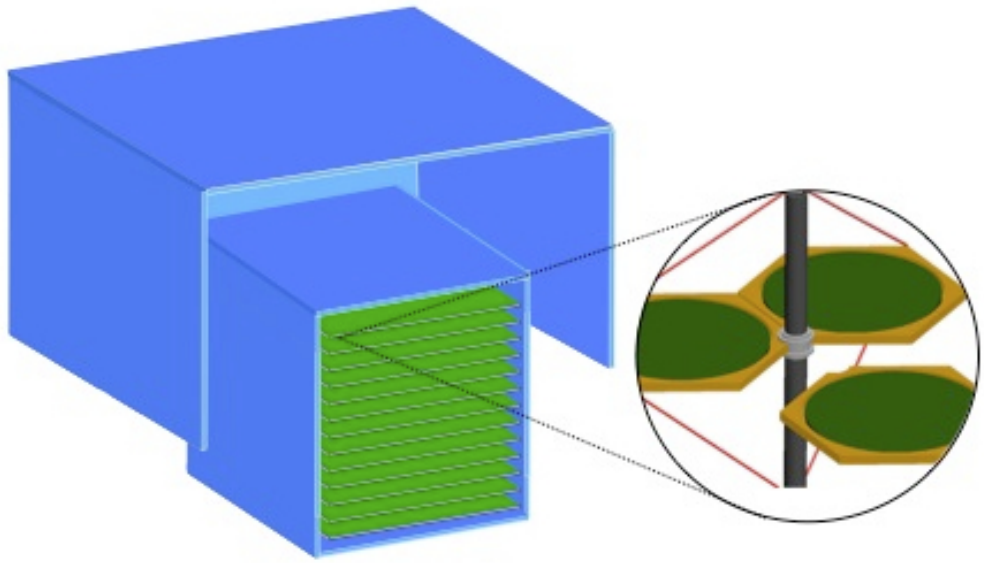

Figure 3.3: GAPS detector design. 13 layers of Si(Li) detectors are surrounded by the TOF plastic scintillators. Each Si(Li) detector is 4 inch diameter, 2.5 mm thick.

A tracking geometry is a natural consequence of the current GAPS detection concept, unlike the original GAPS (*gaseous* antiparticle spectrometer) cubic geometry, which only focused on detecting atomic X-rays using a the gaseous cell target surrounded by scintillation detectors without determining trajectory information [Mori *et al.*, 2002; Hailey, 2004; Hailey

et al., 2006]. The tracking geometry can count the number of particles produced in the nuclear annihilation and separately identify atomic X-rays from particle tracks. It also permits direct measurement of particle stopping depth and naturally conforms to the multi-detector geometry. Note that since each strip is relatively small, $\sim$ 1 cm wide, X-rays and charged particles (pions/protons) can be detected separately in the different strips/channels. Each Si(Li) layer also works as a degrader and a target material to slow down the incoming antiparticle and to form an exotic atom.

3.3.1 Si(Li) Detector

The key to the GAPS detection method is the good energy resolution and the good timing resolution in Si(Li) detectors, which allow one to identify the antideuterons with their atomic X-rays. Lithium compensation of silicon permits one to achieve an excellent energy resolution with a thicker detector width ($\sim$ 2-3 mm) than can be obtained with pure, high resistivity silicon. In particular, an energy resolution of $\sim$ 3 keV (FWHM), extremely modest for a modern Si(Li) detector, is adequate to clearly identify the antideuteronic and antiprotonic X-rays. The timing resolution of Si(Li) detectors, $\leq$ 100 ns using simple zero crossing timing on the preamplifier output, is also adequate to suppress sources of background such as cosmic rays and the diffuse X-rays that are temporally incoherent with the X-ray emission and nuclear annihilation.

The concept of the Si(Li) detector was first conceived by Pell in 1960 [Pell, 1960]. Since the Lithium ion acts as a donor, creating an excess of negative charge carriers (positive) in the silicon crystal, the p-type silicon that has the excess of positive charge carriers can be compensated by drifting the Lithium ion inside, which permits a thicker ($>$ 2 mm) intrinsic region, unlike a high-resistivity Silicon detector. The intrinsic region is the volume where there are no free carriers present and the electric field is constant. Therefore, when X-rays come into the intrinsic region and interact with Silicon crystals, electron-hole pairs will be created. Here, the number of created electron-hole pairs is proportional to the deposited energy. These electrons and holes will be separated by the applied bias between the electrodes and collected into the charge sensitive preamplifier.

The Si(Li) detector is the ideal detector for the GAPS detection method since it can

be used not only as the X-ray detector with an excellent energy resolution, but also as the tracker for the incoming antiparticle and the outgoing charged particles produced by the nuclear annihilation. Moreover, it also serves as the target material to stop the antideuteron and to form the exotic atom. A 2-3 mm thick Si(Li) detector is a good compromise, since the X-rays need to escape from one detector with high probability and yet to be absorbed in another with high efficiency. The Si(Li) detector has high enough energy resolution to resolve the antideuteronic X-rays from the antiprotonic X-rays.

3.3.2 Data Acquisition (DAQ) system and Cooling System

Since the GAPS Si(Li) detector was designed to simultaneously detect atomic X-rays and track charged particles, the readout system has two modes, high gain mode and low gain mode. The range for the high gain mode is $\sim$ 20 - 80 keV with $\sim$ 3 keV FWHM energy resolution, while the range of the low gain mode is $\sim$ 1 - 50 MeV with 10% FWHM energy resolution. This dual-mode system was tested in pGAPS. Since there will be $\sim$ 24000 channels in bGAPS and the power for the readout is limited in the flight configuration, an application-specific integrated circuit (ASIC) is required. The ASIC allows us to achieve the required spectral resolution and to have the dynamic energy range in the DAQ system while maintaining low mass. Any passive mass near the Si(Li) leads to efficiency and tracking losses. Our partner, Oak Ridge National Laboratory (ORNE), has already designed and tested an ASIC for other Silicon sensors and their requirements are very similar to ours: the X-ray mode requires low noise ($<$ 3 keV) over a wide dynamic range ($\sim$ 10-100 keV) to measure atomic X-rays and provide overlap with the particle mode, which will have moderate noise ($\sim$ 10% FWHM) over a higher energy range (1-50 MeV). The readout will provide system-wide coincidences of $\sim$ 1 μs between tracker and TOF.

The performance of the Si(Li) detector is strongly affected by the temperature and requires a temperature of at least -30C to achieve $<$ 3 keV FWHM energy resolution. The thermal cooling concept was built based on this requirement. The GAPS mechanical and cooling design is based on a modular approach, with three detectors mounted on a hexagonal carrier mechanically fixed to a central Al coupling (coolant port). The carriers are made of 0.030 inch thick Al sheet metal with stiffening flanges on six sides. The coupling acts

as both the structural support for the module and a heat exchanger. The fluid (EM Novec heat transfer fluid) circulates inside the PTFE tube with a pump, and heat will be released from the radiator to outer space. The coolant temperature is predicted to be -50C at the radiator and -40C at the Si(Li) wafers during the flight.

The oscillating heat pipe (OHP) is a possible new technique for the cooling system that uses the basic concept of the heat transfer in the phase transition. A liquid inside the pipe at the hot interface turns into a vapor by absorbing the heat and then moves to the colder side and condenses back into a liquid with release of the latent heat. This process can be repeated as long as there is temperature difference in the system. Since the OHP does not require any mechanical pump, it can vastly reduce power consumption in the flight system. A prototype of the OHP system was demonstrated in the pGAPS flight.

3.3.3 TOF System

The TOF system provides the timing and spatial information on the incoming particle, which allows us to distinguish antideuterons from other particles through the stopping range. The antideuteron flux at the top of atmosphere (TOA) can be also estimated with the TOF timing by tracking it backwards. The inner TOF plastic scintillators will completely surround the Si(Li) detector planes, and the outer TOF scintillators will cover the top and halfway down the sides of the inner TOF, separated by 1 m. The scintillator will be 0.3 cm thick and segmented into paddles that are 15 cm wide and 100 cm long. Curved acrylic light guides will be mounted on both ends of each paddle, and the scintillation photon will be read out by a high-speed photomultiplier tube (PMT).

In order to reduce the total weight of the TOF system, the GAPS scintillators will be relatively thin, 0.3 cm, but they will provide good timing resolution, 500 ps. The performance could be enhanced since high quantum efficiency (ultra-bialkali) PMTs will be available for the GAPS flight. Also, since GAPS focuses on the slow antiparticles, $0.2 \geq \beta \geq 0.5$, the light emitted in the scintillator will be ~ 4 times more than for minimum ionizing particles (MIPs). The timing difference of two PMT signals at the opposite ends of the scintillator will provide ~ 6 cm spatial resolution, and ~ 5 degree of angular resolution will be provided for the incoming particle with this TOF system.

3.4 Detector Development

3.4.1 Overview of Detector Program

The Si(Li) detector has been extensively developed for X-ray astronomy and flown on a satellite [Serlemitsos, 1984]. It was originally developed in the 1960s as a particle tracker for high-energy particle physics, although it was ultimately replaced by high-resistivity Silicon detectors. However, GAPS will be the first balloon flight to employ a very large area, segmented, high energy resolution Si(Li) detector. In order to progress rapidly towards a science experiment, the GAPS project is taking a dual approach to the development and demonstration of the Si(Li) detector technology. The near term goal was a technology demonstration of a prototype GAPS (pGAPS) instrument. pGAPS was successfully launched from the JAXA/ISAS balloon facility in Hokkaido, Japan in summer 2012, and we are currently analyzing the data. The pGAPS goals were (1) to demonstrate stable, low noise Si(Li) performance with good energy resolution at the ambient pressure (1-10 torr) of balloon altitude, $\sim$ 35 km, (2) to demonstrate the in flight cooling of the Si(Li) detector using our baseline approach, and (3) to characterize the background in the Si(Li) detectors at balloon altitude. The longer term goal is to demonstrate the capability to mass produce Si(Li) detectors for the ultimate science experiment, which is called bGAPS. The goal is to fly bGAPS from Antarctica, which requires multi-layer detector geometry ($\sim$ 3000 Si(Li) detectors), in the winter of 2016-2017.

An in-house facility has been established at Columbia University for the cost-effective, mass production of Si(Li) detectors. The fabrication process is fairly simple and has been well studied since the 1960s [Goulding and Hansen, 1964; Allbritton *et al.*, 2002]. The first part of the dual track entailed flying commercially produced Si(Li) detectors (procured from SEMIKON GmbH) in order to demonstrate the goals indicated above. This demonstration only required Si(Li) detectors meeting our energy resolution requirements at altitude, and with comparable thermal properties. Using commercial detectors permitted an early flight of pGAPS, since we are just now producing our first in-house detectors (the second part of the dual track), and much work is required to optimize them. The design differences in the commercial and in-house Si(Li) detectors are not particularly profound (see below), so the

pGAPS demonstration should provide ample evidence that the in-house Si(Li) detectors will work as required on bGAPS.

3.4.2 SEMIKON and In-house Detector

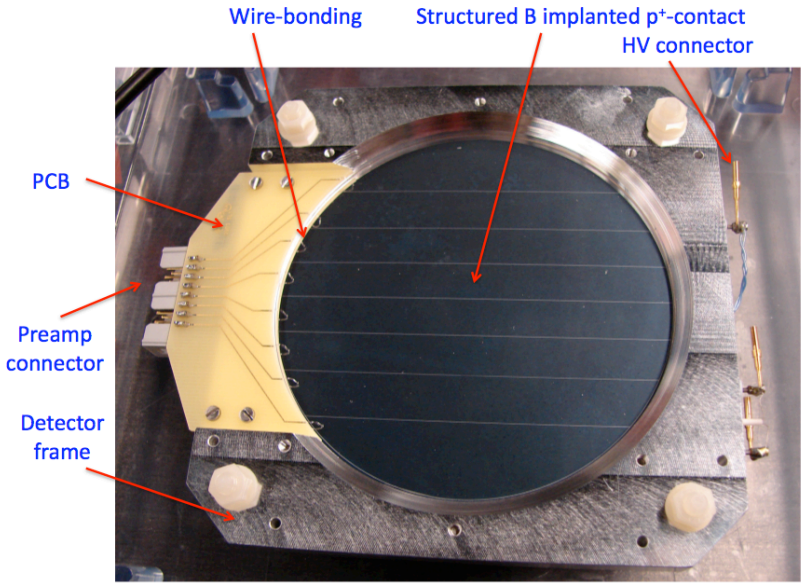

Figure 3.4: SEMIKON Si(Li) detector: 4 inch diameter, 2.5 mm thick, 4 mm guard ring, 70 cm^2 active area. The guard ring and strips are structured on the p^+ side.

The SEMIKON Si(Li) detector (Figure 3.4) has a Lithium-diffused n^+ (highly doped n-type) contact and a Boron-implanted p^+ (highly doped p-type) contact. The thickness of Boron-implanted contacts amounts to ~ 1 μm, while the specially-thinned Lithium-diffused contacts show an effective thickness of 30 μm or below, as determined by measurements with α-particles [Protic and Krings, 2002]. The noise in the detector can be characterized by the surface leakage current, the current flow without any bias voltage, which is dominated by the leakage current from the surface of the detector. A grounded guard ring, an outer peripheral region formed at the p^+ contact to suppress the leakage current, and 8 electrically independent adjacent strips (total area $\sim$ 70 cm^2) have been structured with reactive ion etching of the p^+ contact. Wire-bonding is used to connect each strip to a printed circuit board (PCB) located on the detector frame. A positive bias voltage is applied to the n^+

contact.

In contrast, the in-house detectors are somewhat simpler. The much more rugged Lithium-diffused n^+ contact is segmented into the 8 strips and a guard ring with an ultrasonic impact grinder. Each of the 8 strips and the grounded guard ring are connected to the PCB via electrodes with a simple pressure contact. A Gold contact on the p^+ side creates a Schottky barrier [Fong *et al.*, 1982], a potential barrier formed on a metal-semiconductor junction, and rectifies the current (see Figure 3.5). We note parenthetically that modern Si(Li) research attempts to achieve a simultaneous ever-finer pixel resolution and better energy resolution, for which a premium in cost is paid. The GAPS project is regressing to the early days of Si(Li) technology; the goal is to create large quantities of flight-qualified, large area, moderately thick detectors with modest energy and spatial resolution at a minimum cost.

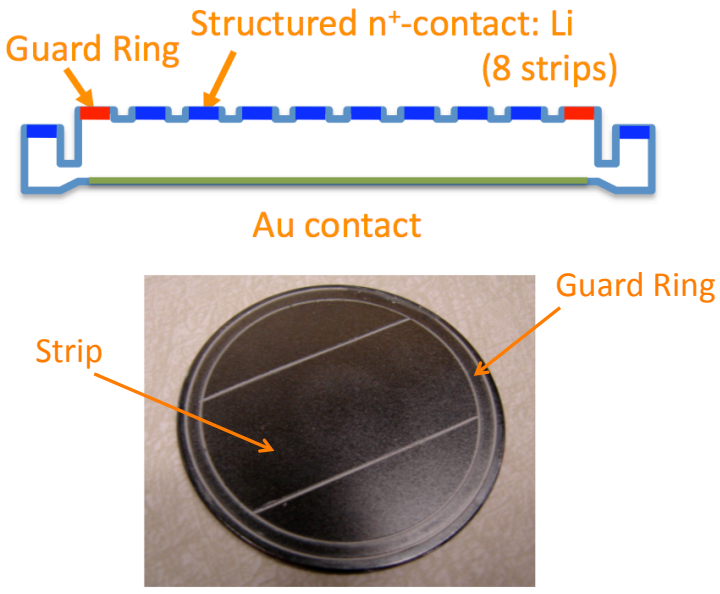

Figure 3.5: Schematic and sample picture of homemade Si(Li) detector; the sample picture is the 2 inch diameter silicon with a guard ring and 3 strips, which was ultrasonic grinded and etched in the in-house facility.

Chapter 4

Cascade Model for Exotic Atom

As discussed in the previous chapter, the X-ray yield of the exotic atom is the key to the GAPS detection concept: the energy of the atomic X-ray is unique to the exotic atom, allowing us to differentiate antideuterons from other particles, including antiprotons. The X-ray yield can be estimated using the cascade model of the exotic atom, which was developed after the existence of the exotic atom was predicted in the 1940s. We have measured the X-ray yields of antiprotonic exotic atoms at KEK, Japan with different target atoms, including Al and S targets (see Chapter 6). Unfortunately, we did not measure the X-ray yields for the Si target, which will be used in the GAPS flight experiment, since we did not envision silicon as a useful target at that time. However, since Si (Z = 14) has an atomic number between Al (Z = 13) and S (Z = 16), the results allow us to characterize the parameters and estimate the X-ray yield of the Si target. Note that since GAPS focuses on the X-ray yield at the low n state with the energy of 20 keV $<$ E $<$ 100 keV, we were able to develop a simplified cascade model as described below. The cascade model was extended to antideuteronic exotic atoms, and the X-ray yields of the antiprotonic and antideuteronic exotic atoms with a Si target were estimated to derive the ultimate GAPS sensitivity, shown in Chapter 7. In addition, the cascade model allows us to predict the X-ray yields of the exotic atom produced when the incoming antiparticle stops in other material.

4.1 Overview of the Cascade Model

A negatively charged particle (μ^-, π^-, K^-, $\bar{p}$, etc., called "cascader" hereafter) will be captured into a target atom at the radius of its outermost electrons after it slows down until its kinetic energy becomes comparable to the binding energy of the electron. The initial principal quantum number for the exotic atom can be estimated as [Hartmann, 1990; Gotta, 2004]:

$$n \sim n_e \sqrt{M^*/m_e^*} \ . \tag{4.1}$$

Here, n_e is the principal quantum number of the outermost electron shell of the target atom, m_e^* is the reduced mass of the electron in the target atom and M^* is the reduced mass of the cascader. The cascade model is designed to calculate the probability for the cascader to be in the (n, l) state, where l is the orbital angular momentum, and to estimate the X-ray yields of the exotic atom as it decays. The cascade model starts at the electron K shell ($n_e = 1$ in Eq 4.1) and the orbital angular momentum l is assumed a statistical distribution, $P_l \propto (2l+1)e^{\alpha l}$. There are $(2l+1)$ magnetic quantum numbers, $m = -l+1, -l+2 \ldots 0 \ldots l-2, l-1$, for each l, and $e^{\alpha l}$ is a correction factor due to the deexcitation at the outer shell, $n_e > 1$ ($\alpha \sim 0.2$ or less) [Hartmann, 1990; Gotta, 2004]. The initial n in the cascade model is about 14 for μ^-, 16 for π^-, 31 for K^-, and 40 for $\bar{p}$, and 60 for $\bar{d}$.

The three leading deexcitation processes, Auger transition (emission of an Auger electron), radiative transition (emission of an atomic X-ray), and nuclear capture (interaction with the nucleus), dominate the cascade model for atoms with $Z > 2$. As shown in Figure 4.1, Auger transitions dominate at the beginning of the cascade, followed by radiative transitions. The nuclear capture takes place at very low n states. Since the exotic atom can be assumed to be hydrogen-like, the Auger and the radiative transitions with $\Delta l = \pm 1$ dominate due to selection rules.

4.2 Auger Transition

In a high n state, an Auger electron is emitted as soon as the energy difference of the initial state (n_1, l_1) and the final state (n_2, l_2) exceeds the ionization energy. The Auger transition

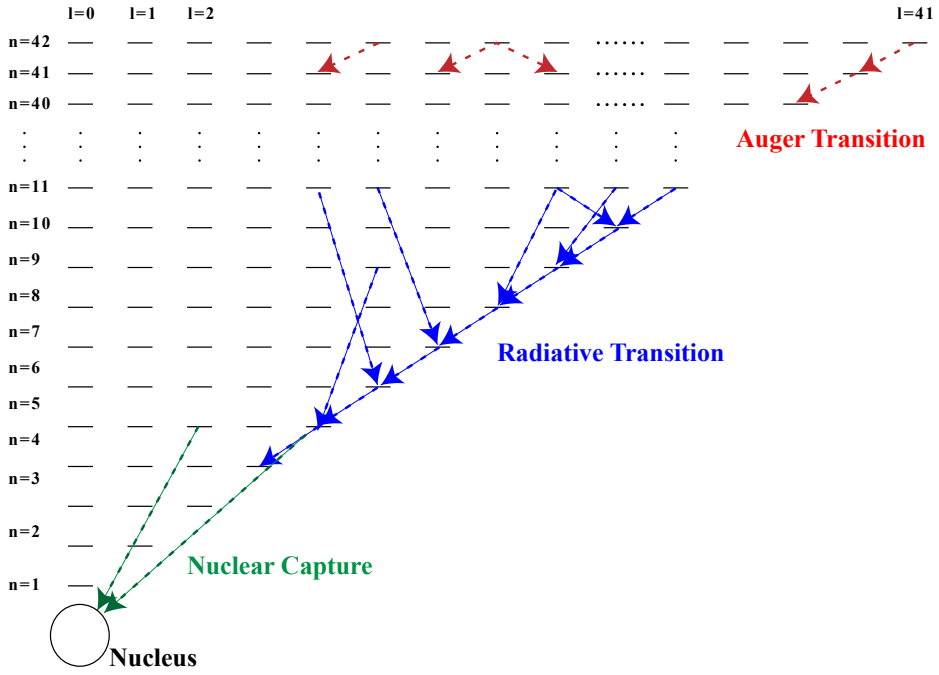

Figure 4.1: Schematic for the cascade model of the antiprotonic exotic atom. The Auger transitions dominate in high n states, while the radiative transitions dominate in low n states. The nuclear capture takes place in very low n states.

rate for the K shell and L shell electrons can be estimated by considering the interaction between the cascader and the electron as follows [Eisenberg, 1961].

$$\Gamma^{Aug,K}_{n_1,l_1\to n_2,l_2} = \frac{32\pi\alpha c}{a_0\mu^2}\left(\frac{Z^*}{Z}\right)^2 \frac{\max(l_1,l_2)}{3(2l_1+1)}\frac{y^2}{1+y^2}\frac{\exp[y(4\arctan y-\pi)]}{\sinh \pi y} I^2$$

$$\Gamma^{Aug,L}_{n_1,l_1\to n_2,l_2} = \frac{16\pi\alpha c}{a_0\mu^2}\left(\frac{Z^*}{Z}\right)^2 \frac{\max(l_1,l_2)}{3(2l_1+1)}\frac{y^2(4+5y^2)(4+3y^2)}{(4+y^2)^3}\frac{\exp[y(4\arctan y-\pi)]}{\sinh \pi y} I^2$$

Here, μ, y, and I are defined as follows.

$$\begin{aligned}
\mu &= M/m_e \\
y &\equiv \frac{Z^*\alpha}{\sqrt{(T/m_ec^2)^2 + (2T/m_ec^2)}} \\
T &\equiv \Delta E_{n_1,n_2} - E_{ionization} \\
I^2 &\equiv \int_0^\infty dr\, r^3 R(n_1,l_1)R(n_2,l_2)
\end{aligned}$$

$\Gamma^{Aug,K}_{n_1,l_1\to n_2,l_2}$ ($\Gamma^{Aug,L}_{n_1,l_1\to n_2,l_2}$) is the Auger transition rate with emitting K (L) shell electrons initial state: (n_1, l_1), and the final state (n_2, l_2), a_0 is the Bohr radius of hydrogen atom, α is the fine structure constant, Z^* is the effective nuclear charge seen from the electron, T is the kinetic energy of the emitted electron, and $R(n,l)$ is the normalized radial function of the exotic atom. The transitions with $\Delta l = \pm 1$ dominate the process, due to the transition selection rules. Note that after the electrons are depleted by the Auger transition, the electrons can be filled from adjacent atoms with a refilling rate Γ_{ref} and also from the higher shell with the fluorescence rate. The refilling rate for the noble gases can be estimated as [Hartmann, 1990]:

$$\Gamma_{ref} = n \cdot \sigma \cdot v.$$

Here, n is the density of target atoms, σ is the cross-section for charge transfer ($\sim 10^{-14}$ cm^2), and v is the relative velocity of the exotic atom with respect to other atoms of the medium ($< 10^5$ cm/s). The typical value of the refilling rate is $\sim 10^{10} s^{-1}$ for low pressure gases and $\sim 10^{16} s^{-1}$ for depleted solid and metal.

Since the Auger transition can take place only if an electron occupies a shell state, the time-dependent filling condition of the electron in each shell and the refilling rate from outside, including the electron fluorescence transition (de-excitation) from the outer shell to the inner shell, Γ_{flu}, need to be included for a more precise calculation in the cascade model [Koike *et al.*, 1996]. However, this will not affect the X-ray yield in the low n states since the radiative transition rate dominates over the Auger transition rate as n becomes smaller (see Section 6.3 and 6.5). Therefore, we simply estimate the modified Auger transition rate, including the electron refilling rate and the fluorescence transition rate, as:

$$\Gamma^{Aug,K,mod}_{n_1,l_1\to n_2,l_2} = \left(\frac{1}{\Gamma^{Aug,K}_{n_1,l_1\to n_2,l_2}} + \frac{1}{\Gamma_{ref}} + \frac{1}{\Gamma_{flu}} \right)^{-1}. \tag{4.2}$$

4.3 Radiative Transition

The radiative transition rate becomes larger than the Auger process at a relatively low n state. It can be estimated with a perturbation method and in the dipole approximation as follows [Eisenberg, 1961].

$$\Gamma^{Rad}_{n_1,l_1\to n_2,l_2} = \frac{4e^2}{3\hbar^4 c^3} \left(\frac{a_0}{\mu Z} \right)^2 (\Delta E_{n_1,n_2})^3 \frac{\max(l_1,l_2)}{2l_1+1} I^2 \tag{4.3}$$

$$\Delta E_{n_1,n_2} \equiv hcR_y \mu Z^2 \left(\frac{1}{n_1^2} - \frac{1}{n_2^2} \right)$$

Here, $\Gamma^{Rad}_{n_1,l_1\to n_2,l_2}$ is the radiative transition rate with the initial state (n_1, l_1) and the final state (n_2, l_2), and $\Delta E_{n_1,n_2}$ is the energy difference between the initial and final state, and R_y is the Rydberg constant. The transitions with $\Delta l = \pm 1$ dominate the process, due to the selection rules for the transition. The radiative transition rate increases as n decreases ($\Delta E_{n_1,n_2}$ increases), and becomes the main transition process in low n states. The radiative transitions dominate for $n < 9$ for the antiprotonic exotic atom and $n < 5$ for the muonic exotic atom. Note that the radiative transitions prefer large Δn since they are proportional to $(\Delta E_{n_1,n_2})^3$, as seen in Eq 4.3. However, once the cascader reaches the circular state, $(n, n-1)$, the selection rule restricts the transition to $(n, n-1) \to (n-1, n-2)$. Therefore, we can expect a high X-ray yield in the low n states, since the cascader is predominantly in a circular state at low n.

4.4 Nuclear Capture

Since the effective Bohr radius for the cascader, a_0/μ, is much smaller than the Bohr radius, a_0, the strong nuclear force interaction between the cascader and the nucleus can become large in low n states. This may terminate the de-excitation cascade of the exotic atom before

it reaches the ground state, since the cascader is captured by the nucleus. In particular, the antiproton and the antideuteron annihilate with the nucleus in the nuclear capture process and produce pions and protons. The optical potential between the cascader and the nucleus can be [Batty, 1981a; Batty, 1981b]:

$$\begin{aligned} U(r) &= -\frac{2\pi}{M^*}\left(1+\frac{M^*}{m_N}\right)\bar{a}\rho(r) \\ &\equiv -(V+iW)\frac{\rho(r)}{\rho(0)} \\ \rho(r) &= \frac{\rho(0)}{1+e^{\frac{r-c}{z}}}. \end{aligned}$$

Here, M^* is the reduced mass of the cascader, m_N is the mass of the nucleon, $\bar{a}$ is the average complex "effective" hadron-nucleon scatting length (experimentally determined), and $\rho(r)$ is the Fermi distribution with the parameters $\rho(0) = 0.122$ fm^3, $c = 1.07 \times A^{1/3}$ fm, and $z = 0.55$ fm [Batty, 1981a; Batty, 1981b; Wiegand, 1969].

The nuclear capture rate can be derived with the perturbation method using the imaginary part of the optical potential, W, giving.

$$\begin{aligned} \Gamma^{Cap}_{n_1,l_1} &= \frac{2}{\hbar}\int \mathrm{Im}(U(r))(R(n_1,l_1))^2 r^2 dr \\ &= \frac{2W}{\hbar}\int \frac{(R(n_1,l_1))^2 r^2}{1+e^{\frac{r-c}{z}}} dr \ . \end{aligned}$$

Here, $\hbar$ is the reduced Planck constant, $\sim 6.5 \times 10^{-16}$ eV·s, and W is ~ 30 keV (experimentally determined). Note that the energy level of the exotic atom might be slightly shifted, due to the strong nuclear force, but the shift is small for low and middle Z atoms and negligible compared with the energy of the atomic X-rays ($\Delta E_{n_1,n_2}$).

4.5 Antiprotonic Exotic Atom with Al, S and Si Targets

A Monte Carlo simulation for the antiprotonic exotic atom was developed for experimental analysis. The simulation takes into account all possible Auger transition rates and the electron refilling and fluorescence transitions, the radiative transitions, and the nuclear

capture. It starts at $n_e = 1$ in Eq 4.1 and l is determined with the modified statistical distribution, $P_l \propto (2l+1)e^{\alpha l}$ as discussed above. Antiprotons are then allowed to cascade until they are captured by the nucleus or reach the $(1,0)$ state. There are many possible Auger transitions, radiative transitions, and finite probability of nuclear capture at each state, and the probability for each transition to take place is

$$P^i_{n_1,l_1\to n_2,l_2} = \frac{\Gamma^i_{n_1,l_1\to n_2,l_2}}{\sum \Gamma^{Aug}_{n_1,l_1\to \text{any}} + \sum \Gamma^{Rad}_{n_1,l_1\to \text{any}} + \Gamma^{Cap}_{n_1,l_1}} \ .$$

Here, the initial and final states are (n_1,l_1) and (n_2,l_2) (no final state for the nuclear capture) and i is the transition type, either the Auger transition, radiative transition, or nuclear capture respectively. The simulation stores all the transitions including the quantum numbers of the initial and final states. The X-ray yields, $Y_{n_1\to n_2}$ in the low n states ($n < 9$) were also calculated as follows:

$$Y_{n_1\to n_2} = \sum_{l_i=0}^{n_1-1} \sum_{l_j=0}^{n_2-1} \frac{N_{n_1,l_i}}{N_{\text{all}}} P^{Rad}_{n_1,l_i\to n_2,l_j}.$$

Here, N_{all} is the number of antiprotons simulated in the cascade model and N_{n_1,l_i} is the number of antiprotons that cascaded to the state (n_1,l_i).

Tables 4.1 and 4.2 show the simulation results of the X-ray yields, $Y_{5\to4}$, $Y_{6\to5}$, $Y_{7\to6}$, $(Y_{8\to7})$, for the antiprotonic exotic atom with Al and S targets. The energies of these atomic X-rays are within the energy range of the KEK detector (25 keV < E < 300 keV). The experimental data taken at KEK (see Chapter 6) are also shown in the tables. The

Transition	Energy	Cascade Model	Exp Data
$5 \to 4$	92 keV	0.46	0.87 ± 0.14
$6 \to 5$	50 keV	0.81	0.79 ± 0.13
$7 \to 6$	30 keV	0.69	0.86 ± 0.14

Table 4.1: X-ray yields and experimental data for antiprotonic exotic atom with Al target.

tentative parameters used here are $\alpha = 0.16$ (coefficient for the initial angular momentum

Transition	Energy	Cascade Model	Exp Data
$5 \rightarrow 4$	139 keV	0.17	0.41 ± 0.31
$6 \rightarrow 5$	76 keV	0.78	0.77 ± 0.21
$7 \rightarrow 6$	46 keV	0.70	0.77 ± 0.21
$8 \rightarrow 7$	30 keV	0.52	0.77 ± 0.21

Table 4.2: X-ray yields and experimental data for antiprotonic exotic atom with S target.

distribution), $W = 30$ MeV (the imaginary part of the optical potential) and $\Gamma_{ref} = 10^{16} s^{-1}$ (electron refilling rate), which are derived from the equations in the previous sections.

The parameter dependencies of the X-ray yield for the Al target are shown in the tables below. Table 4.3 shows the results for different values of α with $W = 30$ MeV and $\Gamma_{ref} = 10^{16} s^{-1}$, while Table 4.4 shows the results for different values of W with $\alpha = 0.16$ and $\Gamma_{ref} = 10^{16} s^{-1}$. The results for different values of Γ_{ref} with $\alpha = 0.16$ and $W = 30$ MeV are shown in Table 4.5.

Transition	Energy	$\alpha = 0$	$\alpha = 0.04$	$\alpha = 0.08$	$\alpha = 0.12$	$\alpha = 0.16$	$\alpha = 0.2$
$5 \rightarrow 4$	92 keV	0.29	0.34	0.40	0.43	0.46	0.47
$6 \rightarrow 5$	50 keV	0.46	0.59	0.69	0.76	0.81	0.85
$7 \rightarrow 6$	30 keV	0.37	0.48	0.58	0.63	0.68	0.71

Table 4.3: X-ray yields for the Al target with different values of α with $W = 30$ MeV and $\Gamma_{ref} = 10^{16}$ s^{-1}.

Transition	Energy	$W = 0$	$W = 10$	$W = 30$	$W = 50$	$W = 70$	$W = 90$
$5 \rightarrow 4$	92 keV	0.88	0.67	0.46	0.34	0.28	0.24
$6 \rightarrow 5$	50 keV	0.82	0.81	0.82	0.81	0.82	0.82
$7 \rightarrow 6$	30 keV	0.69	0.69	0.68	0.68	0.69	0.69

Table 4.4: X-ray yields for the Al target with different values of W in MeV with $\alpha = 0.16$ and $\Gamma_{ref} = 10^{16}$ s^{-1}.

As seen in the tables above, α changes the yields of all three transitions, while W only changes the yield of the last transition ($5 \rightarrow 4$), as expected. Since $\Gamma^{Aug,mod}$ can be expressed

Transition	Energy	$\Gamma_{ref} = 10^4$	$\Gamma_{ref} = 10^8$	$\Gamma_{ref} = 10^{12}$	$\Gamma_{ref} = 10^{16}$	$\Gamma_{ref} = 10^{20}$
$5 \to 4$	92 keV	0.50	0.50	0.51	0.46	0.46
$6 \to 5$	50 keV	0.97	0.97	0.96	0.81	0.81
$7 \to 6$	30 keV	0.95	0.96	0.94	0.68	0.68

Table 4.5: X-ray yields for the Al target with different values of Γ_{ref} in s^{-1} with $\alpha = 0.16$ and $W = 30$ MeV.

as in Eq 4.2 and strongly depends on Γ_{flu}, the yields increase as Γ_{ref} becomes smaller than $\Gamma_{flu} \sim 10^{12}$, while it will not decrease as Γ_{ref} becomes larger than Γ_{flu}. Considering the above, W can be determined by the ratio of $Y_{5\to4}$ to $Y_{6\to5}$, while α can be determined by the value of $Y_{6\to5}$ and $Y_{7\to6}$. We can also assert that $\Gamma_{ref} \sim 10^{16}$ is reasonable. Therefore, the optimized parameters are $\alpha \sim 0.16$, $W < 10$ MeV and $\Gamma_{ref} \sim 10^{16}$ s^{-1}.

Transition	Energy	$\alpha = 0$	$\alpha = 0.04$	$\alpha = 0.08$	$\alpha = 0.12$	$\alpha = 0.16$	$\alpha = 0.2$
$5 \to 4$	139 keV	0.11	0.14	0.16	0.16	0.16	0.17
$6 \to 5$	76 keV	0.48	0.55	0.65	0.72	0.77	0.82
$7 \to 6$	46 keV	0.36	0.47	0.57	0.63	0.69	0.79
$8 \to 7$	30 keV	0.28	0.36	0.43	0.49	0.53	0.57

Table 4.6: X-ray yields for the S target with different values of α with $W = 30$ MeV and $\Gamma_{ref} = 10^{16}$ s^{-1}.

Transition	Energy	$W = 0$	$W = 10$	$W = 30$	$W = 50$	$W = 70$	$W = 90$
$5 \to 4$	139 keV	0.86	0.34	0.16	0.11	0.09	0.07
$6 \to 5$	76 keV	0.79	0.79	0.77	0.77	0.75	0.75
$7 \to 6$	46 keV	0.70	0.70	0.69	0.70	0.69	0.69
$8 \to 7$	30 keV	0.54	0.55	0.53	0.55	0.54	0.55

Table 4.7: X-ray yields for the S target with different values of W in MeV with $\alpha = 0.16$ and $\Gamma_{ref} = 10^{16}$ s^{-1}.

The results for the parameter studies of the α and W dependencies of the antiprotonic exotic atom with the S target, are shown in Tables 4.6 and 4.7, which also indicate that the

optimized parameters are $\alpha \sim 0.16$, $W \sim 10$ MeV and $\Gamma_{ref} \sim 10^{16}$ s^{-1}.

Transition	Energy	Cascade Model
$5 \rightarrow 4$	106 keV	0.57
$6 \rightarrow 5$	58 keV	0.80
$7 \rightarrow 6$	35 keV	0.69

Table 4.8: X-ray yields for the antiprotonic exotic atom with the Si target.

The X-ray yields for the antiprotonic exotic atom with the Si target were estimated using the parameters for the Al and S targets, since Si (Z= 14) is close to Al (Z = 13) and S (Z =16) in the period table of elements and we can expect that they have similar atomic properties. The result with the parameters, $\alpha = 0.16$, $W = 10$ MeV, and $\Gamma_{ref} = 10^{16} s^{-1}$, is shown in Table 4.8.

4.6 Prediction for Antideuteronic Exotic Atom for Si Target

The X-ray yields of the antideuteronic exotic atom with a Si target were also estimated using the Monte Carlo simulation discussed above. The cascade model for the antideuteronic exotic atom was established simply by changing the mass in the antiprotonic model and assuming $W_{\bar{d}} \sim 2W_{\bar{p}}$. The simulation results for the yields $n < 9$ are shown in Table 4.9.

Line	Energy	Yield
$5 \rightarrow 4$	206 keV	0.14
$6 \rightarrow 5$	112 keV	0.83
$7 \rightarrow 6$	67 keV	0.81
$8 \rightarrow 7$	44 keV	0.76
$9 \rightarrow 8$	30 keV	0.65

Table 4.9: X-ray yields for antideuteronic exotic atom with Si target.

Since the GAPS Si(Li) detector is sensitive by design to the energy range of 20 keV $< E <$ 80 keV, three X-ray transitions, $7 \rightarrow 6$, $8 \rightarrow 7$ and $9 \rightarrow 8$, can be detected and used for antideuteron identification in the GAPS experiment. As seen in Table 4.9, we

can expect relatively high yields, $\sim$ 75 %, for these X-rays. Note that the yields are less sensitive to α compared with the lighter cascader since the initial principal quantum number of the antideuteronic exotic atom is higher, $\sim$ 60, and the antideuteron can be in a more circularized state ($l = n-1$) at low n. In contrast, the nuclear capture takes place at higher n than for the lighter cascaders since the modified Bohr radius for the antideuteronic atom is smaller. In any case, the nuclear capture can only take place at $n = 5$ or less and it will not affect the yields of the three X-rays of interest. Overall, the simulation results show higher X-ray yields than were assumed in [Mori *et al.*, 2002], thus increasing the GAPS sensitivity to the antideuteron detection.

Chapter 5

KEK Beam Test for GAPS Prototype Detector

5.1 Overview of the Experiment

Antiprotonic exotic atoms have been studied for many years at the CERN low energy antiproton ring (LEAR) [Batty and Friedman, 1984; Nakamura *et al.*, 1984; Amsler, 1998], but none of the experiments have focused on the measurement of the absolute X-ray yield, the probability of atomic X-rays to be emitted in the decay of the exotic atom. As discussed in Chapter 4, GAPS utilizes the atomic X-rays of the exotic atom to distinguish antideuterons from other antimatter, and the measurement of the X-ray yield is crucial to the GAPS detection method. Therefore, we conducted beam tests at KEK in Japan in 2004 and 2005 to measure the X-ray yields of the antiprotonic exotic atom with several different target materials. The results constrain the parameters in the cascade model described in Chapter 4, which can be applied to estimate the X-ray yield of the antideuteronic exotic atom with a Si target in the GAPS flight experiment.

The KEK (high energy accelerator research organization) facility is located north of Tokyo, in Tsukuba, Japan. During the course of the experiments the proton synchrotron produced an 8 GeV (up to 12 GeV) proton beam in a main ring. The H^- ion source generated in the plasma chamber was injected into the pre-injector, followed by the linac, booster synchrotron and main ring and accelerated to 750 keV, 40 MeV, 500 MeV and 8

GeV, respectively. Our experiment was performed at the $\pi 2$ secondary beam line, which delivers copious particles generated by the proton beam hitting an internal target in the main ring. The momentum of the beam was controlled and focused by dipole and quadrupole magnets, while the momentum spread was also controlled by a shutter. The particles were delivered in 1.5 s long spills, and each spill was separated by a 4 s interval. A momentum of 1 GeV/c was chosen to optimize the antiproton flux, considering that more antiprotons annihilate in flight as the momentum increases. The beam with a momentum of 1 GeV/c contained about 20-30 antiprotons, 10^5 π^-, and a somewhat smaller number of K^- and e^-, as measured in the 2004 experiment, and these numbers were consistent with the data sheets provided by KEK.

The GAPS instrument in the KEK test was composed of a TOF, degraders (lead brick and sheets), Cherenkov/shower counters, a target and X-ray detectors. The antiprotons in the beam were first identified by the TOF system, since antiprotons are slower than the other particles in the beam. The degrader slowed down the particles and stopped them in the target material where they formed an excited antiprotonic exotic atom. Atomic X-rays and charged particles are emitted in the decay of the exotic atom as discussed in the previous chapter. A Sodium Iodide doped with Thallium, Nal(Tl), detector array was installed around the target material and detected the atomic X-rays and a few pions. The Cherenkov/shower counters monitored the Cherenkov light/energy deposited by the particles in the beam and distinguished antiprotons from other particles, including the in-flight annihilation products.

In 2004, we were not able to obtain enough data to accurately measure the X-ray yields. In addition, the performance of the TOF trigger system was not sufficient to identify antiprotons, since many of the triggered antiprotons annihilated in flight and generated accidental events. Therefore, in 2005, another TOF scintillation counter was installed between the P0 and P2 counters. We also replaced the Cherenkov counter with more cost effective shower counters to enhance the particle identification. The schematics of the experimental setup in 2004 and 2005 are shown in Figures 5.1 and 5.2.

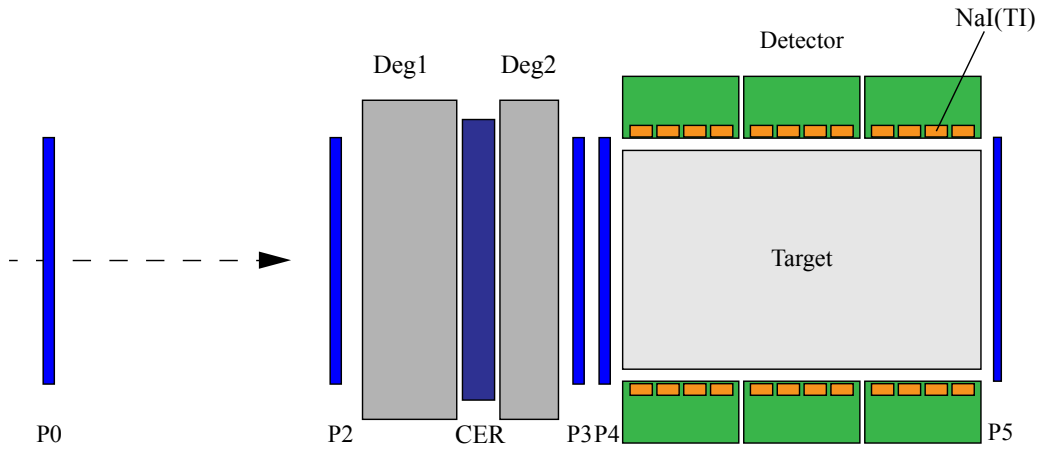

Figure 5.1: Experimental setup at KEK in 2004.

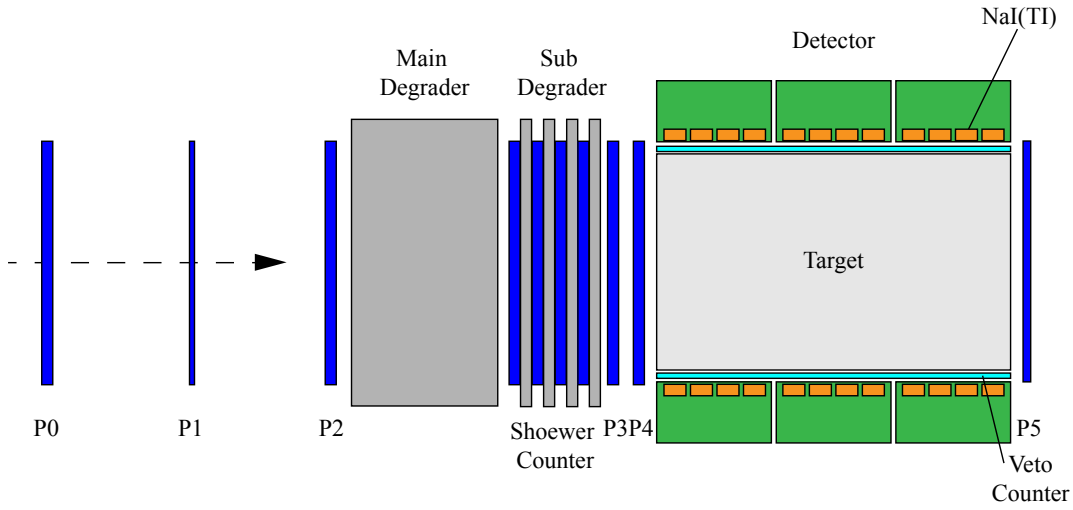

Figure 5.2: Improved experimental setup at KEK in 2005. The Cherenkov counter was replaced with the shower counters.

5.2 Instrumental Setup

5.2.1 Time of Flight

The TOF system in the KEK 2005 (2004) test was composed of 6 (5) scintillation counters, P0-P5 (no P1 in 2004). The TOF timing, the travel time of the incoming particle between the P0 and Pi ($i = 1, 2, 3, 4, 5$) counters, allowed us to identify the incoming particle, since all the particles in the beam had a fixed momentum and the antiproton was much slower than the other lighter particles (see Section 7.3). The P0, P2, P3 and P4 counters each had a dimension of 12 cm $\times$ 12 cm and a thickness of 1.0 cm, while the P1 and P5 counters had a thickness of 0.2 cm. The paddles were coupled to the light guide and then to the 2 inch fast photomultiplier tube (Photonics XP2020). A high voltage of $\sim$ 800V was applied to the PMT base (Photonics S5632).

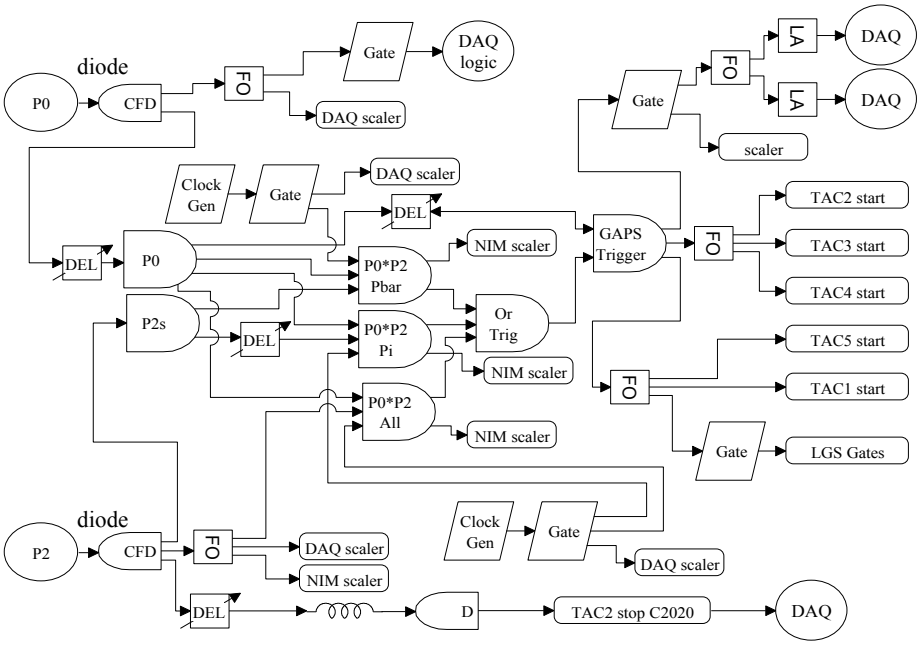

Figure 5.3: Block diagram of the electronics for the P0 and P2 counters

While the P0, P1, and P2 counters measured only the TOF timing, the P3, P4 and P5 counters read for both the TOF timing and the dE/dX energy deposit, as seen in Figures 5.3 and 5.4. The TOF timing was read at the last diode with a fast timing preamplifier

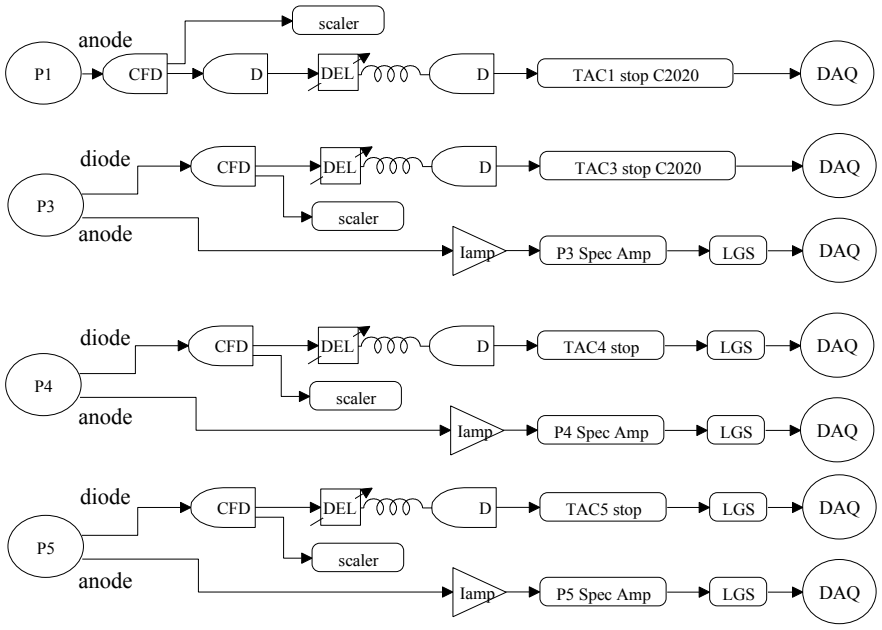

Figure 5.4: Block diagram of the electronics for the P1, P3, P4 and P5 counters. Each scintillation counter provided the TOF timing and dE/dX energy deposit.

(Ortec VT120b), followed by a time-to-analog converter (Canberra 2020), while the dE/dX energy deposit was read at the anode with a preamplifier (Camberra 2005), followed by a spectroscopy amplifier (Ortec 452). As discussed above, another TOF module, P1, was installed between the P0 and P2 counters in 2005 to obtain additional TOF timing to distinguish antiprotons from others.

5.2.2 Cherenkov Counter and Shower Counter

The Cherenkov Counter (12 cm $\times$ 12 cm $\times$ 2 cm, coupled to a PMT) was mounted between the degraders in 2004 to distinguish antiprotons from other light particles. Since all the particles in the beam had a fixed momentum, 1 GeV/c, the lighter particles such as π^- were relativistic and emitted Cherenkov light. In contrast, since antiprotons in the beam were not relativistic, they did not trigger the Cherenkov counter. The Cherenkov counter also triggered the event when antiprotons annihilated in flight, since relativistic pions were produced in the annihilation. However, since the Cherenkov counter was hard to maintain

and we also needed to monitor the interaction of the antiproton in the sub degrader for better particle identification, we replaced the Cherenkov counter with four shower counters, S1-S4 (see Figures 5.1 and 5.2).

The four shower counters were installed behind the main degrader in 2005, and each of them had a dimension of 12 cm $\times$ 12 cm $\times$ 0.5 cm. A 0.25 inch lead sheet was sandwiched between every pair of counters to slow down the incoming particle. Each counter was coupled to the light guide and PMT (Photonics 2042 and 2072 PMT). The charge sensitive preamp was integrated on the PMT base to enhance the signal. The shower counter allowed us to distinguish the antiproton from other particles by measuring the dE/dX energy loss, since non-relativistic slow antiprotons deposit more energy than relativistic particles.

Additionally, the veto counters (6 cm wide, 1 mm thick ribbon scintillation fibers, coupled to a Hamamatsu R1942A 1 inch PMT) were installed between the target and the X-ray detectors in 2005. They were designed to monitor the off-axis antiprotons hitting the detector and the frame without stopping in the target material.

5.2.3 X-ray Detector

The X-ray detectors were composed of 128 NaI(TI) crystals (1 inch $\times$ 1 inch $\times$ 5 mm). The NaI(TI) detector has been widely used as a scintillation detector, and it emits scintillation light proportional to the deposited energy, $\sim$ 40 photons/keV. Since the NaI(Tl) is a relatively high Z material, up to 300 keV X-rays can be photo-absorbed in the 5 mm thick crystal. Each crystal is coupled to a Hamamatsu 1 inch PMT (R1924A) on the back surface. The wavelength of the scintillation light is $\sim$ 410 nm, where the quantum efficiency of the PMT has a peak. Every 8 crystals and PMTs, separated from each other by 1.5 inch, are mounted in a tightly sealed steel housing with a 0.125 mm Al window as seen in Figure 5.5. Each PMT is connected to the custom made PMT base and $\sim$ -800V HV was applied. The preamplifier was mounted inside the housing and the gain for each detector was controlled by the knob ouside the housing. 16 sets of detectors were mounted around the target as seen in Figure 5.6.

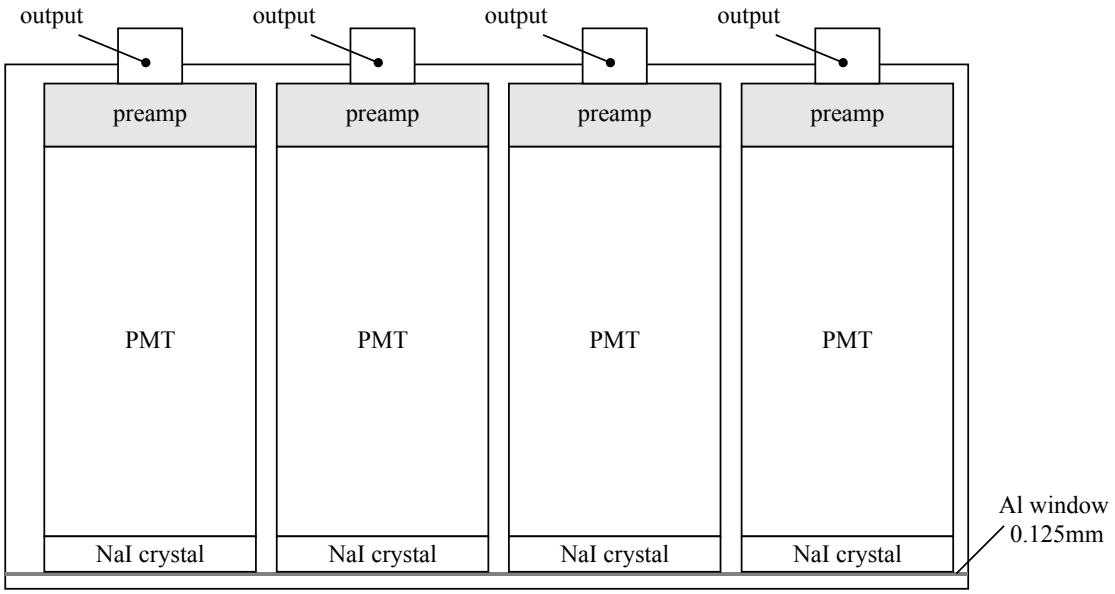

Figure 5.5: NaI(Tl) detector housing. The NaI crystal is coupled to the PMT followed by the preamplifier.

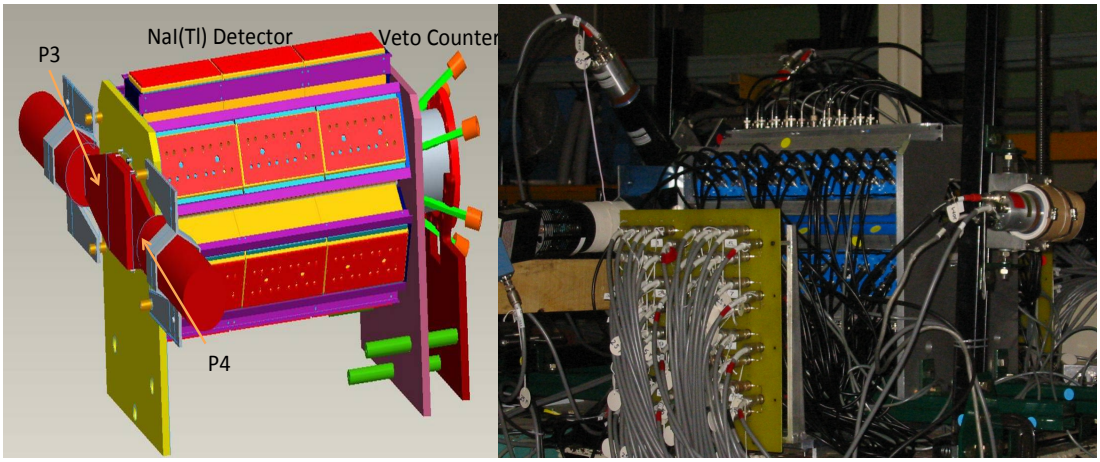

Figure 5.6: Schematic (left) and actual picture (right) for NaI detector array.

5.2.4 Trigger System and DAQ Electronics

The trigger system in the GAPS instrument at KEK was set for each particle (antiproton, π^-, or all) using the proper TOF timing between the P0 and P2 counters, as seen in Figure

5.3. Since each particle had different TOF timing, based on the mass as discussed above, we can selectively choose the incoming particle. The trigger signal, called "GAPS Trigger", was produced by coincident signals at the P1 and P2 counters with the proper TOF timing and sent to the DAQ system. The stretched "GAPS Trigger" was also used for the gate in all time-to-amplitude conversion (TAC) and linear gate and stretcher (LGS) units. The signal in the X-ray detector was recorded when the signal was acquired within a certain time window, called "GAPS Allow". The time window of "GAPS Allow" was set to 500 ns. The leading edge of "GAPS Allow" was generated based on "GAPS Trigger" and the delay due to the data processing time including the travel time, called "GAPS Delay". The optimized "GAPS Delay" was measured using the pulse generator for the outputs of the P0 counter and the X-ray detector, and it was around 1.6 μs. The timing diagrams for "GAPS Trigger", "GAPS Delay", and "GAPS Allow" are illustrated in Figure 5.7. The TOF timing and the dE/dX energy deposit of the triggered event were converted into the pulse height signal and sent to the DAQ system. The block diagram of the electronics is shown in Figure 5.4.

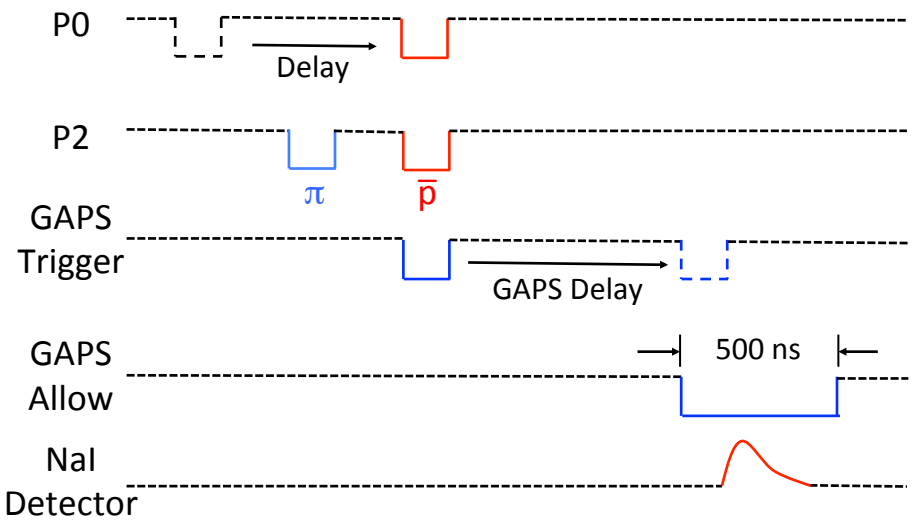

Figure 5.7: Timing diagram for antiproton events

The GAPS DAQ electronics were developed by Lawrence Livermore National Laboratory

(LLNL). There were two chassis, each with 64 ADC cards installed for the signal from the NaI detector and one ADC board to read the signals for the trigger, the TOF timing and dE/dX energy deposit. The digital back end on the chassis communicated with the PC through a National Instrument DAQ board (PCI6534). The backend PC could adjust the GAPS Allow and GAPS Delay on the DAQ system by a software command.

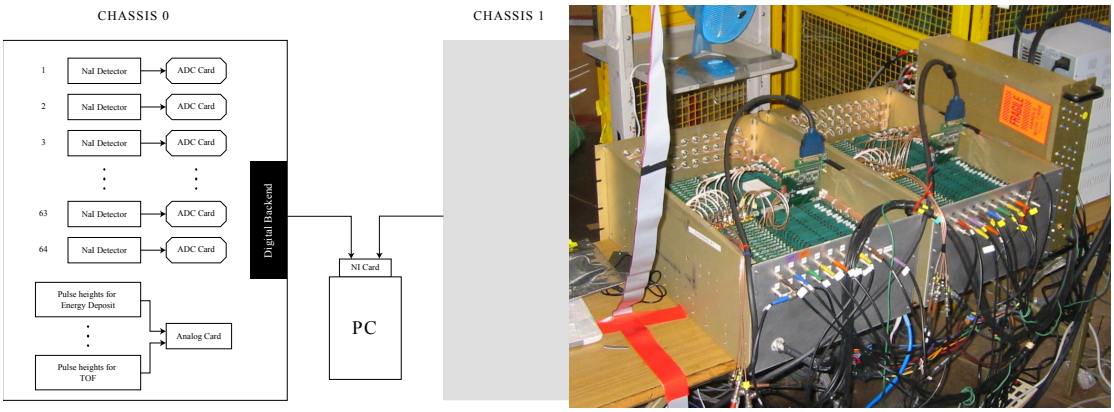

Figure 5.8: DAQ System and backend PC. Schematic (left) and real picture (right)

There are two DAQ modes in the system: a free run mode to record all the data in the NaI detector and a trigger run mode to record the data in coincidence with "GAPS Trigger". In the trigger mode, the DAQ can handle the data up to 1.5k events per spill with event reconstruction, and the NIM counter was setup to monitor the count rate of the first 10 beam spills for each run.

5.2.5 Target Material

In 2004 and 2005, six targets had their antiprotonic atom X-ray yields measured. The target materials were chosen based on the energy of the atomic X-rays in their antiprotonic exotic atom, which needed to be in the useful energy range of the X-ray detector, 25 keV $<$ E $<$ 300 keV. The detectable antiprotonic atomic X-rays for each target tested in KEK are shown in Table 5.1.

The carbon aerogel and C_2F_6 gas were tested in 2004 with minimal results due to the

Table 5.1: Antiprotonic atomic X-rays for each target (25 keV < E < 300 keV)

Target	highest X-ray	2nd highest	3rd	4th	5th	6th
Al	92 keV	50 keV	30 keV	-	-	-
S	139 keV	76 keV	46 keV	30 keV	-	-
Cl	86 keV	52 keV	34 keV	23 keV	-	-
Br	145 keV	99 keV	71 keV	52 keV	41 keV	31 keV

imperfection of the trigger system as discussed above. The carbon aerogel has a density of 0.28g/cm^3 packed into two blocks with a dimension of approximately 12 cm in diameter and 23 cm in length. The two blocks were wrapped with a layer of heat shrink plastic film, estimated to be $\sim$ 0.5 mm thick, to prevent contamination by moisture and dust. The C_2F_6 gas was contained in a capsule container made of 5 mm thick carbon fiber to minimize the X-ray absorption in the wall. The capsule was split into 2 domes: a front window shaped with CFRP to minimize the mass in front of the target and a back window made of stainless steel with gas outlets to reinforce the container.

The Al (Aluminum wool), S (Sulfur), CBr_4 (Tetrabromomethane) and CCl_4 (Carbon tetrachloride) targets were tested in 2005. The Al wool was filled into two 1 mm thick plastic bottles, each with a diameter of 12 cm and 22 cm in length, and the average density was $\sim$ 0.111g/cm^3. The target holders for the Sulfur powder and CBr_4 crystals are framed with Al pipes of diameter 12 cm cut at a 45 degree angle, and both openings were covered with 1 mm thick plastic sheets as seen in Figure 5.9. The holders were placed onto two guided rails to minimize the blockage of X-rays from the target. The CCl_4 was also filled inside the Al frame covered with the plastic sheets. However, the plastic sheet reacted with the CCl_4 and 20% $\sim$ 30% of the CCl_4 was found to have leaked/evaporated during the run.

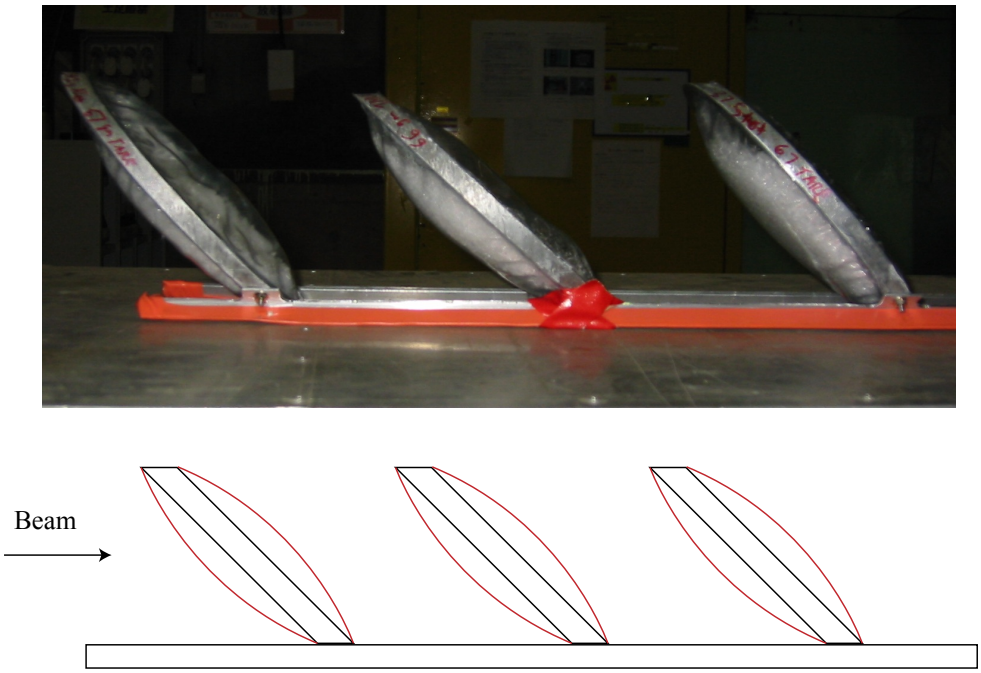

Figure 5.9: Sulfur and CBr_4 target geometry

Chapter 6

Data Analysis for KEK Beam Test

6.1 Overview

The X-ray yields of the antiprotonic exotic atom were measured with different targets at KEK in 2004 and 2005. Some of the data in 2004, however, were contaminated by accidental events, and we were not able to distinguish antiprotons from other particles in the beam. This issue was resolved by adding another plastic paddle in the TOF system in the following year. The liquid and solid targets were used in 2005 rather than the gas target, since they did not require an additional bulky complex to hold and there is more flexibility to design a geometry for a liquid and solid targets. Since Si is $Z = 14$, between Al ($Z = 13$) and S ($Z = 16$) in the periodic table of elements, we expect that the X-ray yields for the Al and S targets will be similar to that for the Si target that will be used in the GAPS balloon experiment. The data analysis is described in this chapter, especially focusing on the Al and S targets. Note that X-ray yields for the compound targets, CCl_4 and CBr_4, are more complicated since the antiproton can stop and form an exotic atom with each atom in the compound. Therefore, they produce many X-rays, making it difficult to distinguish them from each other. Additionally, a leak was found during the measurement on the CCl_4 target, which makes it even more difficult to analyze the X-ray yields.

The GEANT4 (geometry and tracking) simulation software was used to define the beam trajectory and to estimate the X-ray yields. The simulation allowed us to evaluate the cuts for the particle selection at each counter by using the TOF timing and dE/dX energy

deposit.

6.2 Beam Profile

The GAPS prototype detector was tested on the $\pi 2$ secondary beam line at KEK, where the antiparticles were produced from 8 GeV protons hitting a target in the main ring. The intensity of each particle in the beam was measured by using the TOF timing between the P0 and the P2 counters with a multichannel analyzer. The travel time between the P0 and the P2 counters was estimated to be $\sim$ 30 ns for antiprotons, while it was $\sim$ 22 ns for pions. There were $\sim 10^5$ pions (π^-) and $\sim$ 20 antiprotons in each spill. The spatial beam profile at the P0 counter was measured by changing the last dipole magnet, which controlled the horizontal direction, and the height of the remote controlled table (for the vertical direction). The beam profiles, spatial distributions at the P0 counter, with two different shutter openings in the beam line are shown in Figures 6.1 and 6.2.

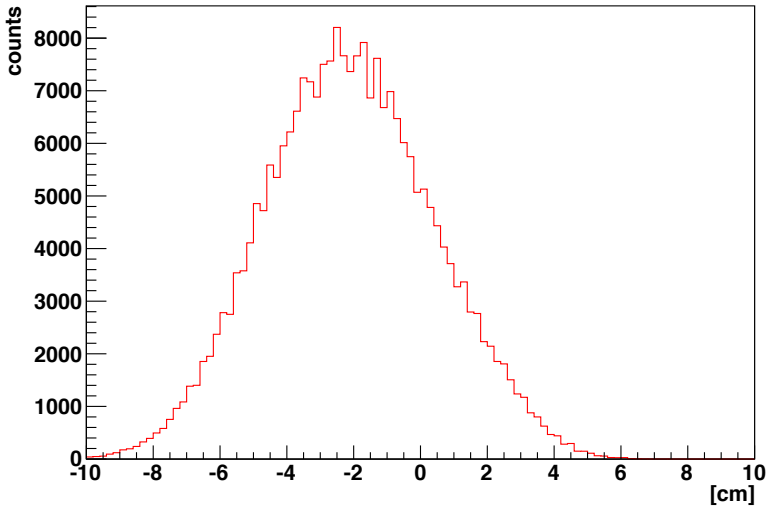

Figure 6.1: Horizontal beam profile at P0 counter.

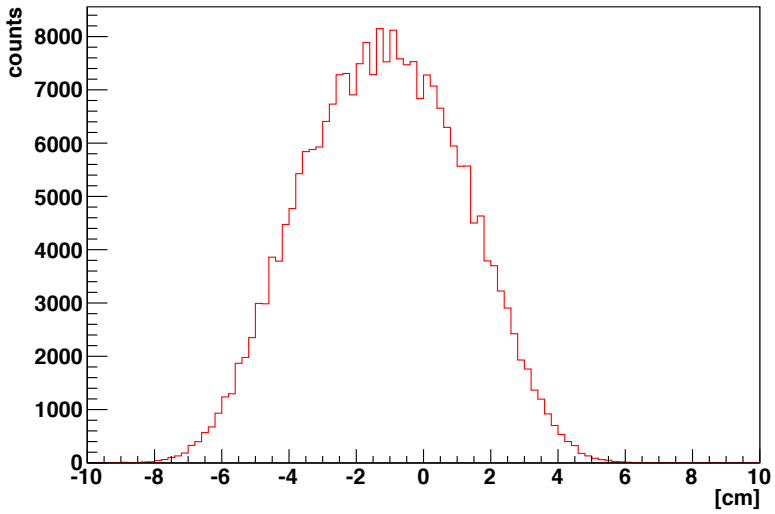

Figure 6.2: Vertical beam profile at P0 counter.

6.3 Range Curve

Since antiprotons in the beam were too energetic to stop in the target, we installed lead bricks and sheets on the beam axis as a degrader to slow them down. The optimized total thickness of degrader was estimated by measuring the number of events at the P4 counter (just before the target) with different thicknesses of degrader. Since the number of antiprotons in the beam was very small, in order to have better statistics, we used positively charged beam (protons and π^+) with the same magnet settings for the beam except for the polarity. The number of proton events at the P4 counter rapidly decreased as the thickness of the degrader increased to $\sim$ 10.3 cm, which implies that there were many slow protons present at the P4 counter with this thickness (see Figure 6.3). Therefore, we decided to use a total thickness of the degrader of 10.3 cm in the experiment.

6.4 Detector Calibration

6.4.1 X-ray Detector

The NaI(Tl) detector was calibrated with ^{241}Am and ^{133}Ba sources before and after each run. ^{241}Am decays (via α decay) and emits characteristic X-rays, 20 keV (Kα of Np atom)

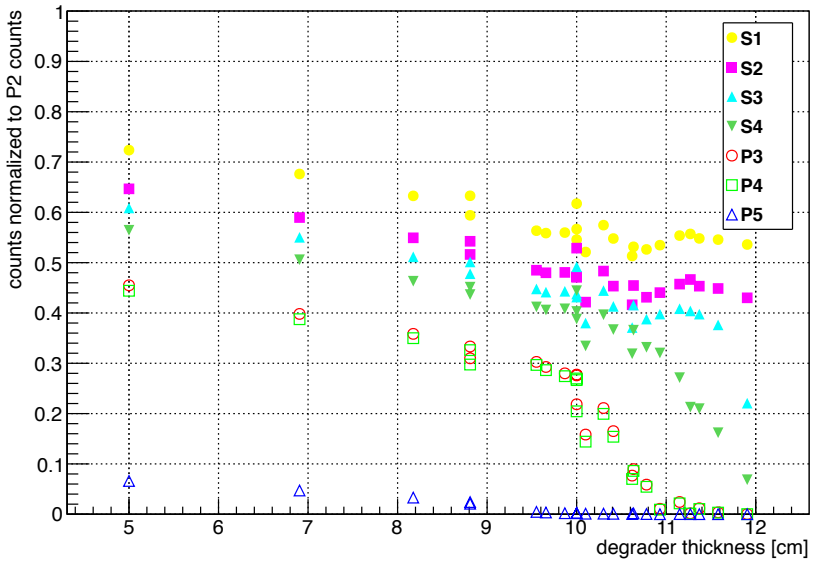

Figure 6.3: Number of hits at each counter vs. degrader thickness (cm). The counts were normalized to the counts at P0 counter.

and 59.5 keV, while ^{133}Ba ($\beta+$ decay) emits 31 keV (Kα of Cs atom), 80 keV, and 133 keV X-rays in the detectable energy range. Note that the energy of the X-ray may not be completely deposited in the detector after it is photo-absorbed, since the atomic X-rays emitted in the subsequent deexcitation of photo-ionized atom may escape from the target. Therefore, the partial energy deposit peak due to this phenomenon, called the escape peak, can be seen at the energy of $(E_{photon} - E_{i,\alpha})$, where $E_{i,\alpha}$ is the k-edge X-ray. The escape peaks are at 31 keV for the ^{241}Am source and 51 keV and 104 keV for the ^{133}Ba source.

Since NaI(Tl) crystal and electronics are sensitive to the temperature, the gain of the X-ray detector drifted during the measurement. We periodically evaluated the gain drift by using the X-ray sources and it was fitted with a function of the temperature for each crystal and electronics changes as below.

$$P = c + (a + bT)E$$

Here, P is the peak energy, a, b, and c are fit parameters, T is the temperature of the detector and E is the energy of the X-ray.

6.4.2 TOF System

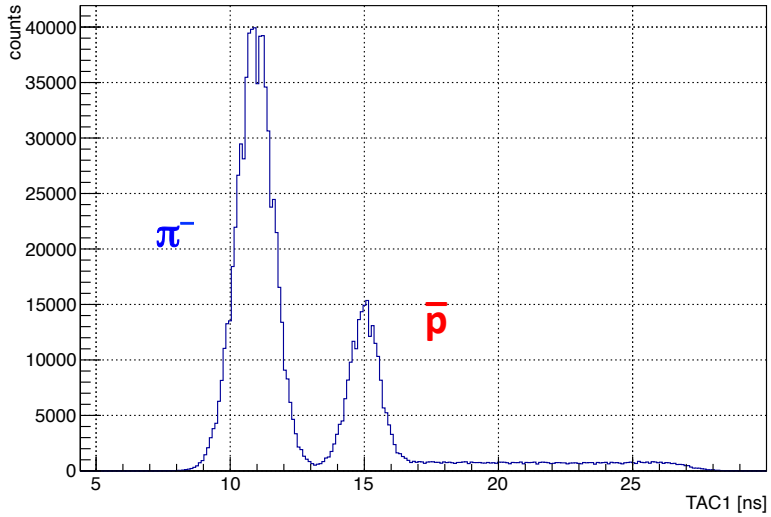

Figure 6.4: The TOF timing at TAC1.

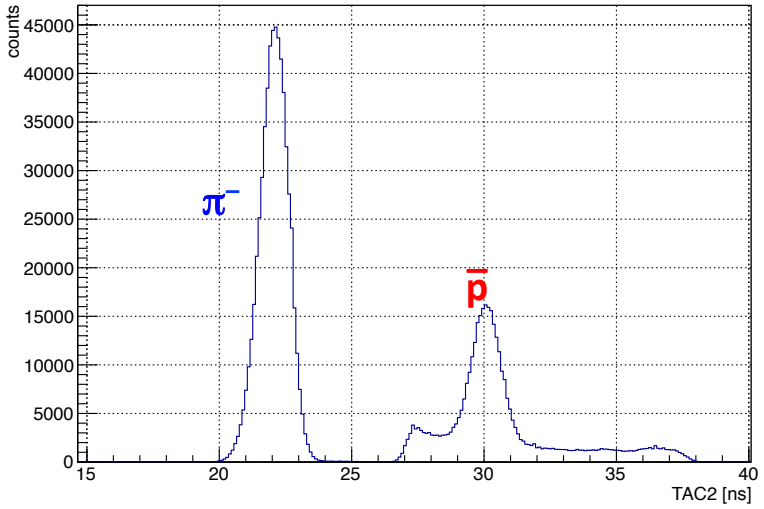

Figure 6.5: The TOF timing at TAC2.

The timing information at each TOF counter (P1-P5) was calibrated by using a pulse generator and changing the delay on the TAC module. The results showed excellent linearity and the output of each TAC scaled into time (ns). The noise contribution from the

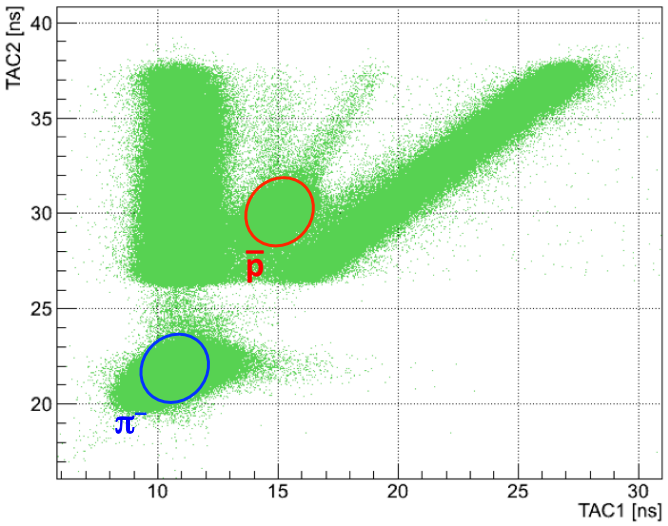

Figure 6.6: 2-dimensional TOF timings, TAC1 (between P0 and P1) vs. TAC2 (between P0 and P2).

electronics was estimated as less than 150 ps in all TACs. Figures 6.4 and 6.5 show the TOF timing, TAC1 (between P0 and P1) and TAC2 (between P0 and P2), for antiprotons and pions in the beam. The peak on the left is for pions, while the peak on the right is for antiprotons. The timing offset was adjusted by using the GEANT4 simulation (see Section 7.5). Figure 6.6 shows the 2-dimensional scatter plot of TAC1 vs. TAC2. The peak for antiproton events is at (TAC1, TAC2) = (15 ns, 30 ns), while the peak for the pion events is at (11 ns, 22 ns).

Figures 6.7, 6.8, and 6.9 also show the TOF timing of antiprotons and pions at TAC3, TAC4, and TAC5. Note that since most of the antiprotons were not able to reach the P5 counter, the signals were either due to the pions in the beam or the antiproton annihilation products. As seen in the figures, the peaks for pions and antiprotons were distinctive and we can distinguish antiprotons in the beam by applying the proper cuts on the TOF timing at each counter (see Section 7.6).

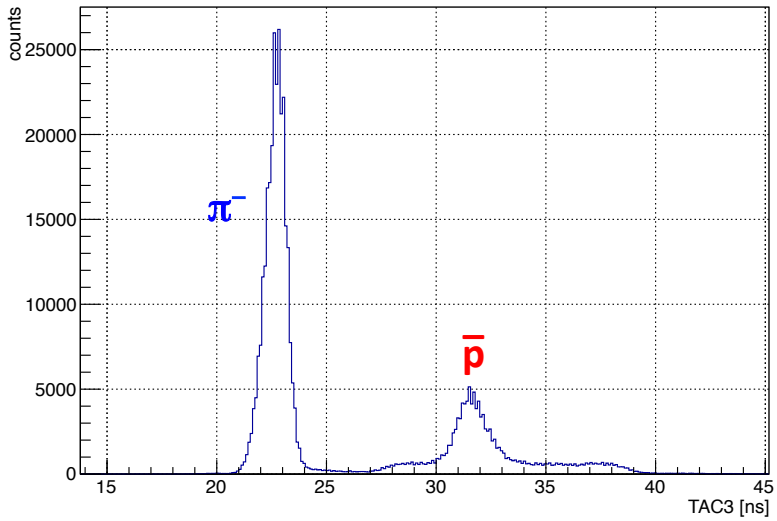

Figure 6.7: The TOF timing at TAC3.

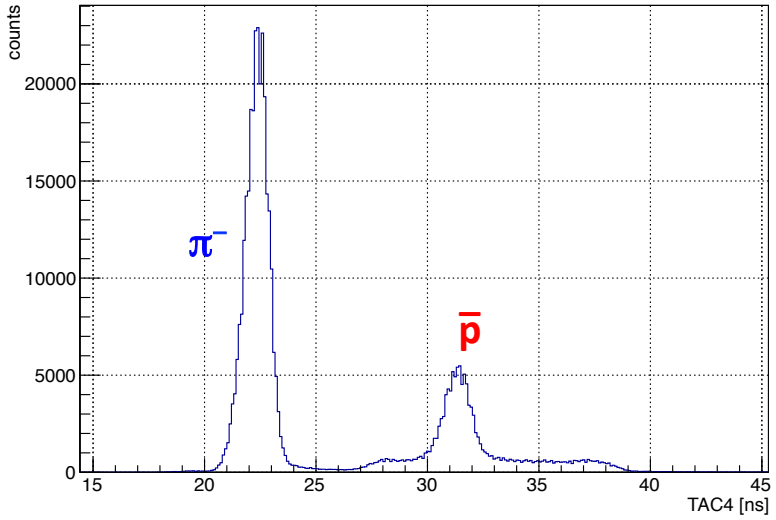

Figure 6.8: The TOF timing at TAC4.

6.4.3 Scintillation Counter

The scintillation counters, S1-S4 and P3-P5, were installed to measure the dE/dX energy loss for incoming particles. This timing allows us to identify the incoming antiprotons in the beam. The dE/dX energy loss can be estimated with the Bethe-Bloch formula, based

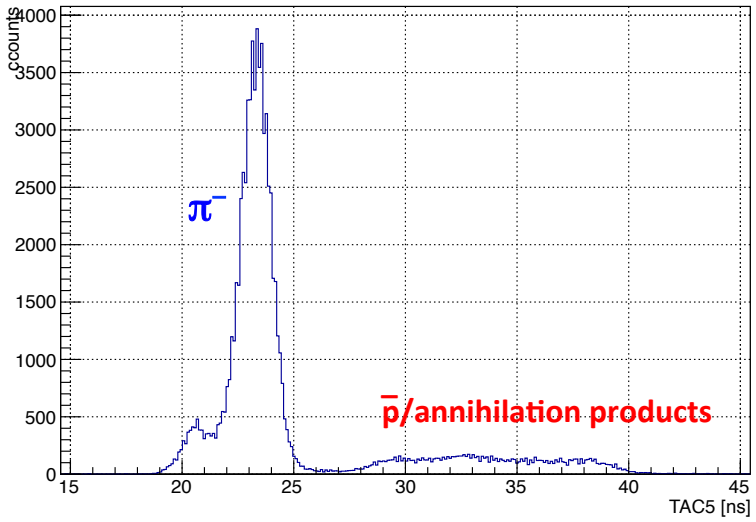

Figure 6.9: The TOF timing at TAC5.

on the charge and velocity of the incoming particle [Leo, 1987].

$$-\frac{dE}{dX} = 2\pi N_a r_b^2 mc^2 \rho \frac{Z}{A}\frac{z}{\beta^2}\left[\ln\left(\frac{2mc^2\gamma^2\beta^2 W_{max}}{I^2}\right) - 2\beta^2\right]$$

Here, N_a is Avogadro's number, r_b is the classical electron radius, m is the electron mass, c is the speed of light, ρ, Z and A are the density, atomic number and atomic weight of the absorbing material, z is the charge of the incident particle in units of e, $\beta = v/c$, $\gamma = 1/\sqrt{1-\beta^2}$, W_{max} is the maximum energy transfer in a single collision, and I is the mean excitation potential of the atom.

Since the pions in the beam were relativistic ($\beta \sim 0.99$), the dE/dX energy loss at each counter is $\sim$ 2 MeV/(g/cm^2) as seen in Eq (6.1), while antiprotons were non-relativistic ($\beta \sim 0.7$) and able to deposit more energy, proportional to $1/\beta^2$. Note that the pions produced by the antiproton annihilation in flight are also relativistic (see Chapter 8) and the dE/dX loss can be estimated as $\sim$ 2 MeV/(g/cm^2). The difference of the dE/dX energy loss between pions and antiprotons can be seen in each scintillation counter. Figure 6.10 shows the energy deposit by the dE/dX energy loss at the S1 counter. There are two peaks in the figure, at 1 MeV for pions and at 2.5 MeV for antiprotons, as expected. Here the energy was calibrated based on the GEANT4 simulation result (see Section 7.5), since the

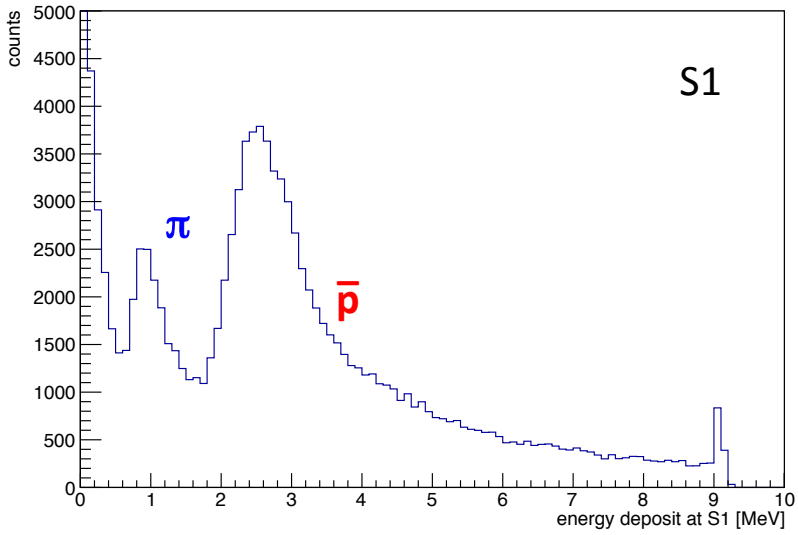

Figure 6.10: Energy deposit in the S1 counter. The peak for pions was around 1 MeV, while the peak for antiprotons was around 2.5 MeV.

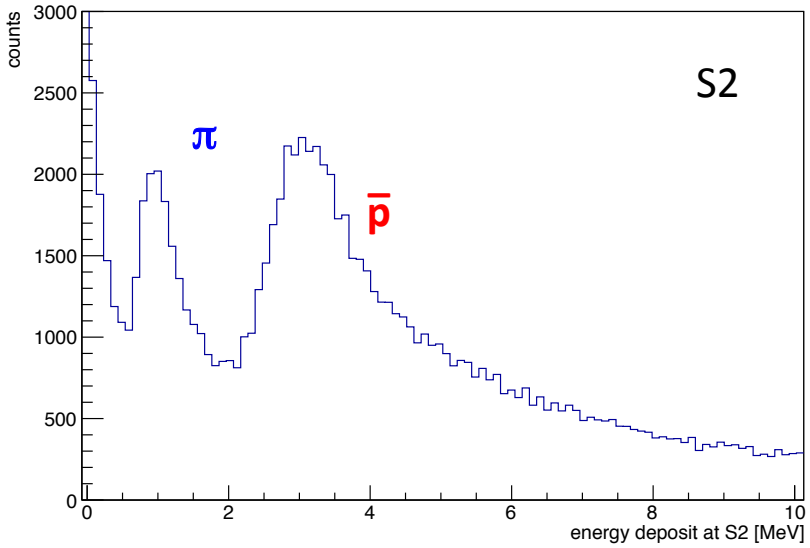

Figure 6.11: Energy deposit in the S2 counter. The peak for pions was around 1 MeV, while the peak for antiprotons was around 3.0 MeV.

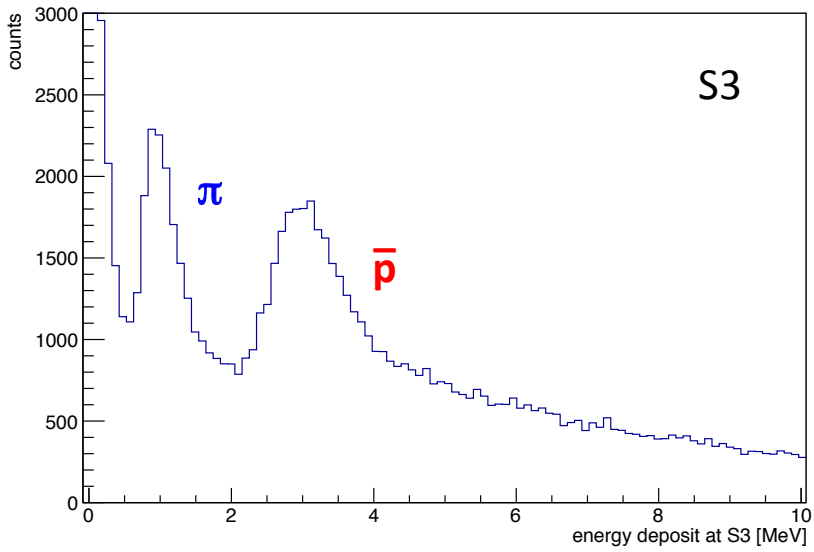

Figure 6.12: Energy deposit in the S3 counter. The peak for pions was around 1 MeV, while the peak for antiprotons was around 3.0 MeV.

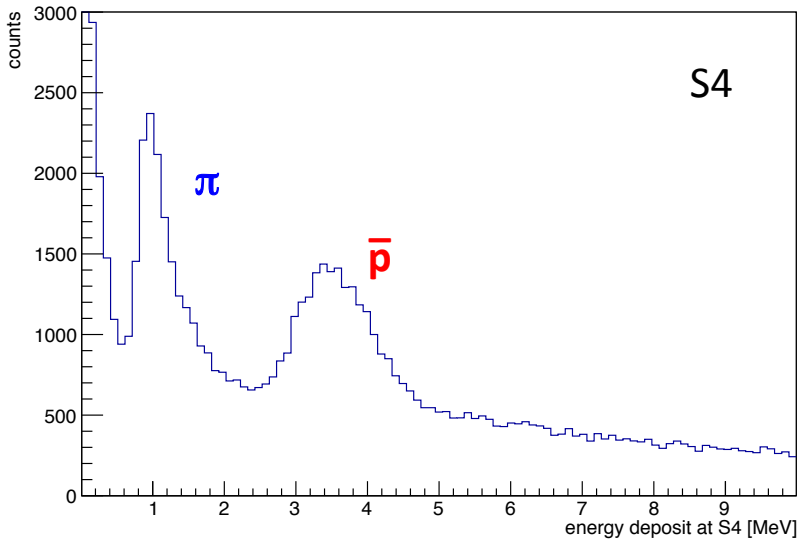

Figure 6.13: Energy deposit in the S4 counter. The peak for pions was around 1 MeV, while the peak for antiprotons was around 3.5 MeV.

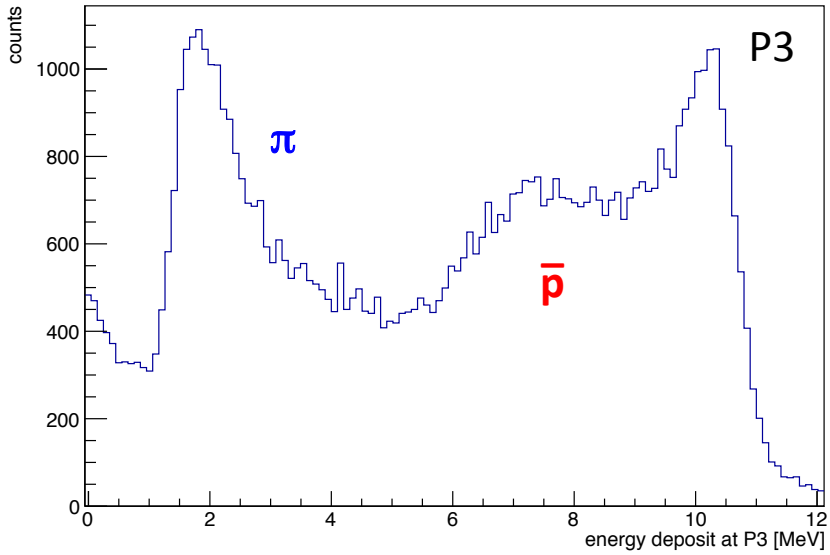

Figure 6.14: Energy deposit in the P3 counter. The peak for pions was around 1.8 MeV, while the peak for antiprotons was around 7.2 MeV. The data above $\sim$ 10 MeV was saturated.

GEANT4 simulation takes into account all the physics processes and interactions including the Bethe-Bloch dE/dX energy loss. Figures 6.11, 6.12, 6.13, 6.14 and 6.15 also show the dE/dX timing (energy deposit) in the other counters. Note that saturation of the data is seen in the P3 and the P4 counters. However, this is mainly for the antiproton annihilation events and can be eliminated with proper cuts on the TOF timing and dE/dX energy loss described in Section 7.6.2.

6.5 GEANT4 Simulation

The GEANT4 simulation was used to determine the beam trajectory and the interactions of the atomic X-rays with the target and other materials. The GEANT4 software for the simulation has been developed by CERN (the European organization for nuclear research), and it is widely used for medical, accelerator and space physics studies. The simulation provides the particle trajectories taking into account all the physics processes and interactions of particles and radiation passing through matter. The exact detector geometry (see

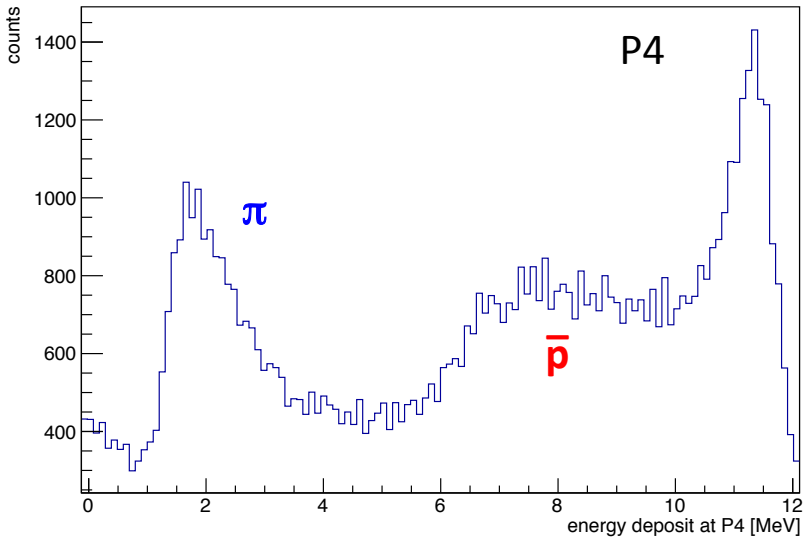

Figure 6.15: Energy deposit in the P4 counter. The peak for pions was around 1.8 MeV, while the peak for antiprotons was around 7.5 MeV. The data above $\sim$ 10 MeV was saturated.

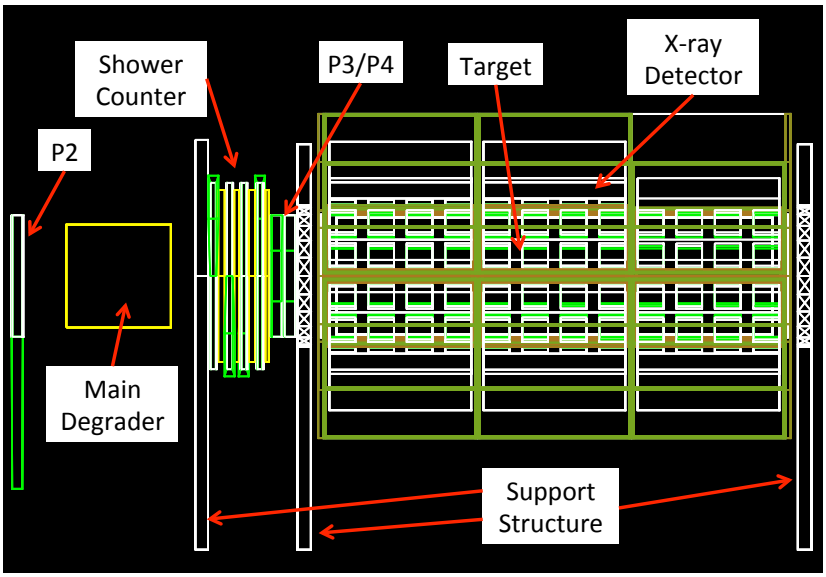

Figure 6.16: KEK detector geometry in the GEANT4 simulation.

Figure 6.16) and the beam profile measured in the experiment were used in the simulation. Approximately 10^5 antiprotons were simulated, and all the particle and X-ray trajectories, including the TOF timing and dE/dX energy deposit, were obtained in the simulation. The simulation also allows us to select the trajectory only for antiproton events, which provides more detailed TOF timing and dE/dX energy deposit to determine the antiproton selection cuts for the experimental data.

6.5.1 TOF timing

The GEANT4 simulation with a given beam profile demonstrated that there should be two peaks in the TOF timing, as seen in the real measurement, and also confirmed that these peaks were for pions and antiprotons. Figure 6.17 shows the TOF timings at TAC1 and TAC2, pion events on the left and antiproton events on the right. The peak for pions was at (TAC1, TAC2) = (11.2 ns, 22.5 ns), while the peak for antiprotons was at (15 ns, 30 ns), and they are widely separated from each other. Since the simulation focused on obtaining the TOF timing for pions and protons in order to adjust the TOF timing in the experiment, the detector response, including the noise in the electronics, and the accidental events from the pions and the antiprotons annihilated in flight were ignored in the simulation. Therefore, the simulation results had much less spread compared to the actual experiment. The simulation results for each TOF timing datum were used to adjust the timing offsets in the real experiment.

6.5.2 dE/dX energy loss

As discussed above, the GEANT4 simulation takes into account all the physics processes and interactions, including the Bethe-Bloch dE/dX energy loss in the particle trajectory. Therefore, the simulation results were used to calibrate the energy deposit in each scintillation counter. Furthermore, since GEANT4 can select the trajectory for a specific event, we can also obtain the dE/dX energy deposit for an antiproton, which stopped in the target at each counter.

Figure 6.18 shows the energy deposit in the S1 counter in the GEANT4 simulation. Two peaks, pions on the left and antiprotons on the right, are seen in the graph as expected.

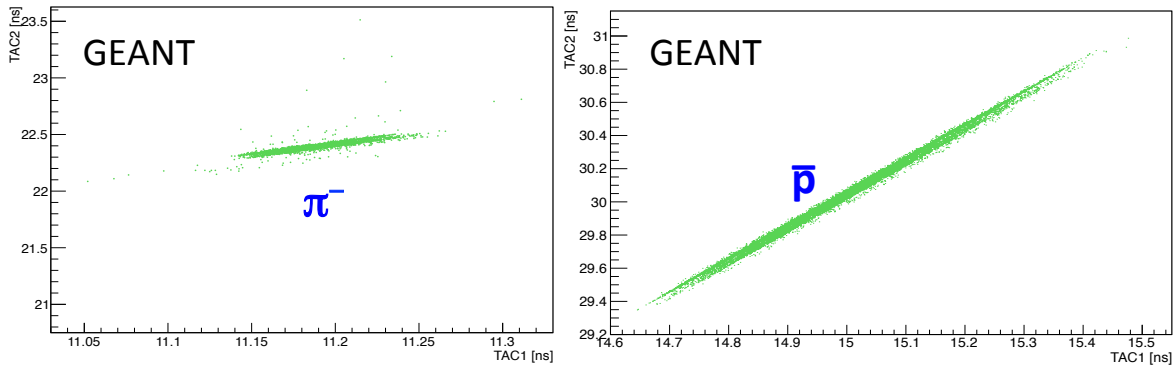

Figure 6.17: TOF timing at TAC1 and TAC2 for pions and antiprotons in the GEANT4 simulation.

Here simple antiproton selection cuts were applied on the TOF timing at TAC1 and TAC2 ($\pm$ 1 ns around the antiproton peak). The red solid line represents the energy deposit for the selected antiprotons, which stopped in the target.

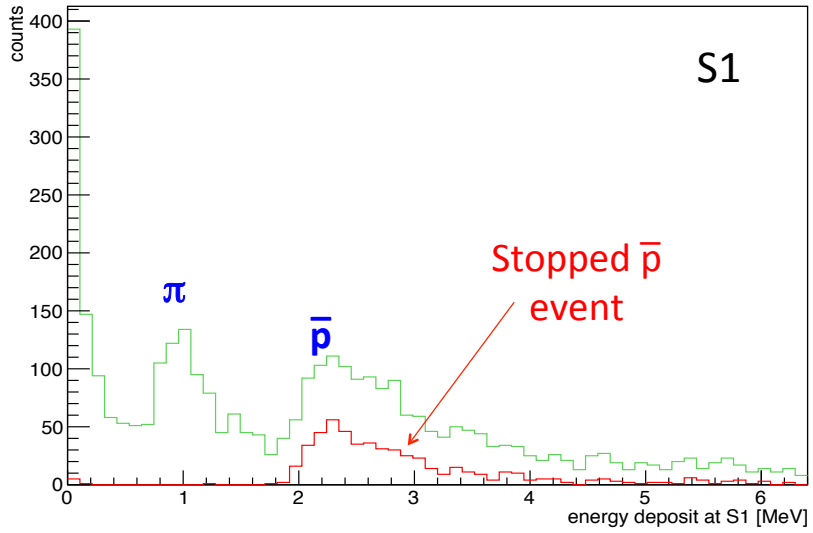

Figure 6.18: Energy deposit in the S1 counter in the GEANT4 simulation. The red solid line represents the energy deposit from those antiprotons which eventually stopped in the target

As with the TOF timing, the energy deposit in each scintillation counter allows us to identify antiprotons from pions. Moreover, the simulation results for the selected antiproton events allow us to determine the optimized cuts to distinguish antiprotons from other particles using the dE/dX energy deposit in each counter for the measurement.

6.5.3 Antiprotonic atomic X-rays

The GEANT4 simulation was conducted to understand the interaction of the atomic X-rays with the target and other materials and to obtain the amount of energy deposited in the NaI(Tl) detector. The energy of the atomic X-ray is determined based on in what material the antiproton formed the exotic atom, which can be provided by the GEANT4 simulation with the given beam profile discussed above. Antiprotons can stop in the target, NaI crystal, NaI housing including the Al window/frame and Fe frame, PMTs in the NaI housing, and plastic counter. However, we will focus on the antiprotonic X-rays generated in the target material and Al window/frame, since the probability for antiprotons to stop in the other materials are negligible, according to the GEANT4 simulation.

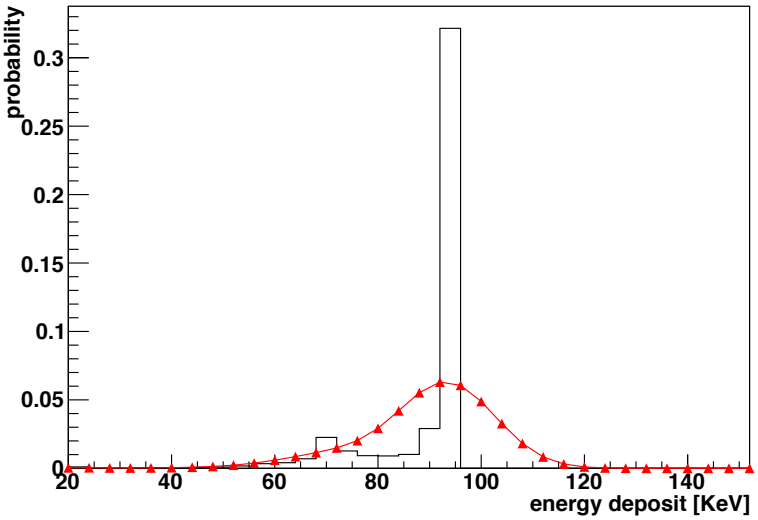

Figure 6.19: The simulation result for the energy deposit in the NaI(Tl) detector by the antiprotonic 92 keV X-ray with the Al target. The red solid line indicates the result with the detector response, 7% FWHM energy resolution at 1 MeV.

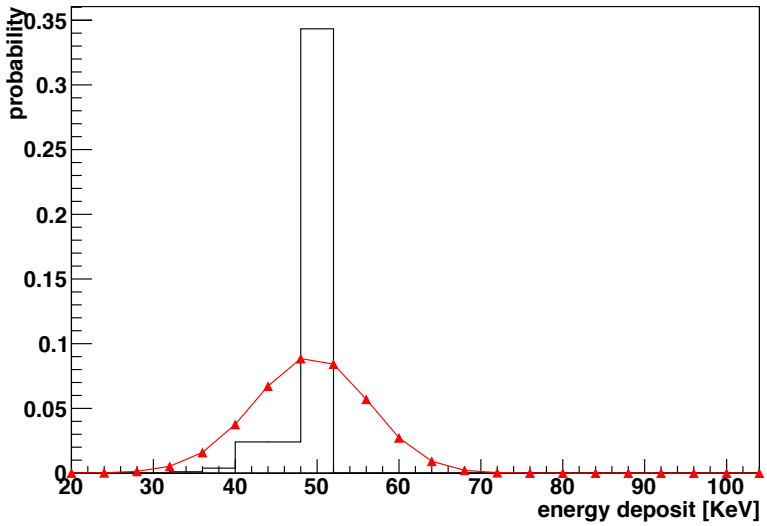

Figure 6.20: The simulation result for the energy deposit in the NaI(Tl) detector by the antiprotonic 50 keV X-ray with the Al target. The red solid line indicates the result with the detector response.

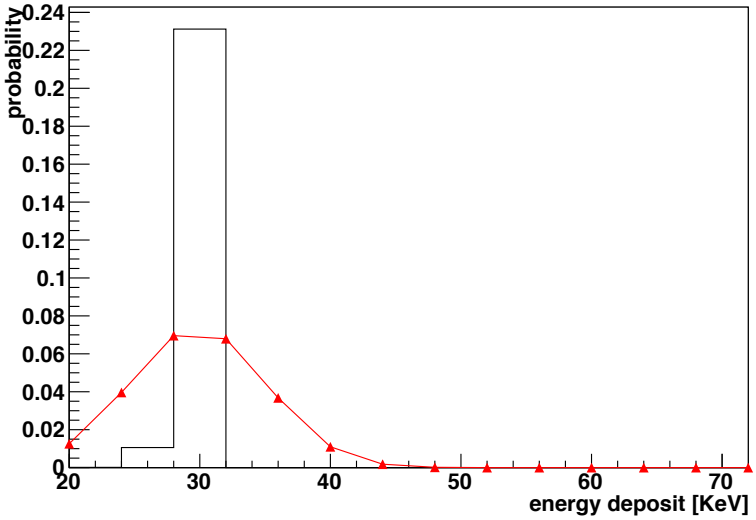

Figure 6.21: The simulation result for the energy deposit in the NaI(Tl) detector by the antiprotonic 30 keV X-ray with the Al target. The red solid line indicates the result with the detector response.

Figures 6.19, 6.20, and 6.21 show the energy deposit from the antiprotonic X-rays with the Al target. The energies of the X-ray are 92 keV ($n = 5 \rightarrow 4$ transition), 50 keV ($n = 6 \rightarrow 5$ transition), and 30 keV ($n = 7 \rightarrow 6$ transition), respectively. The black and red solid lines indicate the energy deposit in the NaI(Tl) detector with and without the detector response (7% FWHM energy resolution at 1 MeV). Figures 6.22, 6.23, 6.24, and 6.25 also show the same results with S target. These results will be used to estimate the X-ray yield as seen in Section 7.8. The energies of the atomic X-rays are 139 keV ($n = 5 \rightarrow 4$ transition), 76 keV ($n = 6 \rightarrow 5$ transition), 46 keV ($n = 7 \rightarrow 6$ transition), and 30 keV ($n = 8 \rightarrow 7$ transition).

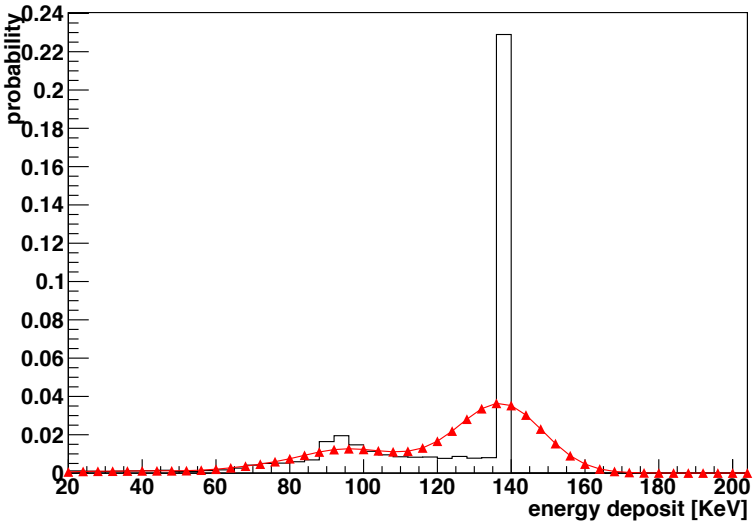

Figure 6.22: The simulation result for the energy deposit in the NaI(Tl) detector by the antiprotonic 139 keV X-ray with the S target. The red solid line indicates the result with the detector response.

6.6 Antiproton selection

As discussed above, we can identify the antiprotons in the beam by using cuts on the TOF timing and dE/dX energy deposit. The GEANT4 simulation also allows us to focus on the trajectory of the stopped antiprotons, providing more detailed dE/dX energy deposit for the antiprotons that stopped in the target. In this section, I will describe how the optimized

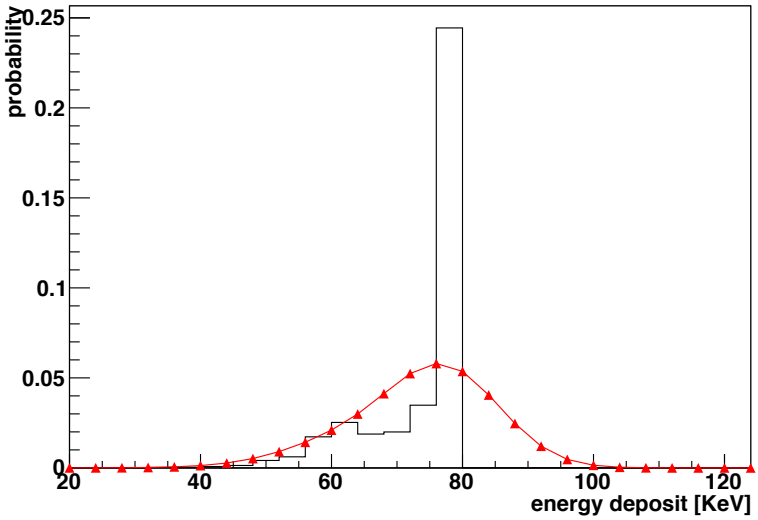

Figure 6.23: The simulation result for the energy deposit in the NaI(Tl) detector by the antiprotonic 76 keV X-ray with the S target. The red solid line indicates the result with the detector response.

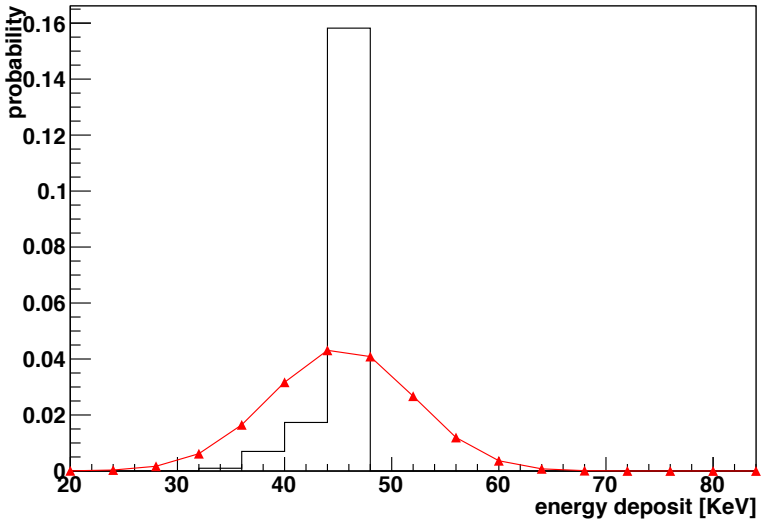

Figure 6.24: The simulation result for the energy deposit in the NaI(Tl) detector by the antiprotonic 46 keV X-ray with the S target. The red solid line indicates the result with the detector response.

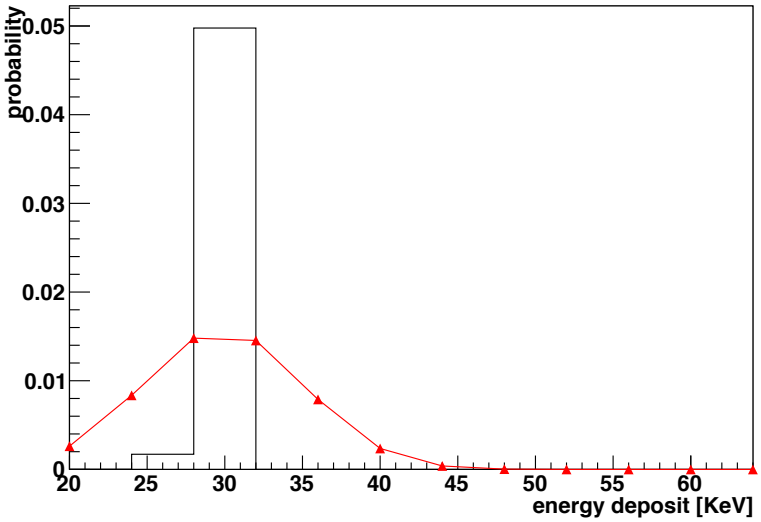

Figure 6.25: The simulation result for the energy deposit in the NaI(Tl) detector by the antiprotonic 30 keV X-ray with the S target. The red solid line indicates the result with the detector response.

antiproton selection cuts were obtained for the estimation of the antiprotonic X-ray yields described in Chapter 4.

6.6.1 Cuts on the TOF timing

As seen in Figures 6.4, 6.5, 6.6, 6.7, 6.8, and 6.9, the peaks for antiprotons and pions are clearly distinguishable. The standard deviations for the antiproton events are obtained by Gaussian fitting as shown in Figure 6.26. Based on this result, we set the antiproton selection cuts as $\pm$ 1 ns ($\sim$ 1.6 σ, $\sim$ 90% acceptance) around the peak for the antiproton events. The peaks for the TOF timing are 15 ns for TAC1, 30 ns for TAC2, 31.5 ns for TAC3 and 31.5 ns for TAC4. For the antiproton stopped events, the relativistic annihilation products may be able to hit the P5 counter at least 2 ns after the antiproton hit the P4 counter (the distance between the P4 and P5 counter is $\sim$ 60 cm). Therefore, the antiproton selection cut on TAC5 is set to $>$ 32.5 ns (TAC4 lower limit + 2 ns) or no hit on the P5 counter. The cuts on the TOF timing are shown in Table 6.1.

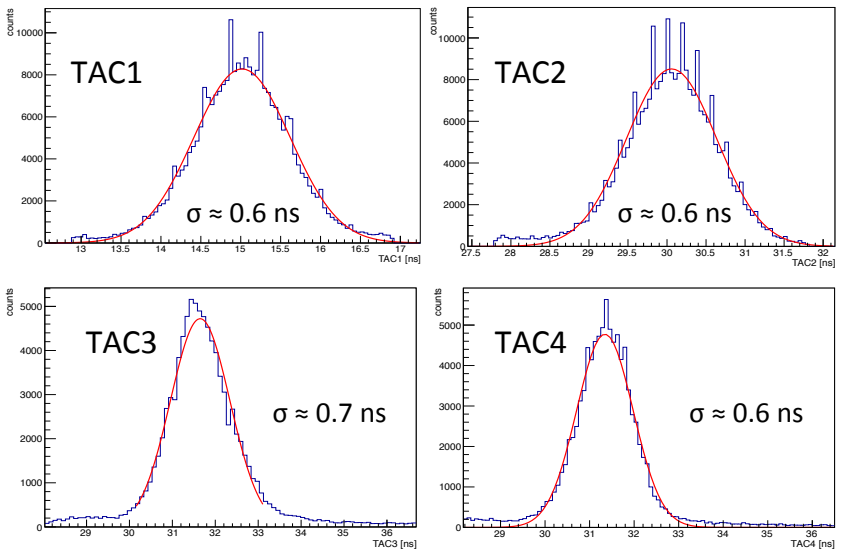

Figure 6.26: Gaussian fits to the antiproton TOF timing spread.

	lower limit	upper limit
TAC1	14.0 ns	16.0 ns
TAC2	29.0 ns	31.0 ns
TAC3	30.5 ns	32.5 ns
TAC4	30.5 ns	32.5 ns
TAC5	$>$ 32.5 ns or no hits	

Table 6.1: Antiproton selection cuts on each TOF timing

6.6.2 Cuts on the dE/dX energy deposit

The energy deposit in the S1 counter with the antiproton selection cuts on the TOF timing is shown in Figure 6.27 (left, solid blue line), compared with the selected antiproton events (right, solid black line) and the stopped antiproton events (right, solid red line) in the GEANT4 simulation. In the experiment data, the peak at $\sim$ 1 MeV is for pions, while the peak at $\sim$ 2.5 MeV is for antiprotons. Since the antiproton energy deposit spectrum is contaminated at lower energies by relativistic pions and at higher energy contaminated by the antiproton annihilation products generated in the degrader, we set the antiproton

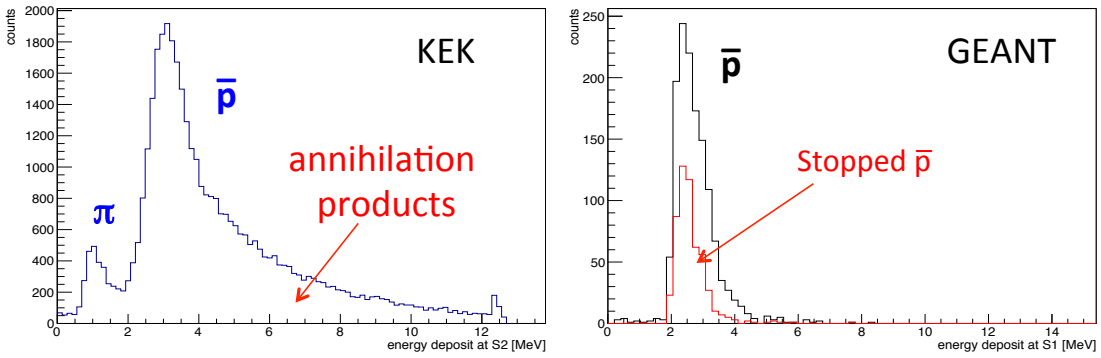

Figure 6.27: The energy deposit in the S1 counter with the antiproton selection cuts on the TOF timing, compared with the GEANT4 simulation.

selection cut as 1.8 MeV < E < 3.2 MeV. The cuts on the dE/dX energy deposit in the other counters were also determined by comparing the experimental result with the GEANT4 result and eliminating the pion and the antiproton annihilation events. Figures 6.28, 6.29, 6.30, 6.31, 6.32, and 6.33, are the graphs for the S1, S2 S3, S4, P3, and P4 counters after applying the cuts on the dE/dX energy deposit as shown in the Table 6.2.

	lower limit	upper limit
S1	1.8 MeV	3.2 MeV
S2	2.2 MeV	4.2 MeV
S3	2.2 MeV	4.2 MeV
S4	2.6 MeV	5.0 MeV
P3	8.0 MeV	-
P4	8.0 MeV	-

Table 6.2: Antiproton selection cuts on each dE/dX energy deposit

6.6.3 Contamination on the selected events

As discussed above, the TOF timing and dE/dX energy deposit allows us to identify the slow antiprotons that may stop in the target. However, since there were many materials, including the degrader on the beam axis, the antiprotons can be scattered off the beam

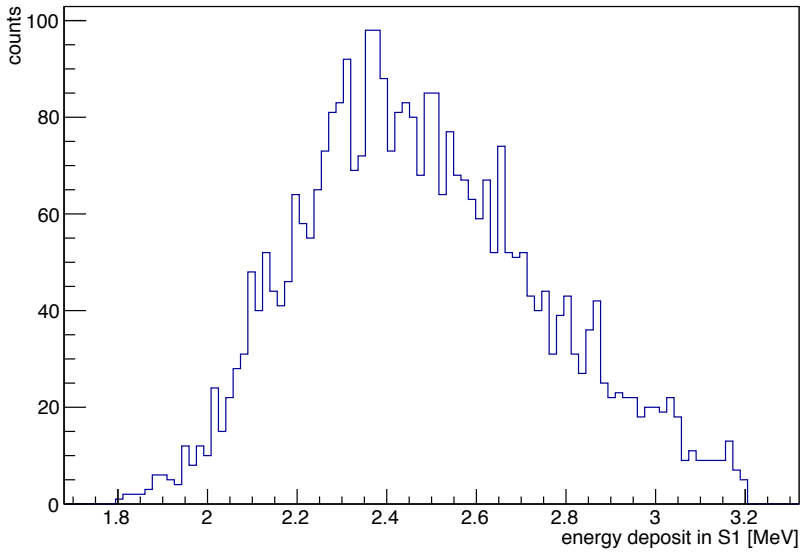

Figure 6.28: The energy deposit in the S1 counter with the antiproton selection cuts, 1.8 MeV $<$ E $<$ 3.2 MeV.

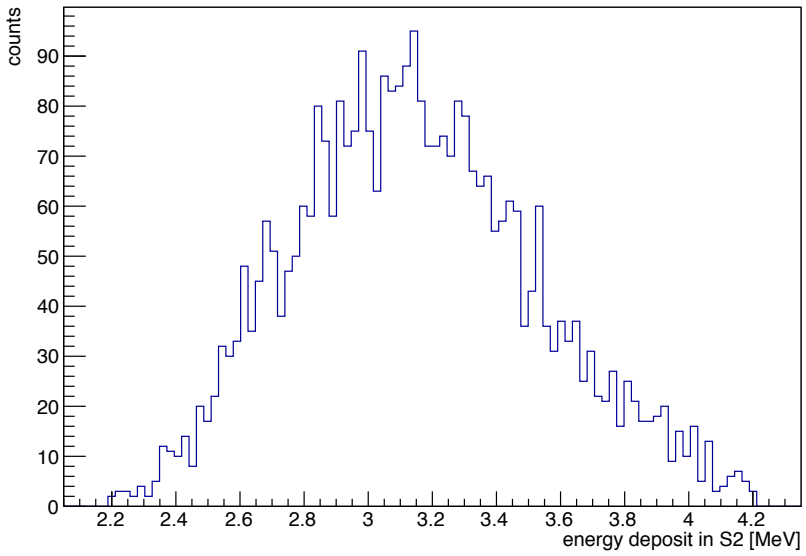

Figure 6.29: The energy deposit in the S2 counter with the antiproton selection cuts, 2.2 MeV $<$ E $<$ 4.2 MeV.

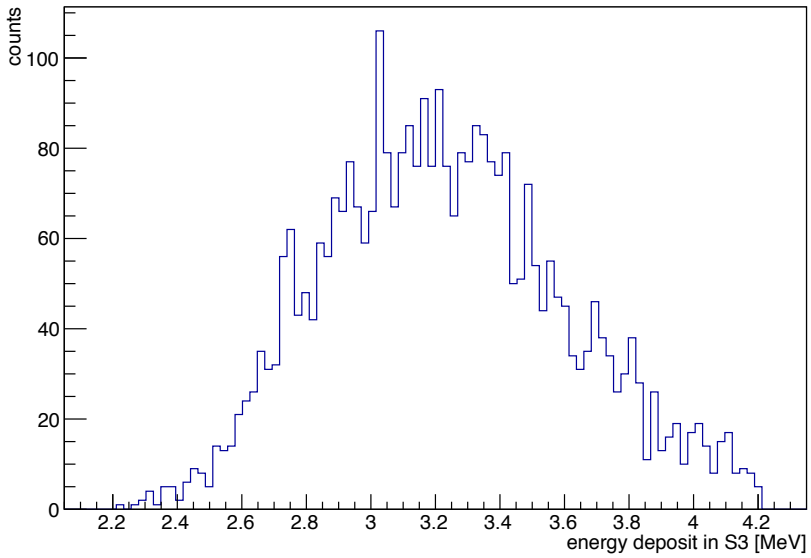

Figure 6.30: The energy deposit in the S3 counter with the antiproton selection cuts, 2.2 MeV $<$ E $<$ 4.2 MeV.

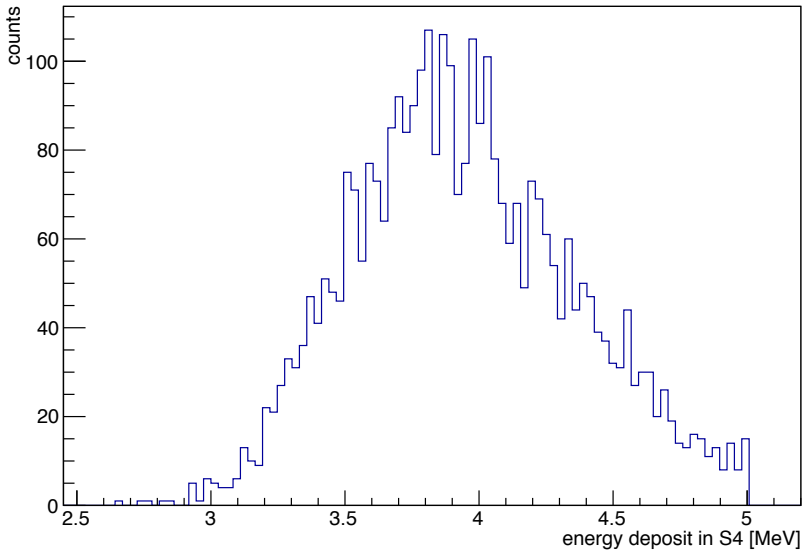

Figure 6.31: The energy deposit in the S4 counter with the antiproton selection cuts, 2.6 MeV $<$ E $<$ 5.0 MeV.

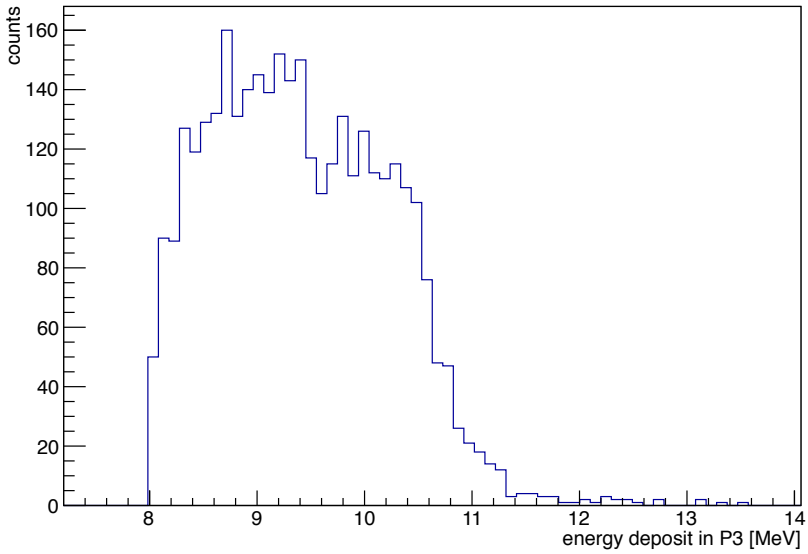

Figure 6.32: The energy deposit in the P3 counter with the antiproton selection cuts, 6.0 MeV $<$ E $<$ 8.0 MeV.

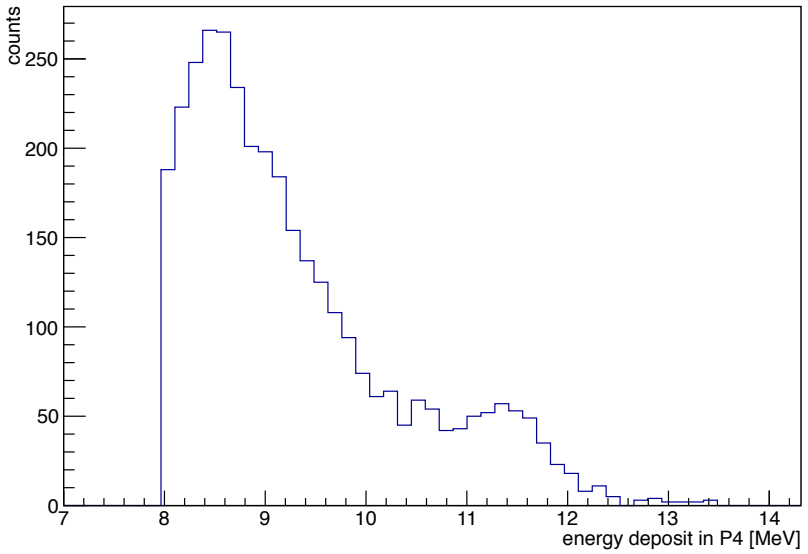

Figure 6.33: The energy deposit in the P4 counter with the antiproton selection cuts, 6.0 MeV $<$ E $<$ 8.0 MeV.

axis and may stop in other materials. The GEANT4 simulation was used to understand where between the P4 and P5 counters the antiproton stopped, and also in what material it formed the exotic atom. The simulations indicate that 86% of the antiprotons selected by the cuts on the TOF timing and dE/dX energy deposit will stop in the instrument. Moreover, $\sim$ 21% of antiprotons stopped in the target and $\sim$ 16% in the Al window and frame for the Al target, while it was $\sim$ 14% and $\sim$ 26% for the S target. Since the number of accepted events with the cuts were 2781 (7529) for the Al (S) target, 590 (1057) events were considered to stop in the target and 455 (1992) events stopped in the Al window and frame (see Table 6.3).

	total	target	Al window/frame
Al target	2781	590	455
S target	7529	1057	1992

Table 6.3: The number of antiprotons stopped in the target and Al window/frame for the Al and S target.

6.7 Background Model

Since "GAPS Allow", the time window to accept the signals measured in the X-ray detector, was programmed as 500 μs (see Section 7), the coincidence between valid triggered event and environmental background such as cosmic ray muons is negligible. Moreover, the cuts on the TOF timing exclude $>$ 99.99% of pions in the original beam according to the GEANT4 simulation. Therefore, the main background in this experiment is due to the annihilation products (mainly pions) that interact with the matter and develop an electromagnetic shower.

Two different background models were built to understand the spectrum in the X-ray detector. One is obtained from the experimental data and the other is from the GEANT4 simulation. The experimental data with cuts only on the TOF timing at TAC1 and TAC2 provides the background model, since the events with the antiproton annihilation products cannot be excluded with the cuts and dominate the result. The result is shown in Figure

6.34. Another background model can be obtained by simulating the stopped antiprotons in the target with GEANT4. The result is shown in Figure 6.35. The black solid line is the simulation result and the red solid line is the result with the detector response (7% at 1 MeV), as discussed above. Both models show the similar shape of the background

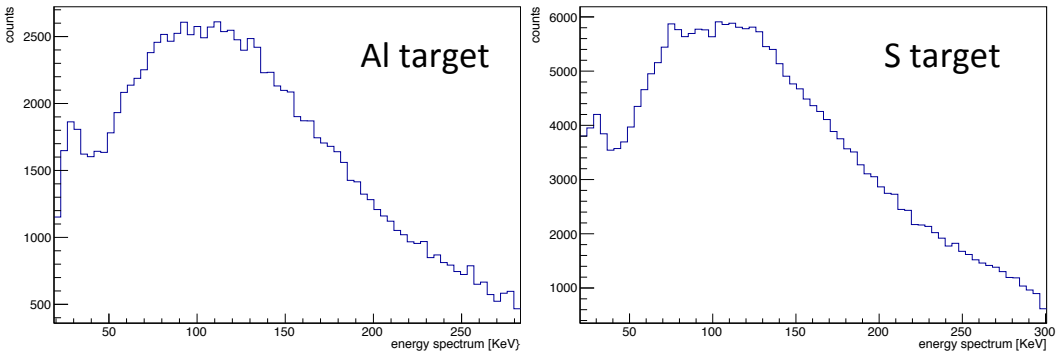

Figure 6.34: The background model for the Al (left) and S (right) targets, obtained from the experimental data. The cuts on the TOF timing at TAC1 and TAC2 were applied.

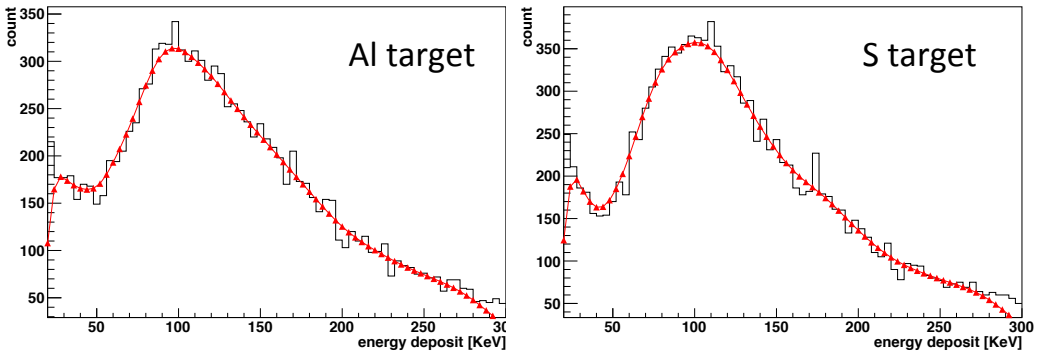

Figure 6.35: The background model for the Al (left) and S (right) targets, obtained from the GEANT4 simulation. The stopped antiprotons were demonstrated in the simulation.

and there is a wide peak around 100 keV. The S target has a more flat peak than the Al target in both models, due to the difference of the detector geometry between the Al and S targets. The model for the experimental data shows a more flat peak than the one for the GEANT4 simulation. This is because the GEANT4 model focused on the stopped

antiprotons between P4 and P5 counters, while the experimental model was mainly for the antiprotons annihilated in flight, especially in the degrader. On the other hand, the GEANT4 simulation was not able to include the very details of the detector geometry and the physics processes. Therefore, we will use both models to estimate the X-ray yield in the following section.

6.8 Calculation of the X-ray Yield

The absolute yield for each antiprotonic X-ray was estimated by fitting the data with the background model and the expected energy spectrum from each atomic X-ray as discussed in Section 7.5. The number of antiprotonic X-rays was estimated based on the fitting result, and the absolute yield for each atomic X-ray was obtained from the ratio of the number of the antiprotonic X-rays to the number of the stopped antiproton events.

6.8.1 Al target

Figure 6.36 shows the energy spectrum in the X-ray detector with cuts on the TOF timing and dE/dX energy deposit discussed above. Three peaks for the antiprotonic X-rays, around 30 keV, 50 keV, and 92 keV, can be seen in the graph.

Figures 6.37 and 6.38 show the fitting results for two different background models as discussed above. The solid black line is the experimental data, the green dashed line is the sum of the background (blue dashed line) and the three atomic X-ray lines (red dashed lines). From this fitting, the absolute yields for the atomic X-rays were obtained as 87% $\pm$ 16% for 30 keV, 79% $\pm$ 15% for 50 keV, 86% $\pm$ 16% for 92 keV, by taking the average of these two background models. Here, the error was estimated based on the statistical error shown in the graph and the systematic error due to the uncertainty in the detector calibration ($\sim$ 7%), the background model ($\sim$ 4%), and the GEANT4 simulation results ($\sim$ 10%). The absolute yields for these three X-rays are within the 1-σ error. The yield for the 30 keV X-ray is slightly higher, but this could be due to the contribution by the antiprotonic X-rays from other materials around the target. The nuclear absorption effects were not seen in the $n = 5 \rightarrow 4$ transition.

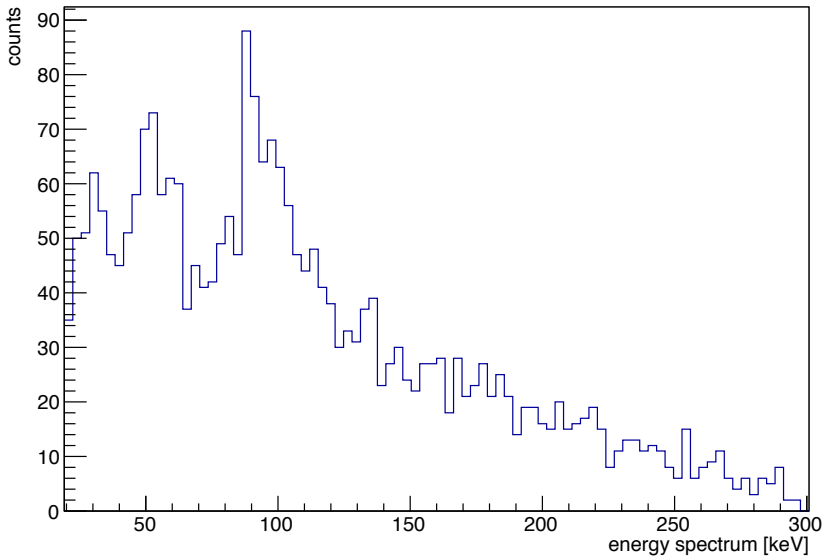

Figure 6.36: The energy spectrum for the Al target with the cuts on the TOF timing and dE/dX energy deposit.

6.8.2 S target

Since some of the antiprotons may stop in the Al window/frame, the data needs to be fitted with seven X-rays (three from the Al target and four from the S target) in the small energy region. Therefore, to simplify the fitting, we assumed that the 30 keV ($n = 8 \rightarrow 7$), 46 keV ($n = 7 \rightarrow 6$) and 76 keV ($n = 6 \rightarrow 5$) X-rays have the same X-ray yields as seen for the Al target. Additionally, the absolute yields for the Al target obtained above were used for the antiproton stopped in the Al window/frame in order to estimate the absolute yields for the S target.

Figures 6.40 and 6.41 show the fitted result for two different background models as discussed above. From this fitting, we obtained the absolute yields for the atomic X-rays as 77% ± 21% for 30 keV, 77% ± 21% for 46 keV, 77% ± 21% for 76 keV and 41% ± 31% for 139 keV. We see the nuclear absorption at $n = 5 \rightarrow 4$ transition in both background models, and this is consistent with the result shown in [Kunselman and Seki, 1973].

In summary, we saw high X-ray yields, $> 70\%$, in all the transitions except for the $n = 5 \rightarrow 4$ transition of the S target, which is due to the nuclear capture as expected.

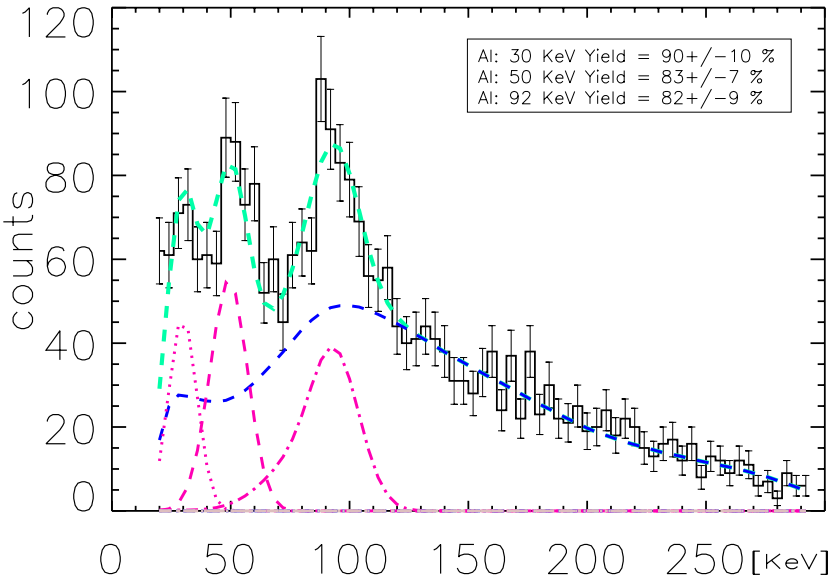

Figure 6.37: The data for the Al target fitted with the GEANT4 background model (blue dashed line) and the expected X-ray spectrum for each antiprotonic X-ray (red dashed lines).

Therefore, we also expect high absolute yields for the three highest X-rays with the Si target that will be used in the GAPS balloon experiment, since Si is $Z = 14$, between Al ($Z = 13$) and S ($Z = 16$) in the periodic table of elements. The result was also used to evaluate the parameters, α, W, and Γ_{ref}, in the cascade model as seen in Chapter 4.

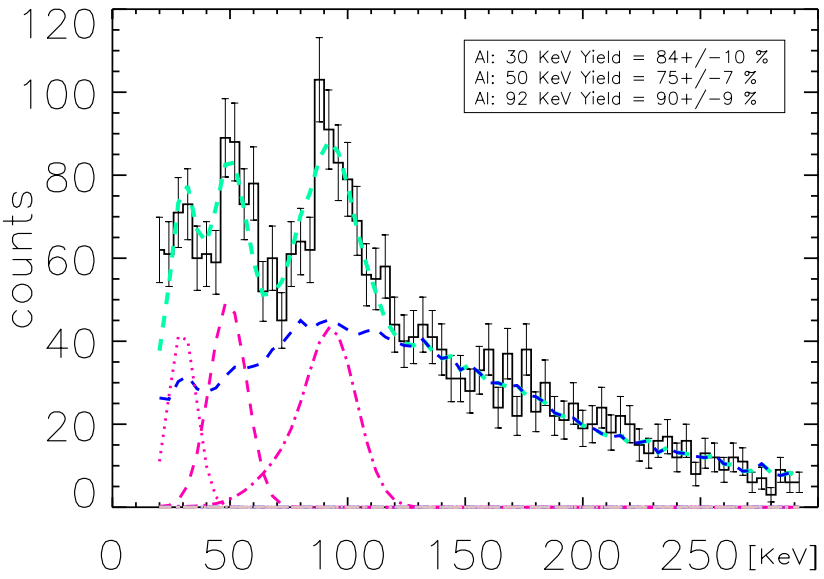

Figure 6.38: The data for the Al target fitted with the background model obtained from the experimental data (blue dashed line) and the expected X-ray spectrum for each antiprotonic X-ray (red dashed lines).

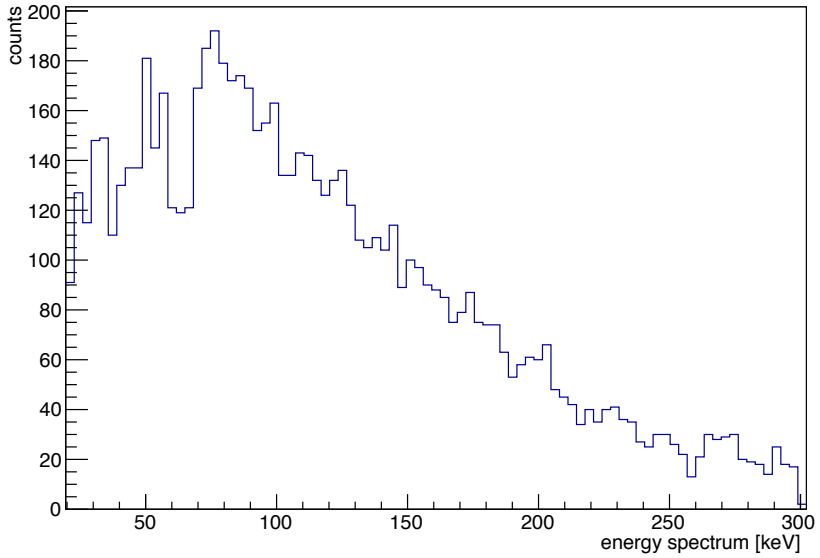

Figure 6.39: The energy spectrum for the S target with the cuts on the TOF timing and dE/dX energy deposit.

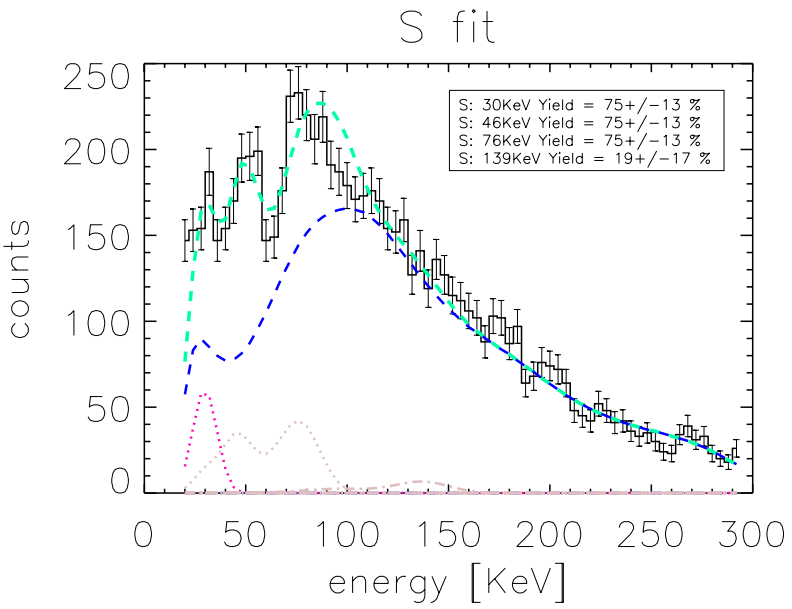

Figure 6.40: The data for the S target fitted with the GEANT4 background model (blue dashed line) and the expected X-ray spectrum for each antiprotonic X-ray (red dashed lines).

target	Transition	Energy	Yield	Error
Al	$7 \rightarrow 6$	30 keV	87%	14%
	$6 \rightarrow 5$	50 keV	79%	13%
	$5 \rightarrow 4$	92 keV	86%	14%
S	$8 \rightarrow 7$	30 keV	77%	21%
	$7 \rightarrow 6$	46 keV	77%	21%
	$6 \rightarrow 5$	76 keV	77%	21%
	$5 \rightarrow 4$	139 keV	41%	31%

Table 6.4: X-ray yields for the antiprotonic exotic atom with the Al and S targets

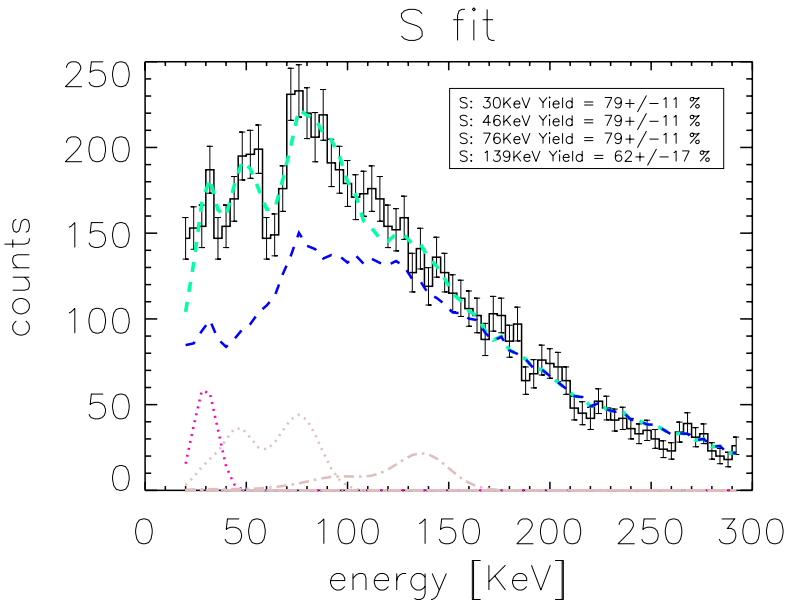

Figure 6.41: The data for the S target fitted with the background model obtained from the experimental data (blue dashed line) and the expected X-ray spectrum for each antiprotonic X-ray (red dashed lines).

Chapter 7

GAPS Sensitivity Calculation

The original GAPS concept established by Mori and Hailey [Mori *et al.*, 2002] was designed to identify incoming particle with atomic X-rays of the exotic atom. In consideration of many types of backgrounds in the GAPS balloon experiment, the current concept, as discussed in the previous chapter, has been introduced with additional particle identification methods, such as the depth sensing/stopping range and dE/dX energy deposit of the incoming particle, and the particle multiplicity in the decay of the exotic atom.

This chapter includes a discussion of how the GAPS antideuteron sensitivity was calculated with a custom Monte Carlo simulation using GEANT4, in addition to, how the antideuterons can be identified with the current detection concept. The calculation includes basic introduction to common methodology and definitions, such as GRASP and sensitivity, and then a detailed development of the nuclear physics behind the use of particle multiplicity for background rejection and the use of depth sensing for particle rejection. Finally, this is all put together along with the X-ray yields measured in the previous chapter to determine the detailed sensitivity of GAPS for detecting antideuterons. The result indicates the GAPS sensitivity will be two orders of magnitude better than the current upper limit for the antideuteron flux by the BESS experiment [Fuke *et al.*, 2005], and comparable to the 5 year AMS-02 observation (see Section 7.7), which proves GAPS is an ideal approach for an antideuteron search.

7.1 Overview of the Simulations

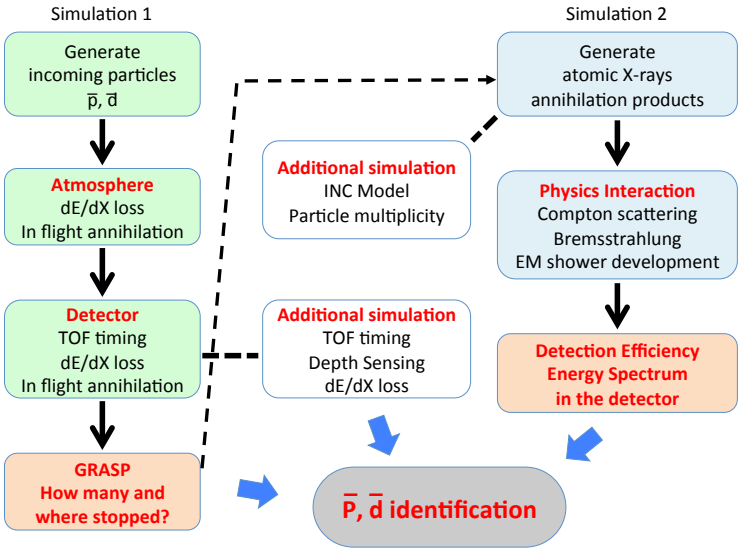

Figure 7.1: Flow chart for the simulation.

The GEANT4 simulation was conducted to study the background rejection in the GAPS experiment. The major background in the experiment is antiprotons, since their flux is $\sim 10^4$ times more than that of antideuterons, and furthermore, they can form an exotic atom that can decay and emit atomic X-rays and annihilation products (pions and protons). Therefore, the simulation was conducted to evaluate the performance of the antideuteron and antiproton identification. The simulation was divided into two parts: The first simulation was to obtain how many antideuterons can stop in the target and form exotic atoms, including the energy loss and in-flight annihilation in the atmosphere. The second simulation estimated the energy spectrum in the detector due to the decay of the antideuteronic and antiprotonic exotic atoms, including all the interactions with the instruments, such as Compton scattering and Bremsstrahlung, that develop the electromagnetic shower. Additional simulation was conducted for the TOF timing, depth sensing and dE/dX energy loss. The simulation results allow us to determine the optimized cuts to distinguish antideuterons from antiprotons. Note that the particle multiplicity due to the nuclear annihilation of the exotic atom was estimated with a simple Monte Carlo simulation, based on the Intra Nucear

Cascade (INC) Model (see Section 7.5). The brief overview of the simulations is shown in Figure 7.1.

7.2 GEANT4 Setup

In the GEANT4 simulation, the detector geometry was defined as 13 layers of Si(Li) detectors surrounded by the TOF paddles as discussed in Chapter 4. Each layer was composed of 270 Si(Li) wafers, and each wafer was 4 inch diameter, 2.5 mm thick. The TOF was a 3 mm thick plastic layer. The geometrical setup in GEANT4 is shown in Figure 7.2. The Si(Li) preamplifier and the signal cables were assumed to be uniformly distributed around the detector, and therefore modeled as a 5 mm thick Al detector frame. The atmosphere was treated as a flat, thin layer of compressed air (ρ = 1.0 g/cm^3) with the equivalent atmospheric column depth, 3.9 g/cm^2, as found at a flight altitude of 35 km. It was placed just above the instrument in the simulation. See Section 7.2 for more details.

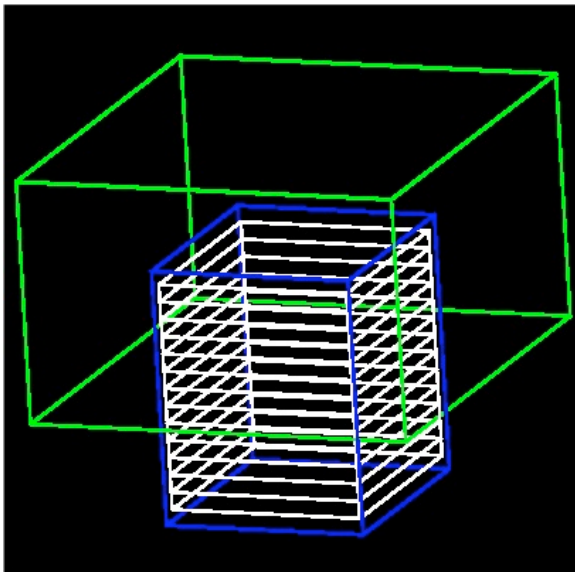

Figure 7.2: Geometrical setup in GEANT4.

Models for most of the physics processes and interactions relevant to GAPS are available in GEANT4. However, since the physics for antideuterons is still not well-known, the antideuteron has not yet been defined in GEANT4. Therefore, the sensitivity for an-

tideuteron was estimated by using the simulations for protons, deuterons, and antiprotons. In addition, the inelastic (annihilation) cross sections for low energy antiprotons are not current in GEANT4, so we modified the physics interaction code in GEANT4 based on a recent model fitted with experimental data [Duperray *et al.*, 2005]. The comparison between the original and modified GEANT4 antiproton annihilation cross section and experimental data is shown in Figure 7.3. The modified cross section agrees well with the experimental data (Carbon target) [Nakamura *et al.*, 1984; Kuzichev, 1994]. Since the original GEANT4 inelastic (annihilation) cross section was overestimated, more antiprotons can actually annihilate in flight before stopping in the target than GEANT4 originally predicted, as seen in Figure 7.4, and thus the incoming antideuteron flux was underestimated.

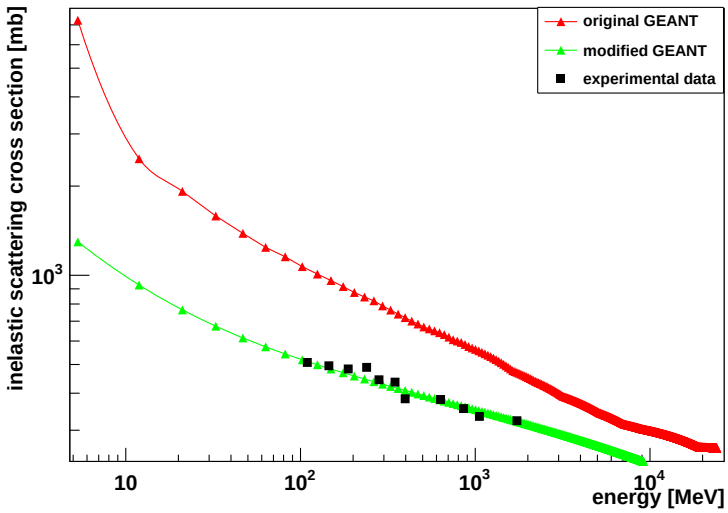

Figure 7.3: Original and modified antiproton annihilation cross section in GEANT4 and experimental data (Carbon target)

Simulation software for the cascade model of the exotic atom was not in GEANT4, and also could not be easily incorporated. Therefore, the simulation was conducted in two stages: simulations before and after the antiparticle stops in the instrument. The first simulation provided the number of incoming particles stopped in the instrument and also where they stopped. Then, the atomic X-rays and charged particles, decay products of the

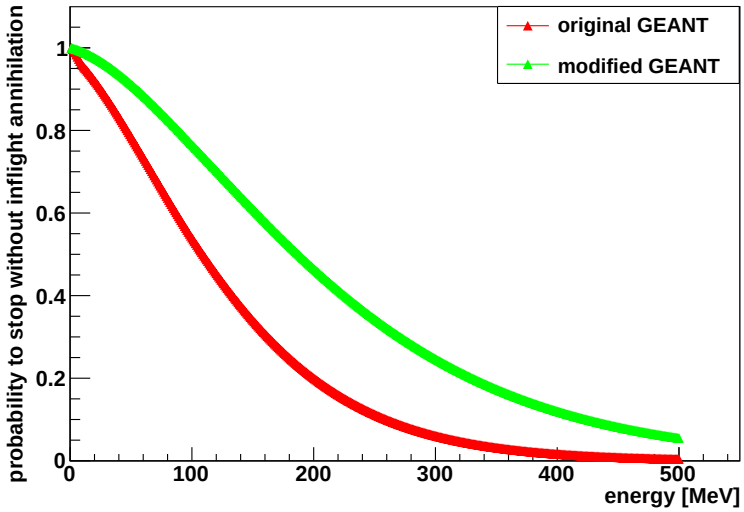

Figure 7.4: The probability for antiprotons to stop without the in flight annihilation. The original and modified annihilation cross section in GEANT4

exotic atom, were manually generated in the second simulation, based on the result of the first simulation. The second simulation provided the detection efficiency of these particles. Considering that bGAPS experiment will be conducted in the Antarctic, where almost no rigidity cutoff (particles trapped by the magnetic field) exists, the geomagnetic field in the atmosphere was ignored in the simulation to simplify the model.

7.3 GRASP

Some of the incoming antiparticles may not be able to reach the instrument since they interact with atoms in the atmosphere and annihilate in flight. In the simulation, primary particles were isotropically (downward only) generated above the atmosphere with a flat energy distribution between 0 and 250 MeV/n, based on the antideutron flux predicted from the dark matter model as discussed below. (See Figure 7.25.) They were slowed down by the atmosphere and stopped in the detector if they did not annihilate in flight. Figures 7.6, 7.7 and 7.8 show the energy and angular distribution (cosine of the zenith angle) at the top of atmosphere for the protons, antiprotons and deuterons that stopped in the instrument.

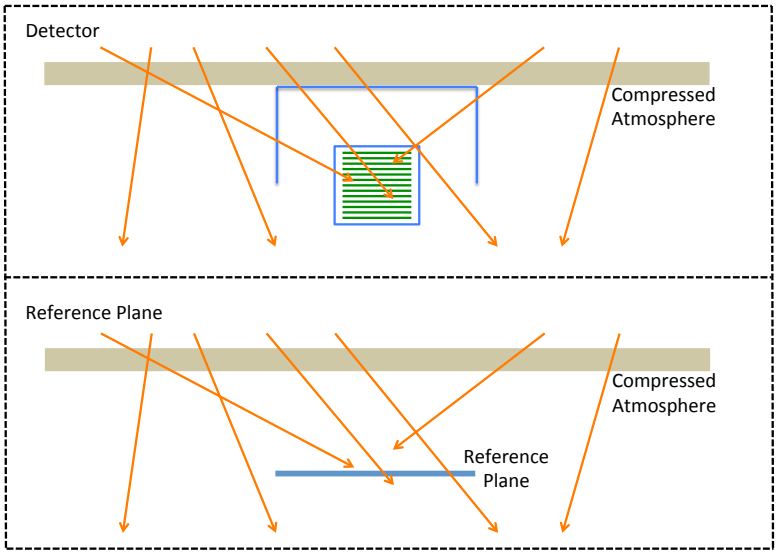

Figure 7.5: Overview of the GEANT4 setup with the GAPS detector (above) and reference plane (below).

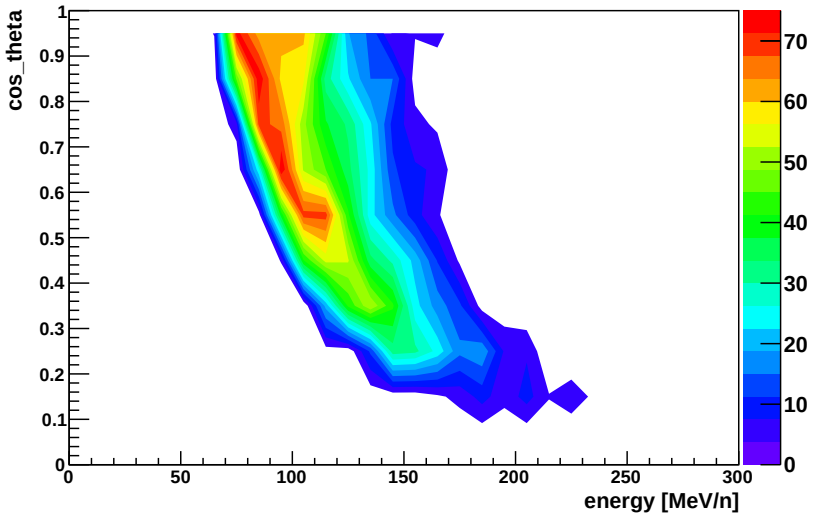

Figure 7.6: Energy and angular distribution (cosine of the zenith angle) at the top of atmosphere for protons stopped in the instrument.

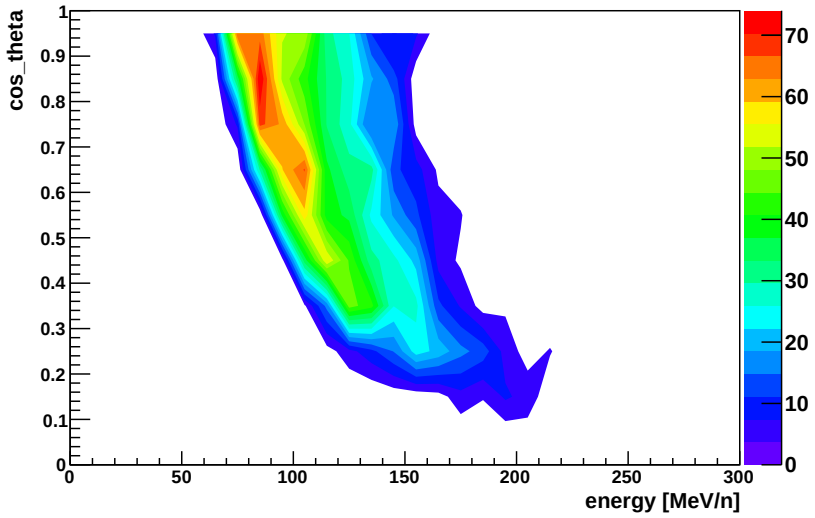

Figure 7.7: Energy and angular distribution (cosine of the zenith angle) at the top of atmosphere for antiprotons stopped in the instrument.

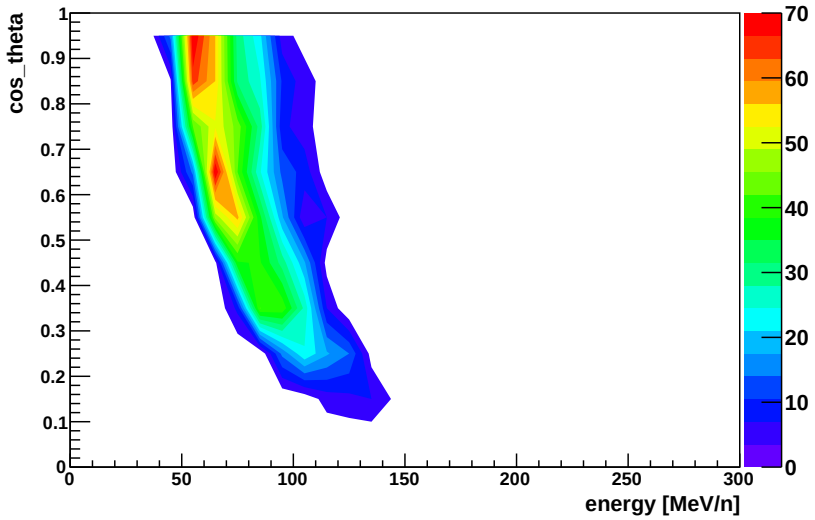

Figure 7.8: Energy and angular distribution (cosine of the zenith angle) at the top of atmosphere for deuterons stopped in the instrument.

The graphs for protons and antiprotons show similar distribution except that the number of antiprotons stopped in the instrument was less due to the in flight annihilation. The energy range for the stopped deuterons was narrow compared to protons and antiprotons as seen in the graphs. This is because the deuterons with the same velocity (same energy per nuclei) as protons and antiprotons have a longer stopping range than protons and antiprotons.

The GRASP ($m^2 \cdot Sr$), defined here as the product of the geometrical acceptance and stopping efficiency of the instrument, can be estimated by considering the geometrical acceptance of the reference plane, G_{ref}, as described in the Figure 7.5.

$$\begin{aligned} \Gamma &\equiv G_{GAPS} \cdot \epsilon_{stop} \\ &= G_{ref} \cdot \frac{N_{det}^{hit}}{N_{ref}^{hit}} \cdot \epsilon_{stop} \\ &= G_{ref} \cdot \frac{N_{det}^{stop}}{N_{ref}^{hit}} \end{aligned}$$

, where

$$\begin{aligned} G_{GAPS} &\equiv G_{ref} \cdot \frac{N_{det}^{hit}}{N_{ref}^{hit}} \\ G_{ref} &= \int_0^{2\pi} A \cos\theta d\theta = \pi A. \end{aligned}$$

Here, Γ is the GRASP, G_{GAPS} is the geometrical acceptance of the GAPS instrument, ϵ_{stop} is the stopping efficiency of the instrument, N_{det}^{hit} and N_{ref}^{hit} are the number of primary particles hitting the detector and reference plane respectively, N_{det}^{stop} is the number of primary particles stopped in the detector, and A is the area of the reference plane.

As discussed above, since the annihilation cross section of the antideuteron has not been well studied, we simply assumed that the annihilation cross section is proportional to the geometric area and the ratio of the GRASPs between the antideuteron and deuteron is similar to that between the antiproton and proton. Therefore, the GRASP for antideuterons can be estimated as follows:

$$\Gamma_{\bar{d}} \simeq \Gamma_d \cdot \frac{\Gamma_{\bar{p}}}{\Gamma_p}.$$

The GRASPs for protons, antiprotons, deuterons, and antideuterons can be found in Table 7.1. We also defined $\Gamma^{Si(Li)}$ as the GRASP for the particles stopped in the Si(Li) detector. We can also determine multiplicity depth and dE/dX for particles stopping in material other than silicon, such as frame, cables and electronics. If the actual stopping material is known, on the above information, aluminum with the atomic X-rays can be used to deduce the stopped particle.

Table 7.1: GRASPs for protons, antiprotons and deuterons ($m^2 \cdot Sr$)

	proton	antiproton	deuteron	antideuteron
Γ	3.56	2.88	1.87	1.52
$\Gamma^{Si(Li)}$	1.36	1.14	0.72	0.61
$\epsilon_{Si(Li)}$	0.38	0.40	0.39	0.40

7.4 Atomic X-ray

While the nuclear annihilation of the antiparticles in the exotic atom are included in the GEANT4 physics package, the cascade model of the exotic atom is not included. Therefore, the simulation for the exotic atom was conducted by simulating the exotic atom deexcitation as atomic X-rays and a stopped antiparticle. The stopped antiparticle was allowed to immediately decay. These particles were generated at the position where the incoming antiparticle had stopped in the previous simulation.

Figures 7.9, 7.10, and 7.11 show the spectrum in the Si(Li) detector for the antideuteronic atomic X-rays of the Si target, which have energies of 30 keV, 44 keV and 67 keV. The black solid line is the simulation result without detector response, while the red solid line includes the detector response with FWHM = 2 keV. It is normalized by the number of events (generated X-rays).

In order to minimize the background event, the acceptance cut was set as ± 1 keV around the peak for each X-ray. The detection efficiency for each atomic X-ray becomes $\epsilon_X^{30keV} = 0.16$, $\epsilon_X^{44keV} = 0.13$ and $\epsilon_X^{67keV} = 0.05$. Therefore, the probability that at least one

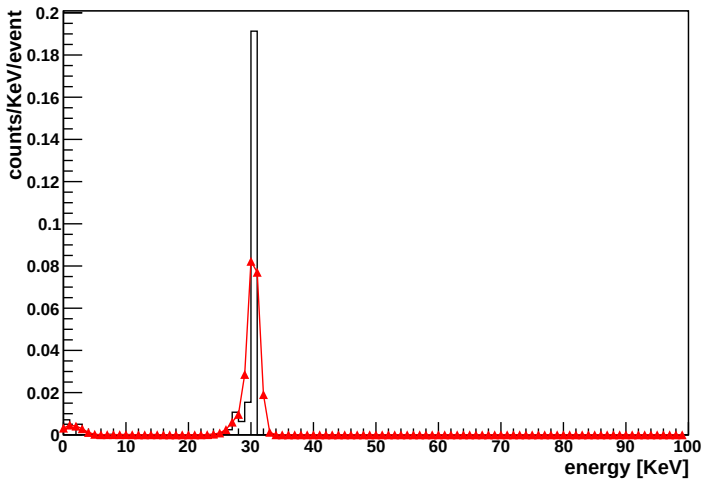

Figure 7.9: X-ray spectrum for the antideuteronic 30 keV X-ray of the Si target. The black solid line is the simulation result without detector response, while the red solid line includes the detector response with FWHM = 2 keV.

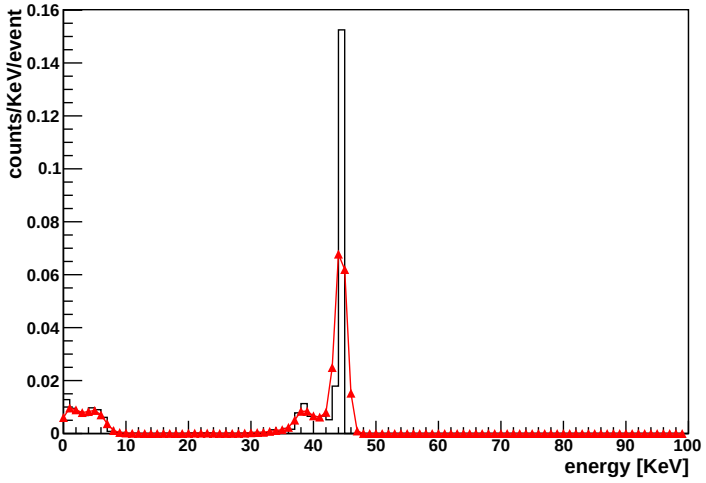

Figure 7.10: X-ray spectrum for the antideuteronic 44 keV X-ray of the Si target. The black solid line is the simulation result without detector response, while the red solid line includes the detector response with FWHM = 2 keV.

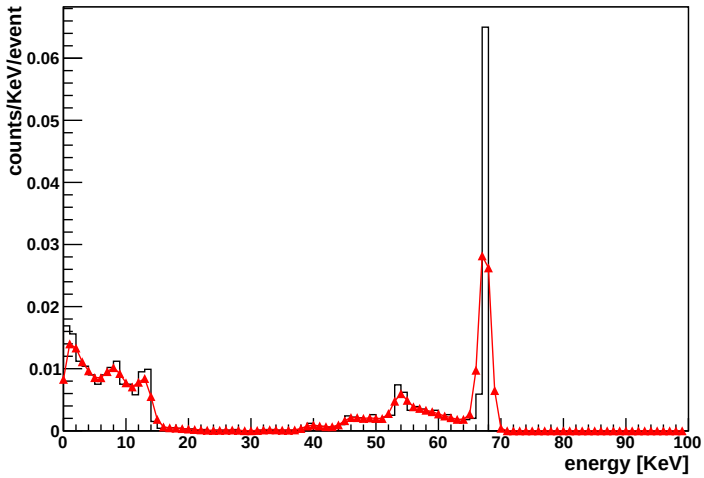

Figure 7.11: X-ray spectrum for the antideuteronic 67 keV X-ray of the Si target. The black solid line is the simulation result without detector response, while the red solid line includes the detector response with FWHM = 2 keV.

atomic X-ray can be detected, $\epsilon_X^{\bar{d}}$, is estimated as $1-(1-\epsilon_X^{30keV})\cdot(1-\epsilon_X^{44keV})\cdot(1-\epsilon_X^{67keV}) \sim 0.30$. Note that since the separation between Si(Li) layers is relatively large, 15 cm, and the Si(Li) strip is relatively small, 1-2 cm, the probability that the X-rays and annihilation products hit the same strip is negligible. Considering the X-ray yield of the exotic atom, the X-ray detection efficiency per exotic atom becomes $Y \cdot \epsilon_X$, where Y is the average absolute yield of the atomic X-rays.

Figure 7.12 shows the energy spectrum of the antiprotonic event, which is the superposition of the atomic X-rays (35 keV, 58 keV, 107 keV) and interactions of the annihilation products with the instrument. The black solid line is the simulation result without detector response, while the red solid line includes the detector response with FWHM = 2 keV. This indicates that the probabilities of the misidentification as the antideuteronic X-rays (2 keV around the peak) by the antiprotonic event, $\epsilon_X^{\bar{p}}$, are $\sim 4\%$ for 30 keV, $\sim 3\%$ for 44 keV and $\sim 2\%$ for 67 keV. Note that this might be slightly overestimated since we assumed a 100% yield for each antiprotonic X-ray. Considering the probability that the incoming particle stops in the Si(Li) detector, the antiproton rejection factor for one or more antideuteronic

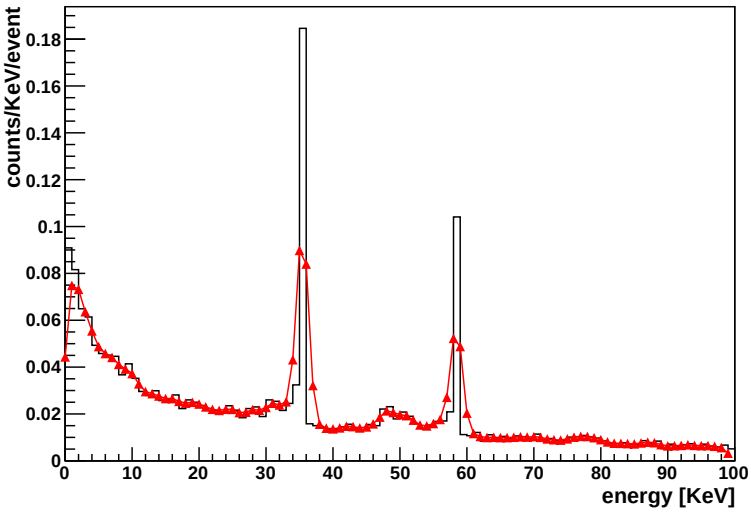

Figure 7.12: Energy spectrum for the antiproton event.

X-ray detection becomes, $r_{X\geq 1} = 1/a_X^{\bar{p}} \sim 84$. Here, $a_X^{\bar{p}}$ is the acceptance (probability) of the antiprotonic event to be misidentified as the antideuteronic X-ray and it is estimated as $a_X^{\bar{p}} = \epsilon_X^{\bar{p}} \cdot \epsilon_{Si(Li)} = 0.012$. Here, $\epsilon_{Si(Li)}$ is the probability that the incoming antiparticle can stop in the Si(Li) detector (see Section 5.2). The acceptance of antideuteronic events with one or more X-rays detected can be estimated as $a_{X\geq 1}^{\bar{d}} = \epsilon_X^{\bar{d}} \cdot \epsilon_{Si(Li)} \cdot Y = 0.10$, considering the X-ray yield, $Y \sim 0.8$.

7.5 Nuclear Annihilation Products

7.5.1 Intra Nucear Cascade (INC) Model

The interaction of antiprotons with nucleons (protons and neutrons) has been studied since the discovery of the antiproton by Chamberlain, Segre, Wiegand, and Ypsilantis in 1955. Many particles can be produced in the antiproton annihilation on nuclei, and the intra nuclear cascade (INC) model has been developed to predict the particle multiplicity [Cugnon, 1989; Sudov, 1993]. The INC model is composed of 4 stages: primordial pion production, direct emission (fast ejectiles) from the primordial pion-nucleon interaction, pre-equilibrium

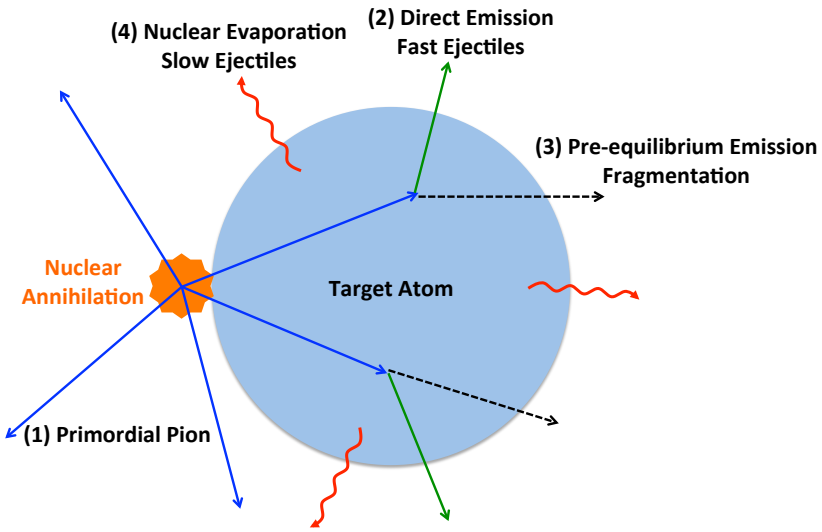

Figure 7.13: Schematic of INC model. (1) The primordial pions ($\pi^{\pm}$, π^{0}) are produced in the nuclear annihilation. (2) Some of the pions hit the nucleons in the nucleus with direct emission (fast ejectiles), followed by (3) the pre-equilibrium emission (fragmentation) and (4) the nuclear evaporation (slow ejectiles).

emission (multi-fragmentation) from excited nucleus, and nuclear evaporation (slow ejectiles). The antiproton is first assumed to annihilate at the surface of a single nucleon of the nucleus and to produce the primordial pions ($\pi^{\pm}$, π^{0}). Some of these pions may escape from the nucleus, but the others cascade through the nucleons of the nucleus, knocking out fast nucleons as they go through. Due to this interaction, the nucleons in the nucleus are excited and their energy density distribution becomes quite non-thermal. Therefore, the nucleus can break into pieces with the emission of fragmented particles. The characteristic time of this process is $\sim 10^{-22}$ s. Then the density distribution becomes more thermal and the remaining excitation energy will be removed by nuclear evaporation, which emits slow ejectiles. Figure 7.13 shows an overview of the INC model processes.

The INC model can also be applied to the antideuteron annihilation, resulting in two models that have been built based on how the two antinucleons in the antideuteron interact with nuclei [Cugnon, 1992]. The first model (model A) assumes that the two antinucleons

interact with the nucleons simultaneously, while the second model (model B) assumes that the antinucleons interact with nucleons separately. The pion and proton multiplicities can then be estimated with the INC model. We will discuss how we can use the model to distinguish antideuterons from antiprotons in the following sections.

7.5.2 Pion Multiplicity

The number of primordial pions ($\pi^{\pm}$, π^0) in the INC model is estimated based on antiproton-nucleon annihilation. This annihilation has been well studied, and much experimental data are available. The pion multiplicity and the standard deviation for the antiproton-nucleon annihilation is estimated as follows [Cugnon, 1989; Cugnon, 1992]:

$$\langle M^p_{\pi^{\pm},\pi^0} \rangle = 2.65 + 3.65 \ln \sqrt{s} \tag{7.1}$$

$$\frac{\sigma^2}{\langle M^p_{\pi^{\pm},\pi^0} \rangle} = 0.174 \left(\sqrt{s}\right)^{0.40}. \tag{7.2}$$

Here, $\langle M^p_{\pi^{\pm},\pi^0} \rangle$ is the average number of primordial pions ($\pi^{\pm}$, π^0), and s is the center of mass energy in GeV. Eq 7.1 and Eq 7.2 agree well with the experimental data [Cugnon, 1989]. The average number of pions, $\langle M^p_{\pi^{\pm},\pi^0} \rangle$, and the average number of charged pions, $\langle M^p_{\pi^{\pm}} \rangle$, for the antiproton-nucleon annihilation at rest are 5.1 and 3.1, respectively.

Most of the primordial pions can escape from the nucleus, but some of them interact and cascade through the nucleons, producing emission of fast nucleons. The interaction probability can be geometrically estimated for each atom, A, and the average number of the final charged pions, $\langle M^f_{\pi^{\pm}} \rangle$, can be simply estimated as follows [Polster *et al.*, 1995; Cugnon *et al.*, 2001]:

$$\begin{aligned} \langle M^f_{\pi^{\pm}} \rangle &= \langle M^p_{\pi^{\pm}} \rangle \cdot P(A) \\ P(A) &\sim 1 - \frac{\Omega(A)}{4\pi}. \end{aligned}$$

$$\begin{aligned} \Omega(A) &= 2\pi(1 - cos\theta) \\ &= 2\pi \left(1 - \sqrt{1 - \left(\frac{r_0 A^{1/3}}{r_0 A^{1/3} + \delta} \right)^2} \right) \end{aligned}$$

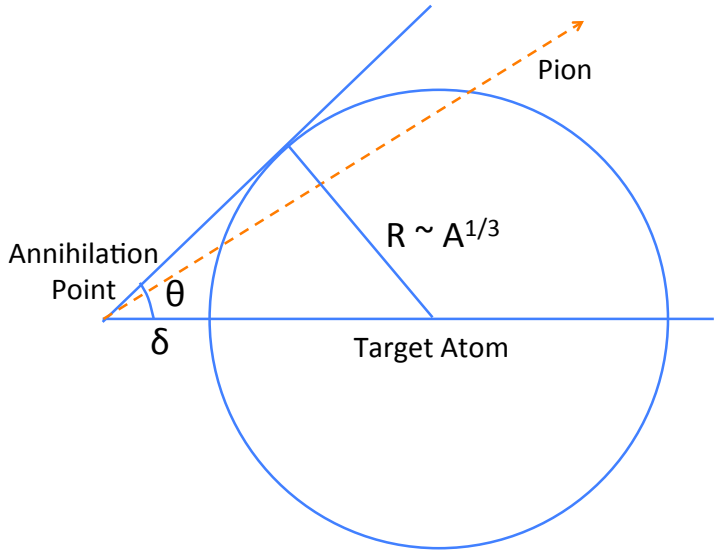

Figure 7.14: Schematic of the interaction probability for primordial pions with the nucleons in the atom

Here, $P(A)$ is the interaction probability, $\Omega(A)$ is the solid angle that the pion can hit the nucleons in the atom, and r_0 and δ are the radius parameters, 1.2 fm and 1.6 fm, respectively [Cugnon *et al.*, 2001] (See Figure 7.14). As seen in Figure 7.15, the INC model agrees well with the antiprotonic experimental data [Polster *et al.*, 1995]. Note that the pion multiplicity reduces by only 0.3 as the nuclei changes from $A = 10$ to $A = 200$.

The distribution of the final pion multiplicity for antiproton annihilation on a target nucleus was estimated by using Eq 7.1 and Eq 7.2 with $s = 2$ GeV to obtain the primordial pions ($\pi^{\pm}$, π^0) and using the simple Monte Carlo simulation to model the interaction of pions and nucleons. It is assumed that the direction of the primordial pions is isotropic and the probability for them to be absorbed in the nucleons is $P(A)$ in the Monte Carlo simulation.

The primordial pion multiplicity for the antideuteron annihilation at rest on nuclei was also estimated with Eq 7.1 and Eq 7.2, by simply changing $s = 4\ GeV$ in model A and $s = 2\ GeV$ for each antinucleon in model B, by assuming $\langle M_{\pi^+} \rangle = \langle M_{\pi^-} \rangle = \langle M_{\pi^0} \rangle$ in the simulation to simplify the model.

Figure 7.16 shows the primordial pion multiplicity for antiproton and antideuteron an-

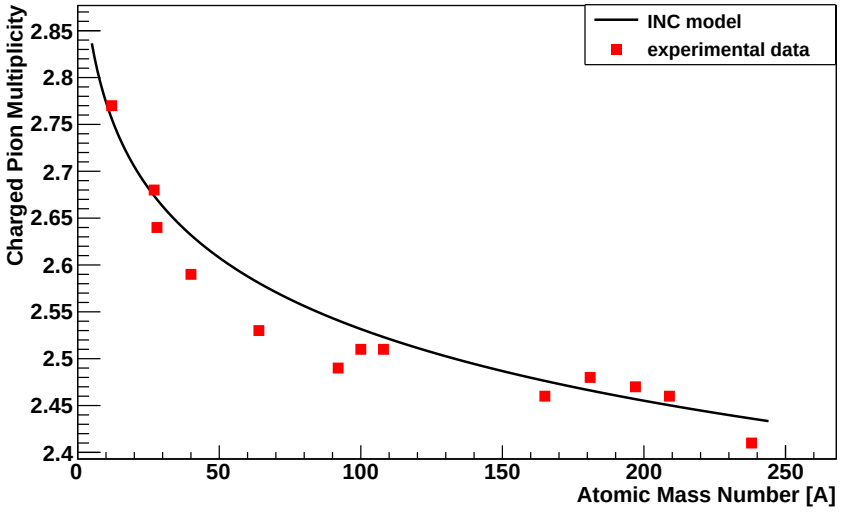

Figure 7.15: INC model vs. experimental data for the charged pion multiplicity

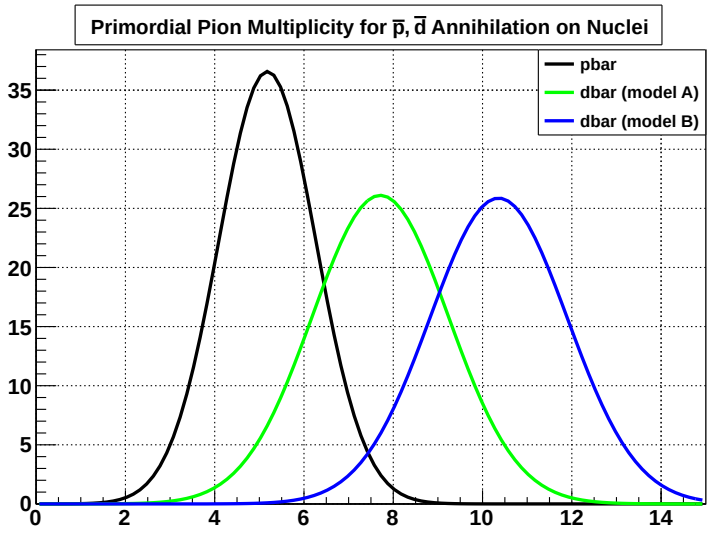

Figure 7.16: Primordial pion multiplicity ($\pi^{\pm}$, π^{0}) for antiproton and antideuteron annihilations at rest on nuclei

nihilations at rest on nuclei. Figure 7.17 shows the primordial charged pion multiplicity for the antiproton and antideuteron annihilations at rest on nuclei and the experimental data.

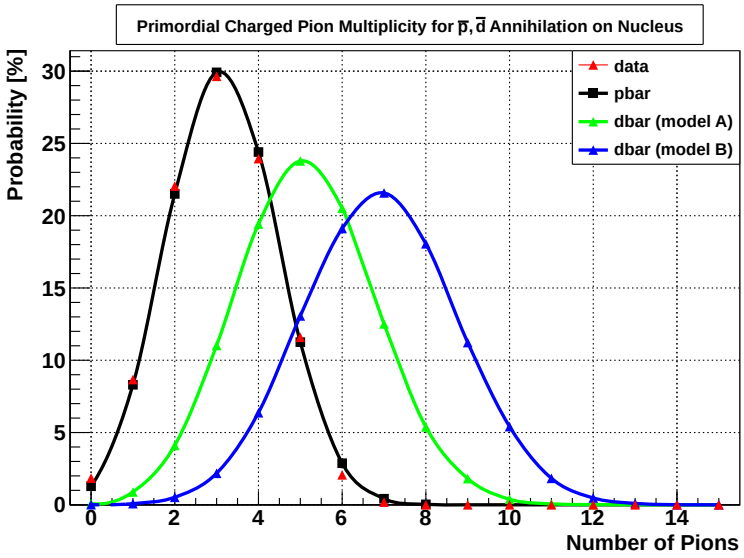

Figure 7.17: Primordial charged pion multiplicity for antiproton and antideuteron annihilations at rest on nuclei

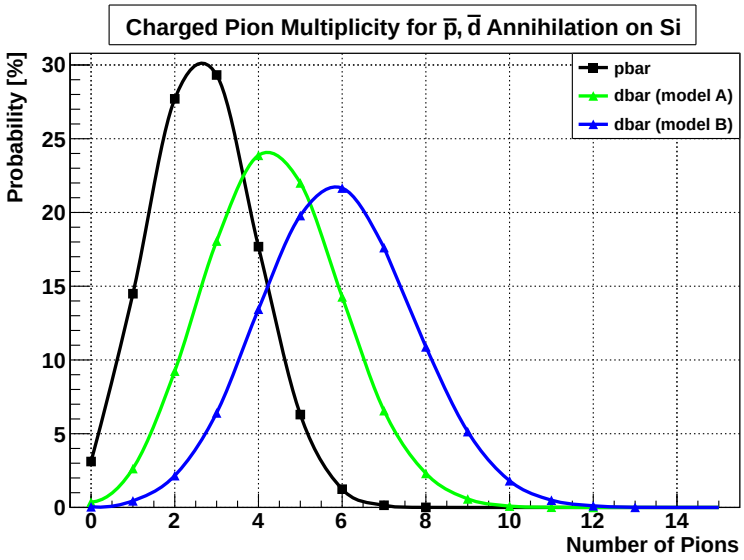

Figure 7.18: Final charged pion multiplicity for antiproton and antideuteron annihilations at rest on Si

Table 7.2: Pion multiplicity, acceptance and rejection factor for antiproton and antideuteron annihilations at rest on Si

$\langle M_{\pi^\pm} \rangle$	$a_\pi^{\bar{p}}$	r_π	$a_\pi^{\bar{d},A}$	$a_\pi^{\bar{d},B}$
≥ 3	54.7%	2	87.8%	97.4%
≥ 4	25.4%	4	69.7%	91.0%
≥ 5	7.69%	13	45.8%	77.5%
≥ 6	1.39%	72	23.8%	57.7%
≥ 7	0.15%	667	9.55%	36.1%
≥ 8	0.01%	10000	3.00%	18.5%

Figure 7.18 shows the final charged pion multiplicity for the antiproton and antideuteron annihilations at rest on Si. Table 7.2 shows the probability to produce each multiplicity of pions in the antiproton and antideuteron annihilations at rest on Si. As seen in Table 7.2, six or more pion multiplicity provides an antiproton rejection factor of $r_{\pi \geq 6} \sim 72$ $(= 1/a_{\pi \geq 6}^{\bar{p}})$ with an antideuteron acceptance of $a_{\pi \geq 6}^{\bar{d},A} = 0.24$ for model A and $a_{\pi \geq 6}^{\bar{d},B} = 0.58$ for model B.

7.5.3 Proton Multiplicity

The INC model also predicts the proton and neutron production in the following processes: (1) direct emission from the interaction between the primordial pions ($\pi^\pm$, π^0) and the nucleons, (2) pre-equilibrium emission (multi fragmentation) from excited nucleons, and (3) nuclear evaporation. The energy spectrum of the proton is estimated with the Maxwell-Boltzmann distribution as given below, based on fitting of the experimental data for antiproton annihilation at rest on nuclei [Polster *et al.*, 1995]:

$$\frac{dM}{dE} = \frac{2\langle M \rangle}{\sqrt{\pi T^3}} \sqrt{E} \exp\left(-\frac{E}{T}\right).$$

Here, $\langle M \rangle$ is the average number of protons produced in the antiproton annihilation at rest on Si, 0.86 ± 0.05, E is the energy of the proton, 10 MeV - 300 MeV, and T is the parameter fitted to the data. If the energy of the proton is too small, it will stop quickly and could not

be tracked by the detector layers. Therefore, we set the lower cut of the proton energy as 60 MeV to guarantee passage through three or more Si(Li) layers. The proton multiplicity with $E \geq 60$ MeV, $\langle M_{\bar{p}}^{\geq 60MeV} \rangle$, is 0.37.

Unfortunately, there is no data available in the INC model for the antideuteron annihilation at rest on Si. However, Cugnon et al. [Cugnon, 1992] estimated the proton and neutron multiplicity with $E \geq 60$ MeV for the antideuteron annihilation at rest on Mo (Molybdenum). Thus, we simply estimated the proton multiplicity on Si using the ratio of the proton multiplicity in the antiproton annihilation at rest on Si to that on Mo. We also assumed the relationship between the proton and neutron multiplicity follows [Polster *et al.*, 1995]

$$\frac{\langle M_n \rangle / \langle M_p \rangle}{N/Z} \sim 2. \tag{7.3}$$

Here, N is the number of neutrons in the atom, and Z is the atomic number (number of protons in the atom). Considering the above, the proton multiplicity for the antideuteron annihilation on Si with $E \geq 60$ MeV becomes 2.35 for model A and 1.76 for model B. Since the distribution of the proton multiplicity is not well known, it was estimated with the poisson distribution. Table 7.3 shows the probability to produce a given multiplicity of protons in the antiproton and antideuteron annihilations at rest on Si. As seen in Table 7.3, a proton multiplicity of three or more protons provides an antiproton rejection factor of $r_{p\geq 3} \sim 160$ $(= 1/a_{p\geq 3}^{\bar{p}})$ with the antideuteron acceptance of $a_{p\geq 3}^{\bar{d}} = 0.42$ for model A and $a_{p\geq 3}^{\bar{d}} = 0.26$.

7.6 Depth Sensing and dE/dX Energy Loss

Since the GAPS detector is composed of 13 layers of Si(Li) detectors, the incoming particle can be tracked in the TOF paddles and Si(Li) layers, and the number of layers that the incoming particle went through before stopping in the detector, provides the stopping range for incoming particles. As seen in the scaling law of the stopping range (Eq 7.4) [Leo, 1987], the stopping range for the antideuteron can be roughly twice as large as that for the antiproton with the same velocity.

Table 7.3: Proton multiplicity, acceptance and rejection factor for antiproton and antideuteron annihilations at rest on Si

$\langle M_p \rangle$	$a_p^{\bar{p}}$	r_p	$a_p^{\bar{d},A}$	$a_p^{\bar{d},B}$
≥ 1	30.7%	3	90.4%	82.7%
≥ 2	5.29%	19	68.0%	52.4%
≥ 3	0.63%	158	41.7%	25.7%
≥ 4	0.06%	1667	21.1%	10.2%
≥ 5	0.004%	25000	8.92%	3.32%

$$R_{\bar{d}}(T_{\bar{d}}) = \frac{m_{\bar{d}}}{m_{\bar{p}}} \frac{z_{\bar{p}}^2}{z_{\bar{d}}^2} R_{\bar{p}} \left(T_{\bar{d}} \frac{m_{\bar{p}}}{m_{\bar{d}}} \right) \tag{7.4}$$

Here, $R_{\bar{d}}$ ($R_{\bar{p}}$) is the stopping range of antideuterons (antiprotons), $m_{\bar{d}}$ ($m_{\bar{p}}$) is the mass of antideuterons (antiprotons), $z_{\bar{d}}$ ($z_{\bar{p}}$) is the charge of antideuterons (antiprotons) and $T_{\bar{d}}$ ($T_{\bar{p}}$) is the kinetic energy of antideuterons (antiprotons).Therefore, antideuterons can be distinguished from antiprotons by using the stopping range (depth sensing) and the TOF timing. Note that if the incoming antiparticle stops in the frame rather in the Si(Li) detector, the stopped position can be determined by tracking from the annihilation products (pions and protons) backwards in the detector layers, since they should be produced at one point (annihilation point).

A GEANT4 simulation was conducted to estimate how large a rejection factor can be obtained from depth sensing. The simulation was done using protons and deuterons, since antideuterons are not defined in GEANT4 and their stopping ranges are the same as antiprotons and antideuterons excluding the fact that they do not annihilate in flight. The two different incoming angles, 0 deg and 45 deg, were simulated taking into account the angular resolution of the TOF system, $\sim$ 5 deg. Figure 7.19 (7.20) shows the relationship between the stopped layer and the TOF timing with the incoming angle, $\sim$ 0 (45) deg. An antideuteron can go deeper than an antiproton with the same TOF, as expected. Since the resolution of the depth sensing is related to the effective thickness of the Si(Li) layer,

the performance of the depth sensing becomes worse as the incoming angle increases, as seen in Figures 7.19 and Figure 7.20. Figure 7.21 is the histogram of the number of layers crossed before stopping (stopping range) for a fixed TOF of 10 $\pm$ 0.5 ns. Here, 0.5 ns is the timing resolution of the TOF system as previously discussed. Since the antideuteron tends to stop in deeper layers than an $\bar{p}$ with same TOF, by requiring at least 8 layers crossed, an antiproton rejection power of > 100 with an antideuteron acceptance of $\sim 75\%$ can be obtained.

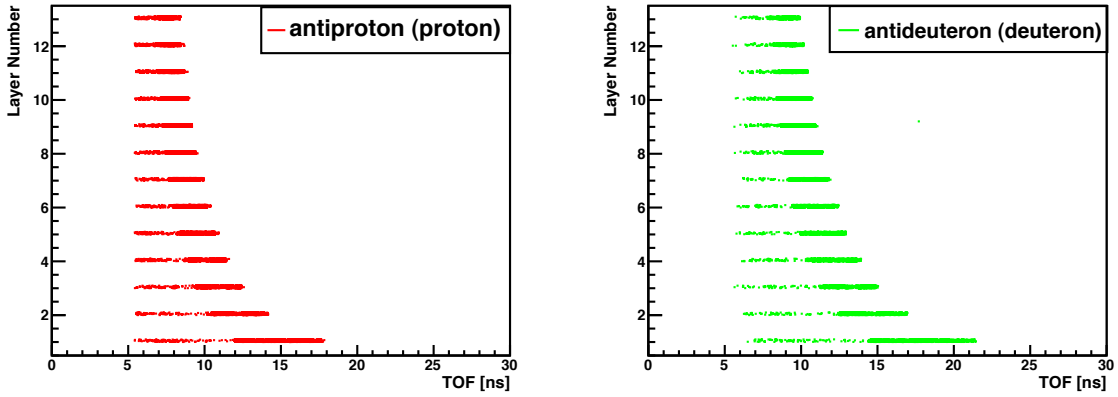

Figure 7.19: Stopped layer vs. TOF timing for protons (left) and deuterons (right) with the incoming angle $\sim$ 0 deg.

The distribution of stops with layer number in Figure 7.21 is broadened because the stopping powers of the Si(Li) detector and the frame (including the cable and electronics) are different and the total mass traversed by the incoming particle before reaching the final layer varied widely. Therefore, the resolution of the depth sensing can be improved by adding mass information along the trajectory in each event. For example, in the real measurement, we can easily determine how many Si(Li) detectors and frames the incoming particle went through before stopping. Figure 7.22 shows the depth sensing for the fixed TOF of 10 $\pm$ 0.5 ns and incoming angle of 0 deg, with the additional requirement that the incoming particle went through at least two Si(Li) detectors before stopping. By applying a depth cut of $\geq$ 6 layers crossed, the antiproton rejection factor becomes $\gg 100$ with $\sim$ 98 % antideuteron acceptance. The detector calibration in flight (and the beam test on the

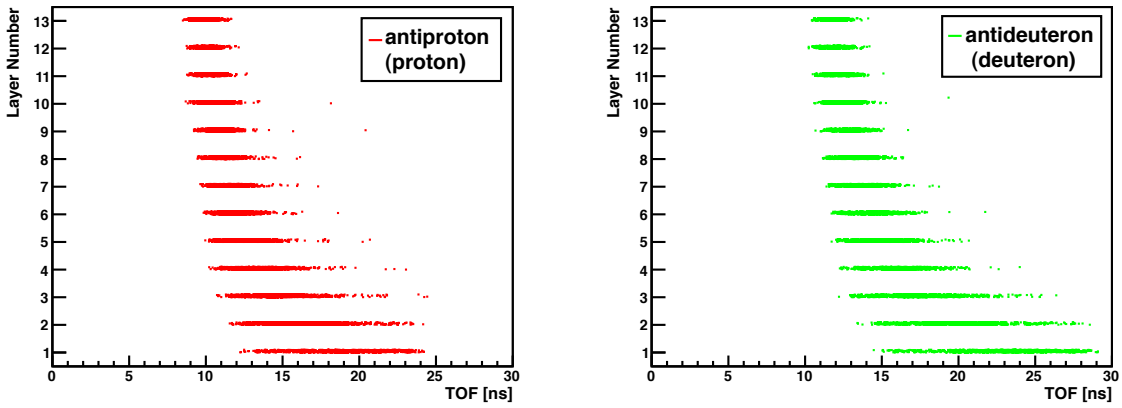

Figure 7.20: Stopped layer vs. TOF timing for protons (left) and deuterons (right) with the incoming angle $\sim$ 45 deg.

ground) can provide more detailed mass information on the trajectory for each event, which will enhance the performance of the depth sensing.

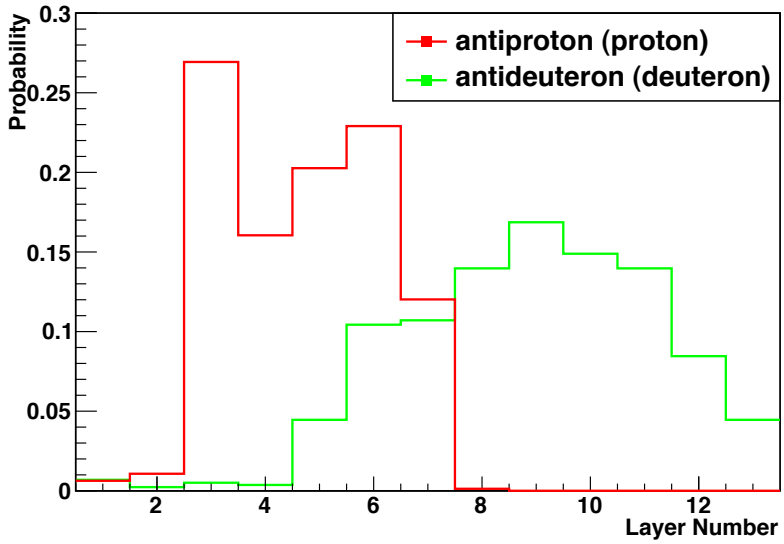

Figure 7.21: Depth sensing for protons (red) and deuterons (green) with the TOF $\sim$ 10 $\pm$ 0.5 ns and the incoming angle $\sim$ 0 deg.

Furthermore, dE/dX energy deposit in the Si(Li) detector can also be used to distinguish

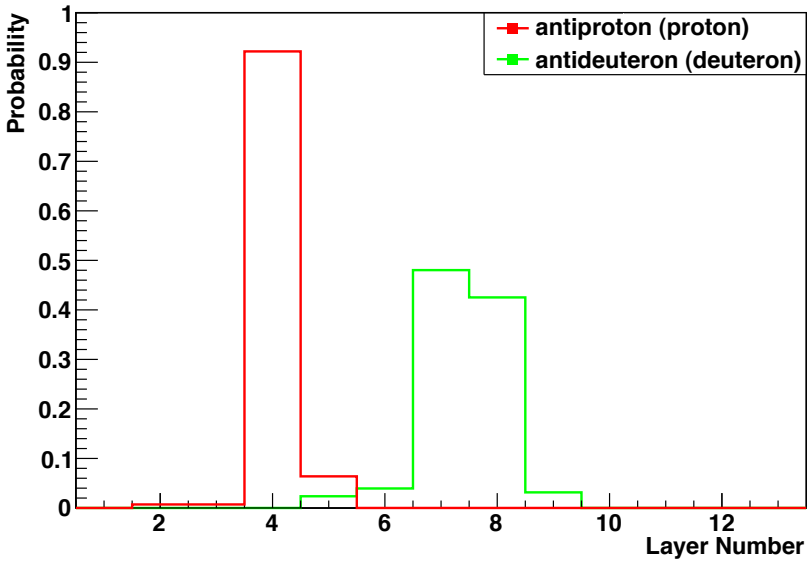

Figure 7.22: Depth sensing for protons and deuterons with the TOF $\sim$ 10 $\pm$ 0.5 ns and the incoming angle $\sim$ 0 deg and the additional information "the incoming particle hit two Si(Li) detectors before stopping".

antideuterons from antiprotons; as discussed above, the stopping range for an antideuteron can be roughly twice as large as that for an antiproton with the same velocity. Therefore, the antideuteron with the same stopping range as the antiproton should have smaller velocity (β) than the antiproton. Since the dE/dX loss is proportional to $1/\beta^2$ at low energy (E $<$ 1 GeV) [Leo, 1987], the antideuteron can deposit more energy in each layer.

Figure 7.23 shows the dE/dX energy loss for antiprotons (red) and antideuterons (green) with an incoming angle $\sim$ 0 deg. Here we assumed that the incoming particle hit the Si(Li) detector at layer 3 and stopped at layer 6. By requiring, dE/dX $\geq$ 8 MeV, the antiproton rejection factor becomes $\gg$ 100, with $\sim$ 85% antideuteron acceptance. Figure 7.24 shows the dE/dX energy loss for antiprotons (red) and antideuterons (green) with the incoming angle $\sim$ 45 deg. Since the effective thickness of the detector becomes larger, the distribution of the dE/dX loss is broader compared to the result for the $\sim$ 0 deg incoming angle. In this case, the antiproton rejection factor obtained by requiring dE/dX $\geq$ 8 MeV is $\gg$ 100, with $\sim$ 50% antideuteron acceptance. Since the effective area of the Si(Li) detector in each layer

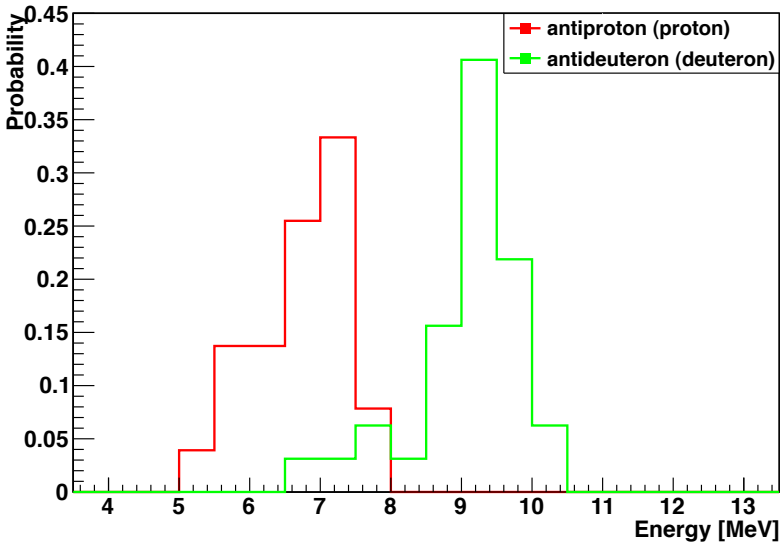

Figure 7.23: dE/dX energy loss for antiprotons (red) and antideuterons (green) with the incoming angle ~ 0 deg. Here, we assumed that the incoming particle hit the Si(Li) detector at layer 3 and stopped at layer 6.

is $\sim 63\%$ of the total layer area, the probability of the incoming particle hitting more than one Si(Li) detector will increase as the particle goes through more layers, yielding a higher antiproton rejection. For example, if the particle goes through 3 layers before stopping, the probability that it hits more than one detector is $\sim 95\%$ and the probability that it hits more than two detectors is $\sim 70\%$.

Considering the above, we conservatively conclude that the antiproton rejection factor can be 100 with an 80% antideuteron acceptance from the depth sensing, and 100 with an 80% antideuteron acceptance from the dE/dX loss.

7.7 Sensitivity and Confidence Level

Since the major background is the antiproton event, the confidence level (CL) for one antideuteron detection can be estimated based on the Poisson distribution and the number of antiprotons misidentified as antideuterons, $N_{\bar{p}}^{mimic}$, as below. $N_{\bar{p}}^{mimic}$ can be calculated based on antiproton events, which satisfy all the applied cuts discussed above. The GAPS

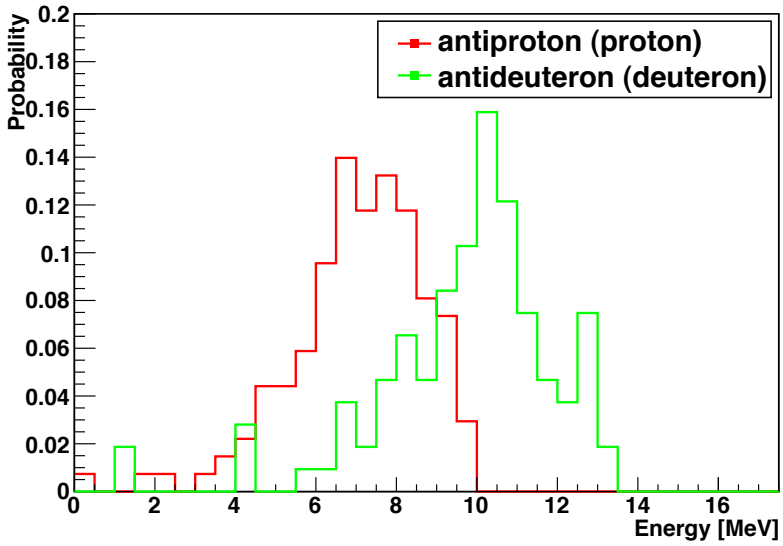

Figure 7.24: dE/dX energy loss for antiprotons (red) and antideuterons (green) with the incoming angle $\sim$ 45 deg. Here, we assumed that the incoming particle hit the Si(Li) detector at layer 3 and stopped at layer 6.

sensitivity was estimated with $\sim$ 98% CL by combining the antiproton rejection factors.

$$\begin{aligned} CL &= P(N=0, \lambda = N_{\bar{p}}^{mimic}) \\ &\sim 1 - N_{\bar{p}}^{mimic} \\ &= 1 - \langle F_{\bar{p}} \cdot \Gamma_{\bar{p}} \cdot \epsilon_g \cdot T \cdot \epsilon_T \rangle_{\Delta E} \, \Delta E \cdot \prod_i a_i^{\bar{p}} \\ & P(N, \lambda) = \frac{e^{-\lambda} \lambda^N}{N!} \end{aligned}$$

Here, P is the Poisson distribution with the observation value N and the mean λ, $F_{\bar{p}}$ is the antiproton flux at the top of atmosphere, $\sim 2.0 \times 10^{-2}$ [$\mathrm{m^{-2}s^{-1}sr^{-1}(GeV/n)^{-1}}$], $\Gamma_{\bar{p}}$ is the GRASP for antiprotons, ϵ_g is the parameter for the geomagnetic cutoff, T is the flight time, ϵ_T is the ratio of the observation time to the flight time ($\sim$ 1.0), ΔE is the energy band for the measurement (0.25 GeV/n in the simulation), $a_i^{\bar{p}}$ is the acceptance (1/rejection factor, r_i) for each cut and i is the cut type (atomic X-ray, pion and proton multiplicity, depth and dE/dX). The geomagnetic cutoff is the minimum energy of a cosmic ray particle

that can reach the top of the atmosphere, and it is estimated as ~ 0.75 for ~ 0.2 GeV/n [Doetinchem, 2012]. The antiproton rejection factor for each cut and the corresponding antideuteron acceptance discussed in the previous sections are shown in Table 7.4.

Table 7.4: Rejection factor and acceptance for each cut

Cut Type (i)	$a_i^{\bar{p}}$	$r_i = 1/a_i^{\bar{p}}$	$a_i^{\bar{d},A}$	$a_i^{\bar{d},B}$
X-ray ≥ 1	0.12%	84	10%	10%
$\langle M_{\pi^\pm} \rangle \geq 6$	1.39%	72	23.8%	57.7%
$\langle M_{\pi^\pm} \rangle \geq 7$	0.15%	667	9.55%	36.1%
$\langle M_p \rangle \geq 3$	0.63%	158	41.7%	25.7%
$\langle M_p \rangle \geq 4$	0.06%	1667	21.1%	10.2%
depth	1%	100	80%	80%
dE/dX	1%	100	80%	80%

The corresponding antideuteron sensitivity, $S_{\bar{d}}$, with the same cuts used above can be estimated as follows.

$$S_{\bar{d}} = \frac{1}{\langle \Gamma_{\bar{d}} \cdot \epsilon_g \cdot T \cdot \epsilon_T \rangle_{\Delta E} \, \Delta E \cdot \prod_i a_i^{\bar{d}}}$$

Different combinations of the cuts provide different values of CL and sensitivity. In order to obtain the optimized sensitivity with CL $\sim 98\%$, we considered the combination of one or more cuts from these cuts, X-rays ≥ 1, $\langle M_{\pi^\pm} \rangle \geq 6$ and $\langle M_p \rangle \geq 3$, in addition to depth sensing and dE/dX cuts. Note that we assumed each cut type is not correlated to each other in the calculation. This combination provides a 1.1×10^6 antiproton rejection factor and $\sim 65\%$ antideuteronic acceptance. The corresponding antideuteron sensitivity is 1.4×10^{-6} [$\mathrm{m^{-2}s^{-1}sr^{-1}(GeV/n)^{-1}}$] for LDB flight and 3.4×10^{-7} [$\mathrm{m^{-2}s^{-1}sr^{-1}(GeV/n)^{-1}}$] for ULDB flight with $\sim 99.4\%$ and 97% CL, respectively.

7.8 GAPS vs. AMS

AMS-02, launched in 2011, is the only current antideuteron search experiment. AMS probes two different energy regions, $0.2 < E < 0.8$ GeV/n and $2.2 < E < 4.2$ GeV/n

[F.Giovacchini, 2007]. However, the primary antideuteron flux in the higher energy region may be contaminated by the secondary flux (produced by cosmic ray interactions). The sensitivity for a 5-year AMS observation is shown in Figure 7.25, which was estimated based on the Poisson distribution and the number of misidentified events as antideuterons, using the same code for the geomagnetic cutoff as used by GAPS [F.Giovacchini, 2007; Doetinchem, 2012]. For comparison with GAPS, we used 5 years for the AMS observation time, since the GAPS experiment is planned to take place in 5 years. The CL in Figure 7.25 is $\sim 98\%$ for both GAPS and AMS. The AMS sensitivity is a best case analysis, since it is based on the published performance of AMS with a superconducting magnet. Results on sensitivity with the non-superconducting magnet, which is actually used on AMS-02, are not yet published. The sensitivity for the GAPS 60 day LDB flight is as good as the 5 year AMS observation, and the sensitivity for the GAPS 300 day ULDB flight can be $\sim$ four times better than the 5-year AMS observation.

If AMS detects antideuterons, a GAPS LDB experiment can confirm the detection using a different detection technique with a completely different background. Using complementary techniques with different background systematics is crucial in rare event searches. Note that GAPS complements existing and planned underground direct detection experiments, which detect dark matter particles via their recoils on target nuclei, as well as other indirect search methods. Exploiting the detection or even non-detection of dark matter with complementary approaches can lead to tighter constraints on theoretical models.

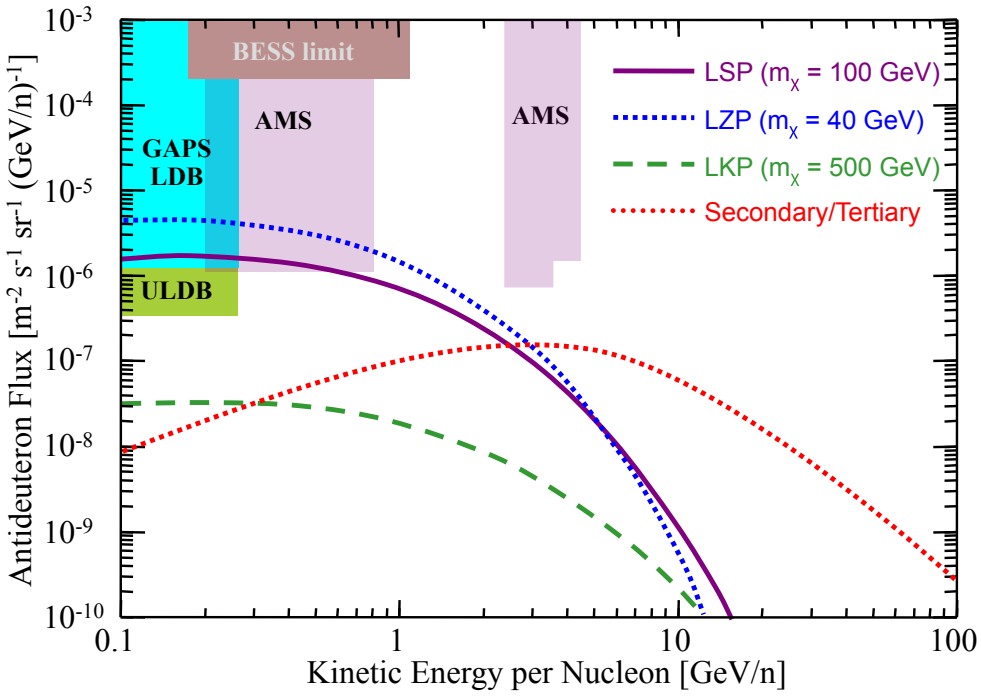

Figure 7.25: Antideuteron flux at the top of the atmosphere, compared with the BESS upper limit[Fuke *et al.*, 2005], and GAPS and AMS sensitivity ($\sim$ 97% confidence level). The sensitivity for the AMS 5 year flight was estimated with the superconducting magnet, based on [F.Giovacchini, 2007; Doetinchem, 2012]. The blue dashed line (LZP), black dotted line (LSP), and green dot-dashed line (LKP) represent the primary antideuteron fluxes due to the dark matter annihilations [Baer and Profumo, 2005]. The red solid line represents the secondary/tertiary flux due to the cosmic ray interactions [Duperray *et al.*, 2005; Salati *et al.*, 2010].

Bibliography

[Aalseth *et al.*, 2011] C. Aalseth, P. Barbeau, N. Bowden, B. Cabrera-Palmer, J. Colaresi, J. Collar, S. Dazeley, P. de Lurgio, J. Fast, N. Fields, C. Greenberg, T. Hossbach, M. Keillor, J. Kephart, M. Marino, H. Miley, M. Miller, J. Orrell, D. Radford, D. Reyna, O. Tench, T. Van Wechel, J. Wilkerson, and K. Yocum. Results from a Search for Light-Mass Dark Matter with a p-Type Point Contact Germanium Detector. *Physical Review Letters*, 106(13):1–4, March 2011.

[Abdo *et al.*, 2009] a. Abdo, M. Ackermann, M. Ajello, W. Atwood, M. Axelsson, L. Baldini, J. Ballet, G. Barbiellini, D. Bastieri, M. Battelino, B. Baughman, K. Bechtol, R. Bellazzini, B. Berenji, R. Blandford, E. Bloom, G. Bogaert, E. Bonamente, a. Borgland, J. Bregeon, a. Brez, M. Brigida, P. Bruel, T. Burnett, G. Caliandro, R. Cameron, P. Caraveo, P. Carlson, J. Casandjian, C. Cecchi, E. Charles, a. Chekhtman, C. Cheung, J. Chiang, S. Ciprini, R. Claus, J. Cohen-Tanugi, L. Cominsky, J. Conrad, S. Cutini, C. Dermer, a. de Angelis, F. de Palma, S. Digel, G. Di Bernardo, E. do Couto e Silva, P. Drell, R. Dubois, D. Dumora, Y. Edmonds, C. Farnier, C. Favuzzi, W. Focke, M. Frailis, Y. Fukazawa, S. Funk, P. Fusco, D. Gaggero, F. Gargano, D. Gasparrini, N. Gehrels, S. Germani, B. Giebels, N. Giglietto, F. Giordano, T. Glanzman, G. Godfrey, D. Grasso, I. Grenier, M.-H. Grondin, J. Grove, L. Guillemot, S. Guiriec, Y. Hanabata, a. Harding, R. Hartman, M. Hayashida, E. Hays, R. Hughes, G. Jóhannesson, a. Johnson, R. Johnson, W. Johnson, T. Kamae, H. Katagiri, J. Kataoka, N. Kawai, M. Kerr, J. Knödlseder, D. Kocevski, F. Kuehn, M. Kuss, J. Lande, L. Latronico, M. Lemoine-Goumard, F. Longo, F. Loparco, B. Lott, M. Lovellette, P. Lubrano, G. Madejski, a. Makeev, M. Massai, M. Mazziotta, W. McConville, J. McEnery, C. Meurer, P. Michelson,

W. Mitthumsiri, T. Mizuno, a. Moiseev, C. Monte, M. Monzani, E. Moretti, a. Morselli, I. Moskalenko, S. Murgia, P. Nolan, J. Norris, E. Nuss, T. Ohsugi, N. Omodei, E. Orlando, J. Ormes, M. Ozaki, D. Paneque, J. Panetta, D. Parent, V. Pelassa, M. Pepe, M. Pesce-Rollins, F. Piron, M. Pohl, T. Porter, S. Profumo, S. Rainò, R. Rando, M. Razzano, a. Reimer, O. Reimer, T. Reposeur, S. Ritz, L. Rochester, a. Rodriguez, R. Romani, M. Roth, F. Ryde, H. Sadrozinski, D. Sanchez, a. Sander, P. Saz Parkinson, J. Scargle, T. Schalk, a. Sellerholm, C. Sgrò, D. Smith, P. Smith, G. Spandre, P. Spinelli, J.-L. Starck, T. Stephens, M. Strickman, a. Strong, D. Suson, H. Tajima, H. Takahashi, T. Takahashi, T. Tanaka, J. Thayer, J. Thayer, D. Thompson, L. Tibaldo, O. Tibolla, D. Torres, G. Tosti, a. Tramacere, Y. Uchiyama, T. Usher, a. Van Etten, V. Vasileiou, N. Vilchez, V. Vitale, a. Waite, E. Wallace, P. Wang, B. Winer, K. Wood, T. Ylinen, and M. Ziegler. Measurement of the Cosmic Ray e++e- Spectrum from 20GeV to 1TeV with the Fermi Large Area Telescope. *Physical Review Letters*, 102(18):6–11, May 2009.

[Adriani *et al.*, 2009] O Adriani, G C Barbarino, G a Bazilevskaya, R Bellotti, M Boezio, E a Bogomolov, L Bonechi, M Bongi, V Bonvicini, S Bottai, a Bruno, F Cafagna, D Campana, P Carlson, M Casolino, G Castellini, M P De Pascale, G De Rosa, N De Simone, V Di Felice, a M Galper, L Grishantseva, P Hofverberg, S V Koldashov, S Y Krutkov, a N Kvashnin, a Leonov, V Malvezzi, L Marcelli, W Menn, V V Mikhailov, E Mocchiutti, S Orsi, G Osteria, P Papini, M Pearce, P Picozza, M Ricci, S B Ricciarini, M Simon, R Sparvoli, P Spillantini, Y I Stozhkov, a Vacchi, E Vannuccini, G Vasilyev, S a Voronov, Y T Yurkin, G Zampa, N Zampa, and V G Zverev. An anomalous positron abundance in cosmic rays with energies 1.5-100 GeV. *Nature*, 458(7238):607–9, April 2009.

[Allbritton *et al.*, 2002] G.L. Allbritton, H. Andersen, and A. Barnes. Large diameter lithium compensated silicon detectors for the NASA Advanced Composition Explorer (ACE) mission. *Nuclear Science,*, 43(3 Part 2):1505–1509, 2002.

[Amsler, 1998] Claude Amsler. Proton-antiproton annihilation and meson spectroscopy with the Crystal Barrel. *Reviews of Modern Physics*, 70(4):1293–1339, 1998.

[Aprile *et al.*, 2011] E Aprile, K Arisaka, F Arneodo, and A Askin. Dark matter results from 100 live days of XENON100 data. *Physical review ...*, 1:8–12, 2011.

[Aprile *et al.*, 2012] E Aprile, M Alfonsi, and K Arisaka. Analysis of the XENON100 Dark Matter Search Data. *Arxiv preprint arXiv: ...*, pages 1–16, 2012.

[Asztalos *et al.*, 2006] Stephen J. Asztalos, Leslie J Rosenberg, Karl van Bibber, Pierre Sikivie, and Konstantin Zioutas. Searches for Astrophysical and Cosmological Axions*. *Annual Review of Nuclear and Particle Science*, 56(1):293–326, November 2006.

[Baer and Profumo, 2005] H. Baer and S. Profumo. Low energy antideuterons: shedding light on dark matter. *Journal of Cosmology and Astroparticle Physics*, 2005(12):008–008, December 2005.

[Barrau *et al.*, 2005] A Barrau, P Salati, G Servant, and F Donato. Kaluza-Klein dark matter and galactic antiprotons. *Physical Review D*, 2005.

[Batty and Friedman, 1984] CJ Batty and E Friedman. Optical potentials for low energy antiproton-nucleus interactions. *Physics Letters B*, 142(4):241–244, 1984.

[Batty, 1981a] CJ Batty. Optical-model analysis of exotic atom data (I). Kaonic atoms. *Nuclear Physics A*, 372:418–432, 1981.

[Batty, 1981b] CJ Batty. Optical-model analysis of exotic atom data (II). Antiprotonic and sigma atoms. *Nuclear Physics A*, 372:433–444, 1981.

[Belli *et al.*, 2002] P. Belli, R. Cerulli, N. Fornengo, and S. Scopel. Effect of the galactic halo modeling on the DAMA-NaI annual modulation result: An extended analysis of the data for weakly interacting massive particles with a purely spin-independent coupling. *Physical Review D*, 66(4):1–17, August 2002.

[Bonechi *et al.*, 2010] L Bonechi, M Bongi, V Bonvicini, S Borisov, and S Bottai. PAMELA results on the cosmic-ray antiproton flux. *Physics*, pages 1–11, 2010.

[Chang *et al.*, 2008] J Chang, J H Adams, H S Ahn, G L Bashindzhagyan, M Christl, O Ganel, T G Guzik, J Isbert, K C Kim, E N Kuznetsov, M I Panasyuk, a D Panov, W K H Schmidt, E S Seo, N V Sokolskaya, J W Watts, J P Wefel, J Wu, and V I Zatsepin. An excess of cosmic ray electrons at energies of 300-800 GeV. *Nature*, 456(7220):362–5, November 2008.

[Cheng *et al.*, 2002] HC Cheng, JL Feng, and KT Matchev. Kaluza-Klein dark matter. *Arxiv preprint hep-ph/0207125*, pages 1–4, 2002.

[Clowe *et al.*, 2004] Douglas Clowe, Anthony Gonzalez, and Maxim Markevitch. WEAK-LENSING MASS RECONSTRUCTION OF THE INTERACTING CLUSTER 1E 0657À558 : DIRECT EVIDENCE FOR THE EXISTENCE OF DARK MATTER. (1995):596–603, 2004.

[Cugnon *et al.*, 2001] J. Cugnon, S. Wycech, J. Jastrzbski, and P. Lubiski. Geometrical effects in antiproton annihilation on nuclei. *Physical Review C*, 63(2):1–4, January 2001.

[Cugnon, 1989] J. Cugnon. Antiproton-nucleus interaction. *Annales de Physique*, 152B(C):308–87, 1989.

[Cugnon, 1992] J. Cugnon. Antideuteron annihilation on nuclei. *Nuclear Physics, Section A*, 542(4):559–578, 1992.

[Doetinchem, 2012] P Doetinchem. (to be published). *Dark Matter 2012, UCLA*, 2012.

[Donato *et al.*, 2000] F. Donato, N. Fornengo, and P. Salati. Antideuterons as a signature of supersymmetric dark matter. *Physical Review D*, 62(4):43003, 2000.

[Donato *et al.*, 2008] F. Donato, N. Fornengo, and D. Maurin. Antideuteron fluxes from dark matter annihilation in diffusion models. *Physical Review D*, 78(4):18, August 2008.

[Duperray *et al.*, 2005] R. Duperray, B. Baret, D. Maurin, G. Boudoul, A. Barrau, L. Derome, K. Protasov, and M. Buénerd. Flux of light antimatter nuclei near Earth, induced by cosmic rays in the Galaxy and in the atmosphere. *Physical Review D*, 71(8):22, April 2005.

[Eisenberg, 1961] Y. Eisenberg. On the μ-mesonic atoms. *Il Nuovo Cimento (1955-1965)*, X(1957), 1961.

[Feng, 2010] Jonathan L Feng. Dark Matter Candidates from Particle Physics and Methods of Detection. 2010.

[F.Giovacchini, 2007] F.Giovacchini. CosmicRaysAnti-DeuteronFluxSensitivityof the AMS-02 Detector. *PhD thesis, Bologna University*, 2007.

[Fong *et al.*, 1982] A. Fong, J.T. Walton, E.E. Haller, H.A. Sommer, and J. Guldberg. Characterization of large diameter silicon by low-bias charge collection analysis in Si (Li) pin diodes. *Nuclear Instruments and Methods in Physics Research*, 199(3):623–630, 1982.

[Fuke *et al.*, 2005] H. Fuke, T. Maeno, K. Abe, S. Haino, Y. Makida, S. Matsuda, H. Matsumoto, J. Mitchell, A. Moiseev, J. Nishimura, M. Nozaki, S. Orito, J. Ormes, M. Sasaki, E. Seo, Y. Shikaze, R. Streitmatter, J. Suzuki, K. Tanaka, K. Tanizaki, T. Yamagami, A. Yamamoto, Y. Yamamoto, K. Yamato, T. Yoshida, and K. Yoshimura. Search for Cosmic-Ray Antideuterons. *Physical Review Letters*, 95(8):4, August 2005.

[Gaitskell, 2004] Richard J. Gaitskell. Direct Detection of Dark Matter. *Annual Review of Nuclear and Particle Science*, 54(1):315–359, December 2004.

[Gotta, 2004] D Gotta. Precision spectroscopy of light exotic atoms. *Progress in Particle and Nuclear Physics*, 52(1):133–195, March 2004.

[Goulding and Hansen, 1964] Fred S. Goulding and W. L. Hansen. An Automatic Lithium Drifting Apparatus for Silicon and Germanium Detectors. *IEEE Transactions on Nuclear Science*, 11(3):286–290, 1964.

[Hailey *et al.*, 2006] C J Hailey, T Aramaki, W W Craig, L Fabris, F Gahbauer, J E Koglin, N Madden, K Mori, H T Yu, and K P Ziock. Accelerator testing of the general antiparticle spectrometer; a novel approach to indirect dark matter detection. *Journal of Cosmology and Astroparticle Physics*, 2006(01):007–007, January 2006.

[Hailey, 2004] C Hailey. Development of the gaseous antiparticle spectrometer for space-based antimatter detection. *Nuclear Instruments and Methods in Physics Research Section B: Beam Interactions with Materials and Atoms*, 214:122–125, January 2004.

[Hartmann, 1990] F.J. Hartmann. Exotic atom cascade processes in atoms with z¿2. *Quantum*, pages 127–139, 1990.

[Hooper and Servant, 2005] Dan Hooper and G Servant. Indirect Detection of Dirac Right-Handed Neutrino Dark Matter. *Astroparticle Physics*, 2005.

[Hultqvist, 2011] Klas Hultqvist. IceCube: Physics, status, and future. *Nuclear Instruments and Methods in Physics Research Section A: Accelerators, Spectrometers, Detectors and Associated Equipment*, 626-627:S6–S12, January 2011.

[Jarosik *et al.*, 2011] N. Jarosik, C. L. Bennett, J. Dunkley, B. Gold, M. R. Greason, M. Halpern, R. S. Hill, G. Hinshaw, a. Kogut, E. Komatsu, D. Larson, M. Limon, S. S. Meyer, M. R. Nolta, N. Odegard, L. Page, K. M. Smith, D. N. Spergel, G. S. Tucker, J. L. Weiland, E. Wollack, and E. L. Wright. Seven-Year Wilkinson Microwave Anisotropy Probe (Wmap) Observations: Sky Maps, Systematic Errors, and Basic Results. *The Astrophysical Journal Supplement Series*, 192(2):14, February 2011.

[Koike *et al.*, 1996] T Koike, T Harada, and Y Akaishi. Cascade calculation of K -p and K -d atoms. *Physical review C: Nuclear physics*, 53(1):79–87, January 1996.

[Kunselman and Seki, 1973] Raymond Kunselman and R Seki. Strong interaction effects in antiproton and sigma-minus baryonic atoms. *Phys. Rev., C, v. 8, no. 6, pp. 2492-2494*, 8(6):6–8, 1973.

[Kuzichev, 1994] VF Kuzichev. The antiproton-nuclei annihilation cross-section at the momentum range from 0.70 to 2.50 GeV/c. *Nuclear Physics A*, 9474(94), 1994.

[L. Bergstrom, 2006] A. Goobar L. Bergstrom. *Cosmology and Particle Astrophysics*. Springer, Springer, 2006.

[Leo, 1987] W R Leo. *Techniques for Nuclear and Particle Physics Experiments*. 1987.

[Mori *et al.*, 2002] K Mori, CJ Hailey, EA Baltz, WW Craig, and M. A novel antimatter detector based on X-ray deexcitation of exotic atoms. *The Astrophysical Journal*, February 2002.

[Nakamura *et al.*, 1984] K Nakamura, J Chiba, and T Fujii. Absorption and Forward Scattering of Antiprotons by C, Al, and Cu Nuclei in the Region 470-880 MeV/c. *Physical Review Letters*, 52(9), 1984.

[Peacock, 1999] John Peacock. *Cosmological Physics*. Cambridge University Press, Cambridge, 1999.

[Peccei and Quinn, 1977a] R. D. Peccei and Helen R. Quinn. Constraints imposed by CP conservation in the presence of pseudoparticles. *Phys. Rev. D*, 16:1791–1797, Sep 1977.

[Peccei and Quinn, 1977b] R. D. Peccei and Helen R. Quinn. CP conservation in the presence of pseudoparticles. *Phys. Rev. Lett.*, 38:1440–1443, Jun 1977.

[Pell, 1960] E. M. Pell. Ion Drift in an n-p Junction. *Journal of Applied Physics*, 31(2):291, 1960.

[Polesello and Tovey, 2004] G Polesello and D.R Tovey. Constraining SUSY Dark Matter with the ATLAS Detector at the LHC. *Journal of High Energy Physics*, 2004(05):071–071, May 2004.

[Polster *et al.*, 1995] D Polster, D Hilscher, H Rossner, and T von Egidy. Light particle emission induced by stopped antiprotons in nuclei: Energy dissipation and neutron-to-proton ratio. *Physical Review C*, 51(3), 1995.

[Porter *et al.*, 2011] TA Porter, RP Johnson, and PW Graham. Dark Matter Searches with Astroparticle Data. *Arxiv preprint arXiv:1104.2836*, pages 1–52, 2011.

[Protic and Krings, 2002] D. Protic and T. Krings. Development of Transmission Si(Li) Detectors, 2002.

[Randall and Sundrum, 1999] Lisa Randall and R Sundrum. Large mass hierarchy from a small extra dimension. *Physical Review Letters*, 1999.

[Rubin and Ford, 1970] VC Rubin and WK Ford. Rotation of the andromeda nebula from a spectroscopic survey of emission regions. *The Astrophysical Journal*, 1970.

[Salati *et al.*, 2010] P. Salati, F. Donato, and N. Fornengo. Indirect Dark Matter Detection with Cosmic Antimatter. *Arxiv preprint*, (40):34, March 2010.

[Serlemitsos, 1984] PJ Serlemitsos. Broad Band X-Ray Astronomical Spectroscopy. *Nuclear Science, IEEE ...*, 31(1):786–790, 1984.

[Servant and Tait, 2003] G Servant and TMP Tait. Is the Lightest Kaluza Klein Particle a Viable Dark Matter Candidate ? *Nuclear Physics B*, 2003.

[Sudov, 1993] A. S. Sudov. Production of light particles after antiproton-nucleus annihilation and their interpretation with statistical models. *Nuclear Physics A*, 554(2):223–245, March 1993.

[Weniger, 2012] Christoph Weniger. A tentative gamma-ray line from Dark Matter annihilation at the Fermi Large Area Telescope. *Journal of Cosmology and Astroparticle Physics*, pages 0–23, 2012.

[Wiegand, 1969] Clyde Wiegand. Measurement of K^{-}-Mesonic X-Ray Spectra of Medium and Heavy Elements. *Physical Review Letters*, 22(23):1235–1238, June 1969.